THE DYNAMICS OF PERSISTENT COLD-AIR POOL BREAKUP

by

Neil P. Lareau

A dissertation submitted to the faculty of
The University of Utah
in partial fulfillment of the requirements for the degree of

Doctor of Philosophy

Department of Atmospheric Science

The University of Utah

May 2014

The University of Utah Graduate School

STATEMENT OF DISSERTATION APPROVAL

The following faculty members served as the supervisory committee chair and members for the dissertation of_____Neil P. Lareau ____.
Dates at right indicate the members' approval of the dissertation.

_____John D. Horel_____, Chair   _____1/30/2014___
                                                     Date Approved

_____Courtenay Strong _____, Member   _____1/30/2014___
                                                     Date Approved

_____Eric Pardyjak_____, Member   _____1/30/2014___
                                                     Date Approved

_____C. David Whitema_____, Member   _____1/30/2014___
                                                     Date Approved

_____Ronald Smith_____, Member   _____1/30/2014___
                                                     Date Approved

The dissertation has also been approved by_____Kevin Perry_____

Chair of the Department/School/College of____Atmospheric Science_____

and by David B. Kieda, Dean of The Graduate School

ABSTRACT

The wind-induced disruption and breakup of multiday cold-air pools are investigated using observational analyses and idealized numerical simulations. The observations are from the Persistent Cold-Air Pool (CAP) Study, which provides modern measurement of the meteorological processes affecting the duration of cold-air pools in the Salt Lake Valley of Utah. In general, the observations indicate that synoptic-scale processes control cold-air pool duration while local processes affect near-surface stratification and mixing. The most common form of CAP breakup is due to cold-air advection aloft. However, analyses reveal that some cold-air pools are destroyed or disrupted by strong winds penetrating into the valley. The resulting wind-CAP interactions are complex, involving sequential CAP displacements, internal oscillations, dynamic instabilities, and terrain-flow interactions. Large Eddy Simulations of multiday cold-air pools in idealized valley topography further demonstrate that cold-air pool removal is affected by the interplay of Kelvin-Helmholtz instability and warm air advection. This dynamic instability generates breaking waves in the stratified shear flow that mix cold-air into the warmer flow aloft. Variations in the initial cold pool stratification and valley terrain affect the timescale for cold-air pool removal. Despite these variations, a basic relationship between the magnitude of the flow aloft and the strength of the underlying cold-air pool can be expressed in terms of the "CAP Froude

number." This dimensionless quantity is useful for diagnosing the onset and amplification of turbulent mixing, as well as the complete removal of cold-air pools.

TABLE OF CONTENTS

ACKNOWLEDGEMENTS

I would like to thank my advisor, Dr. John D. Horel, for his guidance and support throughout my graduate career. I would especially like to acknowledge his willingness to work with students with unconventional backgrounds, such as mine. Dr. Horel has provided me with both academic freedom to develop independent ideas as well as expert guidance in all matters scientific.

I would also like to acknowledge the collaborative relationship amongst the members of the Persistent Cold-Air Pool Study research team: Dr. Erik Crosman, Dr. Sebastian Hoch, Dr. C. David Whiteman, Joe Young, and many others have contributed in ways small and large to my research. The contributions of the academic faculty at the University of Utah are also a key aspect of my success in graduate school. I would especially like to thank Dr. Jim Steenburgh, Dr. Thomas Reichler, and Dr. Courtenay Strong for their inspirational and insightful lectures, which continue to serve as a touchstone for my enthusiasm for meteorology.

Finally, I am deeply appreciative of the love and support that I receive from friends and family, especially my wife, Krysia Skorko.

CHAPTER 1

INTRODUCTION

The well-known adage, "The solution to pollution is dilution," highlights the coherent link between poor air quality and persistent Cold-Air Pools (CAPs), namely the lack of *dilution.* CAPs are stably stratified air masses that form in mountain valleys and basins by near surface cooling, warming aloft, or both. Their stratification limits vertical mixing (e.g., dilution) and the flanking topography prevents horizontal advection (e.g., stagnation). As a result, the longer a CAP persists the greater the buildup of anthropogenic and biogenic emissions.

This linkage between poor air-quality and CAP duration is particularly apparent in Utah's Salt Lake Valley (SLV), which is densely populated, confined by significant mountain ranges, and experiences recurrent multiday CAPs during winter (Wolyn and Mckee 1989; Reeves and Stensrud 2009; Lareau et al. 2013). Emissions from home heating, vehicles, and industry rapidly accumulate within these decoupled air masses (Fig. 1.1). As a consequence, the concentration of fine particulate aerosol ($PM_{2.5}$) frequently exceeds the National Ambient Air Quality Standard (NAAQS; Silcox et al. 2012; Lareau et al. 2013). These elevated levels of $PM_{2.5}$ are linked with increased risk for cardiovascular disease and decreased lifespan (Pope et al. 2006; Pope et al. 2009). High levels of carbon dioxide, carbon monoxide, and ozone may also occur (Pataki et al.

2005; Pataki et al. 2006).

The air quality in the SLV and other urbanized mountain basins typically returns to healthier levels only once a CAP has been removed. Unfortunately, the multiscale processes contributing to CAP removal are incompletely understood and poorly resolved in forecast models (Holstag et al. 2013). As a result, accurate forecasting of CAP duration remains challenging, sometimes leading to large forecast errors for both temperature and air quality (Zardi and Whiteman 2013).

To improve our understanding of the atmospheric controls on CAP duration, the Persistent Cold-Air Pool Study (PCAPS; Lareau et al. 2013) was conducted during the winter of 2010-2011. The primary objective of the two-month field project was to observe the multiscale meteorological processes affecting the life cycle of CAPs. This goal was addressed by collecting intensive observations during 10 long-lived CAP events using surface, remote sensing, and upper-air instrumentation distributed throughout the SLV. A detailed summary of PCAPS is provided in Lareau et al. (2013).

The PCAPS observations reveal that synoptic-scale variations determine CAP strength and duration while local-scale processes alter near-surface stratification and mixing. These results are consistent with previous investigations of CAP lifecycles (Wolyn and Mckee 1989; Whiteman et al. 1999; Whiteman et al. 2001; Zhong et al. 2001; Reeves and Stensrud 2009), but provide greater spatial and temporal resolution than earlier studies, especially for local processes.

The CAP during 1-9 January 2011 (referred to as Intensive Observing Period 5, IOP-5) provides a clear example of these scale dependencies and interactions (Fig. 1.2). The formation of the CAP on 1-2 January occurs as high pressure develops, which is

accompanied by warming aloft due to synoptic-scale advection and subsidence. As the warm air descends into the valley (downward sloping isentropes) a capping inversion is formed (horizontal isentropes), thereby decoupling the valley atmosphere from the flow aloft. Aerosols then rapidly accumulate within the newly stagnated air mass, apparent in Fig. 1.2 in terms of high backscatter intensity observed by a laser ceilometer (Young 2013).

Within the IOP-5 CAP, diurnal variations in surface heating affect the boundary layer stratification and depth of vertical mixing. Near surface "domes" confine low potential temperature and represent surface-based radiative inversions on clear nights (days 1, 2, 5 and 6 in Fig. 1.2), whereas convection during late afternoon distributes aerosols over greater depth. This daytime convection is, however, insufficient to remove the overlying capping inversion, and thus the CAP persists for many days. Clouds aloft (3-4 January) or within the CAP (7-8 January) reduce the nocturnal stratification near the surface and the mixing depth is increased.

Variations in synoptic-scale advection aloft during IOP-5 modulate the strength of the capping layer. For example, the CAP is weakened on 4 January due to cooling associated with a diminutive short-wave trough, but then substantively strengthened by strong warm air advection and subsidence accompanying renewed long wave ridging on 5-8 January. During that time the CAP reaches a maximum strength of ~20 K.

The destruction of the IOP-5 CAP occurs by vigorous cold-air advection aloft accompanying a sharply delineated arctic cold front on 9 January. The arrival of cold-air above the CAP reduces the stratification, thus permitting deep mixing and ventilation of pollution (reduction in backscatter intensity). Synoptic-scale cold-air advection of this

sort is implicated as the dominant factor in the destruction of many long-lived CAPs (Whiteman et al. 1999; Whiteman et al. 2001; Reeves and Stensrud 2009).

In the absence of strong cold-air advection, CAPs can also be destroyed or disrupted by strong winds penetrating into a valley (Petkvosek 1992; Gubser and Richner 2001; Whiteman et al. 2001; Rakovec et al. 2002; Flamant et al. 2002). Flow-CAP interactions of this sort are frequently observed in the SLV when warm southerly winds develop ahead of approaching troughs. Despite the semiregular occurrence of these events, the outcomes of the wind-CAP interactions are particularly difficult to predict: sometimes the strong flows merely perturb a CAP, whereas the CAP is flushed from the valley during other cases.

Substantive wind-induced CAP disruptions were observed during three IOPs of PCAPS (Fig. 1.3). The events are surprisingly similar through much of their evolution. In each case, southerly flow above a preexisting CAP accelerates to ~15 m/s in approximately 24 hs due to an approaching trough. As the flow aloft increases, the CAP thins downward from the top. During IOPs 1 and 4, the thinning advances to the valley floor, producing bursts of warm gusty conditions and providing localized ventilation of pollution. During IOP-1, this disruption is due to temporary displacement of the cold-air (near 06 UTC), causing a period of ventilation over the southern two-thirds of the valley (Lareau et al. 2013). However, after the winds aloft abate, the CAP advects back into the valley and persists for another 4 days. In contrast, the erosion and destabilization of the CAP is irreversible during IOP-4, leading to complete removal of the valley stratification, although cold-air advection aloft also contributes to this breakup.

During IOP-9, the near surface conditions remain entirely decoupled from the

accelerating flow aloft (Fig. 1.3c). A sharp elevated inversion layer separates the strong south wind from the stagnant flow within the CAP and only a modest reduction of the depth of cold air accompanies the strongest winds. The CAP is subsequently destroyed the following day, but its breakup is then dominated by cold-air advection, as in IOP-5.

The similarities and differences amongst these observations of wind-CAP interaction pose a number of scientific questions: What causes the top-down thinning of the CAP? Is it possible to differentiate CAPs that will and will not be removed by moderately strong winds? If so, is there a threshold wind speed for removal? How does the depth and strength of the stratification affect the timescale for removal?

This study addresses these questions using a combination of observational analyses and high-resolution numerical simulations to identify and examine the key dynamical processes leading to CAP removal and displacement. Observational analyses are presented in Chapter 2 for PCAPS IOP-1 (Fig. 1.3a), which provides a particularly rich set of surface and upper air observations. The results reveal complex interactions of the flow aloft with the stratified valley air mass, including: CAP displacement due to mountain waves, turbulent mixing via dynamic instabilities, tilting of the CAP, and basin scale internal oscillations.

To broaden the scope of this study beyond these observational results, a series of idealized numerical experiments are presented in Chapter 3, motivated by the PCAPS cases. The simulations explore the interaction of accelerating flow with preexisting cold-air pools of varying strength and depth confined in idealized valley topographies. Those results show that the top-down thinning of the CAPs, as seen in Fig. 1.3, results from the interplay of shear-induced turbulence and warm air advection. The onset and

amplification of turbulent CAP erosion can be summarized in terms of a dimensionless parameter, the CAP Froude number, which incorporates the strength of the CAP relative to that of the flow aloft.

Finally, the lessons learned from the observations, analyses, and simulations are reflected upon in Chapter 4. The broader implications of these findings are discussed as well as further work that would complement the research presented herein.

1.1 References

Beard, J. D., C. Beck, R. Graham, S. Packham, M. Traphagan, R. Giles, and J. G. Morgan, 2012: Winter temperature inversions and emergency department visits for Asthma in Salt Lake County, Utah, 2003-2008. *Env. Health Pers*., **120,** 1385-1390.

Flamant, C. , P. Drobinski, N. Furger, B. Chimani, S. Tschannett, R. Steinacker, A. Protat, H. Richner, S. Gubser, and C. Haberli, 2006: Föhn/CAP interactions in the Rhine valley during MAP IOP 15. *Quart. J. Roy. Meteorol. Soc.,* **132**, 3035-3058.

Gubser, S., and H. Richner, 2001: Investigations into mechanisms leading to the removal of the cold-pool in foehn situations. Extended abstract, *MAP meeting at Schliersee. MAP Newsletter 15*. Available at:http://www.map.meteoswiss.ch/map-doc/NL15/gubser2.pdf

Holtslag, A. A. M., and Coauthors, 2013: Stable atmospheric boundary layers and diurnal cycles: Challenges for weather and climate models. *Bull. Amer. Meteor. Soc.*, **94**, 1691–1706.

Lareau, N. P., E. Crosman, C. D. Whiteman, J. D. Horel, S. W. Hoch, W. O. J. Brown, and T. W. Horst, 2013: The persistent cold-air pool study. *Bull. Amer. Meteor. Soc.*, **94,** 51–63.

Pataki, D. E., B. J. Tyler, R. E. Peterson, A. P. Nair, W. J. Steenburgh, and E. R. Pardyjak, 2005: Can carbon dioxide be used as a tracer of urban atmospheric transport? *J. Geophys. Res.,* **110,** D15102.

Pataki, D. E., D. R. Bowling, J. R. Ehleringer, J. M. Zobitz, 2006: High resolution atmospheric monitoring of urban carbon dioxide sources. *Geophys. Res. Let.,* **33,** L03813.

Petkovšek, Z., 1992: Turbulent dissipation of cold air lake in a basin. *Meteor. Atmos.*

Phys., **447,** 237-245.

Pope, III C. A., and coauthors, 2006: Ischemic heart disease events triggered by short-term exposure to fine particulate air pollution. *Circulations,* **112,** 2443-2448.

Pope, III C. A., M. Ezzati, and D. W. Dockery, 2009: Fine-particulate air pollution and life expectancy in the United States. *New Engl. J. Med.,* **360,** 376-386.

Reeves, H. D., and D. J. Stensrud, 2009: Synoptic-scale flow and valley cold pool evolution in the western United States. *Wea. Forecasting,* **24,**1625-1643.

Whiteman, C. D., X. Bian, and S Zhong, 1999: Wintertime evolution of the temperature inversion in the Colorado Plateau Basin. *J. Appl. Meteor.,* **38,** 1103-1117.

Whiteman, C. D., S. Zhong, W. J. Shaw, J. M. Hubbe, X. Bian, and J. Mittelstadt, 2001: Cold pools in the Columbia basin. *Wea. Forecasting,* **16,** 432-447.

Wolyn, P. G., and T. B. McKee, 1989: Deep stable layers in the intermountain Western United States. *Mon. Wea. Rev.* **117,** 461-472.

Young, J., 2013: Investigation of wintertime cold-air pools and aerosol layers in the Salt Lake Valley using a laser ceilometer. MS Thesis. University of Utah. 118 pp.

Zardi, D. and C. D. Whiteman, 2013: Diurnal Mountain Wind Systems. *Mountain Weather Research and Forecasting: Recent Progress and Current Challenges,* F. K. Chow, S. F. J. De Wekker, and B. Snyder, Ed., Springer, 35-119.

Fig.1.1. View to the southwest across the Salt Lake Valley during a persistent CAP. The haze is primarily aerosol, as indicated by the bright white forward scattering toward the photographer (Photo courtesy of Dr. Jim Steenburgh).
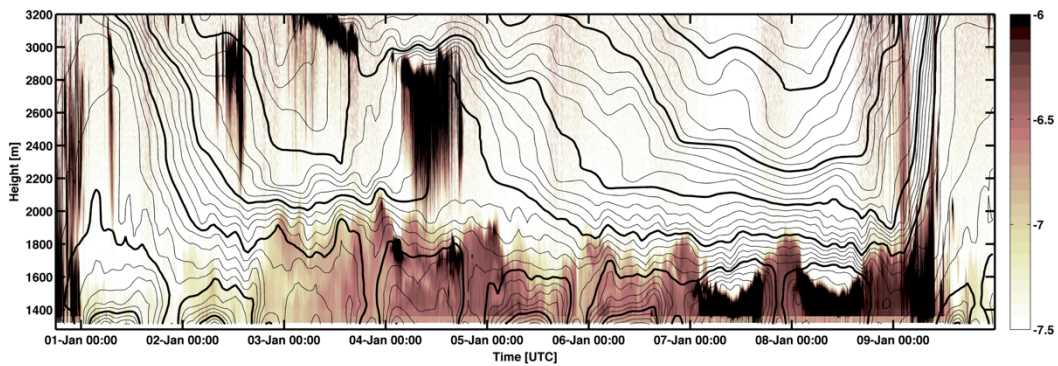
Fig.1.2 Time-height evolution of potential temperature (light contours every 1 K, bold contours ever 5 K) and logarithmic aerosol backscatter intensity (shading) during PCAPS IOP-5. Black shading corresponds to hydrometeors, light shades are due to high aerosol loadings, and white is indicative of clear air. Adapted from Lareau et al. 2013.
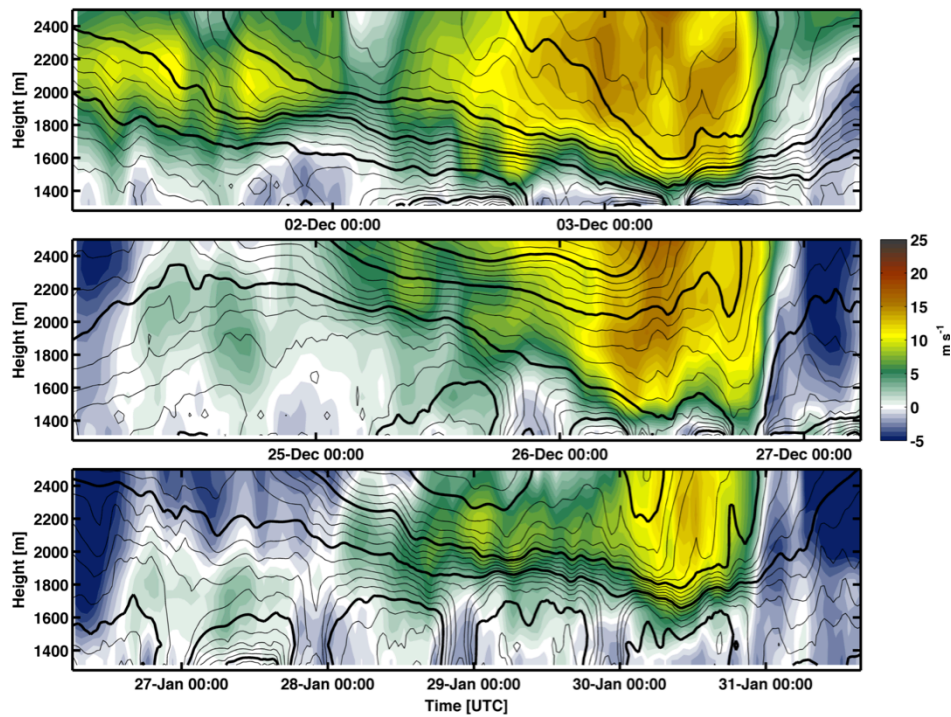
Fig. 1.3 Time height evolution of potential temperature (light contours every 1 K, bold contours ever 5 K) and meridional wind (shading) during selected Persistent Cold-Air Pool Study Intensive Observing Periods (IOPs): (a) IOP-1, (b) IOP-4, and (c) IOP-9.

CHAPTER 2

DYNAMICALLY INDUCED DISPLACEMENTS OF

A PERSISTENT COLD-AIR POOL

2.1 Abstract

This study examines the influence of a passing weather system on a persistent cold-air pool (CAP) during the Persistent Cold-Air Pool Study in the Salt Lake Valley, UT. The CAP experiences a sequence of along-valley displacements that temporarily and partially remove the cold air in response to increasing along-valley winds aloft. The displacements are due to the formation of a mountain wave over the upstream topography as well as adjustments to the regional pressure gradient and wind stress acting on the CAP. These processes appear to help establish a balance wherein the depth of the CAP increases to the north. When that balance is disrupted, the CAP tilt collapses, which sends a gravity current of cold air back upstream and thereby restores CAP conditions throughout the valley. Intravalley mixing of momentum, heat, and pollution within the CAP by Kelvin-Helmholtz waves and seiching is also examined.

2.2 Introduction

The disruption of persistent cold-air pools (CAPs) arising from passing weather systems is examined in this study. CAPs are decoupled air masses that form in mountain

valleys and basins due to cooling of the air near the surface, warming of the air aloft, or both (Whiteman et al. 1999). The resulting stable stratification suppresses vertical mixing while the confining topography prevents advection and favors air stagnation (Zangl 2003). Persistent CAPs are simply CAPs surviving through more than one diurnal cycle (Whiteman et al. 2001).

Persistent CAPs are often accompanied by adverse societal impacts. When they occur in densely settled valleys, the emissions from vehicles, home heating, and industrial sources accumulate, leading to unhealthy air quality (Reddy et al. 1995; Pataki et al. 2005; Pataki et al. 2006; Malek et al. 2006; Silcox et al. 2012). High particulate concentrations during CAPs have recently been linked to increased risk for cardiovascular disease and asthma and may lead to decreased lifespan (Pope et al. 2009; Beard et al. 2012). Suppressed temperatures within CAPs combined with the presence of snow cover can also increase the likelihood of fog, which affects air and ground transportation (Wolyn and Mckee 1989).

The strength and longevity of persistent CAPs is modulated by the synoptic conditions establishing them, the surface energy budget, and subsequent interactions with passing weather systems (Wolyn and Mckee 1989; Whiteman et al. 1999; Whiteman et al. 2001; Reeves and Stensrud 2009; Gillies et al. 2010; Zardi and Whiteman 2013). CAPs most often form during the warming aloft accompanying the arrival of high-pressure weather systems. Weak disturbances may then temporarily perturb a CAP, whereas more vigorous baroclinic troughs are likely to completely destroy them, especially those accompanied by strong cold-air advection (Whiteman et al. 1999; Whiteman et al. 2001; Zhong et al 2001; Reeves and Stensrud 2009; Zardi and Whiteman

2013).

In the absence of strong cold-air advection, forecasting the demise of CAPs remains a challenge. During such situations, CAP removal may be controlled by interactions among four other mechanisms: (1) internal *convection*, (2) top-down *turbulent erosion*, (3) CAP *displacement* and (4) *airflow* over the upstream topography (Lee et al. 1989; Petkovšek 1992; Petkovšek and Vrhovec 1994; Gubser and Richner 2001; Zängl 2003; Zängl 2005; Flamant et al. 2006).

In contrast to diurnal CAPs that form overnight and are destroyed by daytime heating, *convection* alone is generally insufficient to destroy persistent CAPs due to weak sensible heat flux during the winter (Zhong et al. 2001). However, when other processes are weakening a CAP, convection may become an important factor in breakup (Whiteman et al. 1999; Zhong et al. 2001, Zardi and Whiteman 2013). For example, Whiteman et al. (1999) show that the final removal of persistent CAPs preferentially occurs in the afternoon when sensible heat flux is strongest.

The second mechanism, *turbulent erosion*, is the break down of CAP stratification via irreversible turbulent motions. Petkovšek (1992) proposed a semi-analytic model for this process wherein turbulent flow above a CAP progressively erodes downward into the stratified air. In this scenario, the depth of the CAP is progressively reduced, but the strength of the stratification within the capping layer increases in time. The increased capping layer stratification subsequently suppresses the rate of turbulent encroachment, thus requiring an accelerating wind aloft for erosion to continue. Zhong et al. (2003) diagnose the time-scale for turbulent CAP erosion using idealized CAP profiles and steady winds at different strengths. Their results show that the erosion rate decays in

time, consistent with Petkovšek's hypothesis, and that turbulent erosion is very slow for typical CAP scales and thus unlikely to cause CAP breakup independent of other processes.

Turbulent erosion of stratification has also been observed in other geophysical flows, such as mixing across the thermocline in lakes and oceans (Fernando 1991). Strang and Fernando (2001 a, b) use laboratory tank experiments to examine the deepening rate of a mixed layer into a stable layer and show that mixed layer deepening progresses via Kelvin-Helmholtz and other dynamic instabilities, the occurrence of which is controlled by the Richardson number.

CAP *displacement*, the third process, is the rearrangement of CAP mass via static and dynamic processes. Petkovšek and Vrhovec (1994), and later Zängl (2003), show that CAPs hydrostatically adjust to regional pressure gradients by developing a sloping interface and thus an internal pressure gradient that offsets the pressure gradient aloft. When the CAP slope becomes sufficiently large, cold-air spills over the confining topography and the volume of air within the CAP is reduced (Zängl 2003). CAP tilt may also have a component due to wind stress acting on the CAP (Petkovšek and Vrhovec 1994, Gubser and Richner 2001, Zängl 2003). This effect can be particularly pronounced when winds are ageostrophic, e.g., acting in the same sense as the pressure gradient force (Zängl 2003). This wind-stress effect is similar to "wind set-up" or storm surge that displaces water along the downwind fetch within lakes.

CAP displacement may also occur due to *airflow* over the upstream topography. Lee et al. (1989) examine the interaction of a mountain wave with a lee-side CAP in idealized simulations, and show that the CAP is displaced by the mountain wave unless there is an

adverse pressure gradient generating an opposing surface flow toward the mountain. Interestingly, they also found that turbulent erosion was a minimal factor in CAP evolution despite strong shear.

More generally, the ventilation of valleys containing stratified air masses has been related to the Froude number (or its inverse, the nondimensional valley depth):

$$Fr = \frac{\overline{U}}{NH} \qquad (2.1)$$

where $\overline{U}$ is the mean wind above the valley, N is the Brunt–Väisälä frequency, and H is the valley depth (Bell and Thompson, 1980; Tampieri and Hunt, 1985; Lee et al. 1987). Bell and Thompson (1980) found that when $Fr \geq 1.2$, the flow tends to sweep through a valley despite the stratification. Other studies have shown that, in addition to Fr, the terrain geometry (including ridge spacing, slope angle, and the wavelength of lee waves) affects the character of the flow into the valley (Tampieri and Hunt, 1985; Lee et al. 1987).

Relatively few observational studies have focused on the breakup of CAPs. Whiteman et al. (2001) document the differing destructive processes during two CAPs in the Columbia River Basin, one being affected by strong down slope winds and the other by cold-air advection and internal convection. Rakovec et al. (2002) examined turbulent processes during the breakup of CAPs in a Slovenian mountain valley. Using field observations and numerical experiments, they show that turbulent erosion commences above a threshold wind speed and continues if the flow accelerates. Flamant et al. (2006) examined the interaction of foehn winds with a CAP in the Rhine Valley during the Mesoscale Alpine Project. They conclude that CAP displacement along the valley axis is primarily caused by advection within the foehn flow, but also show that Kelvin-

Helmholtz and gravity waves affect the CAP to a lesser degree.

In this study, we use data collected in the Salt Lake Valley of northern Utah during the Persistent Cold-Air Pool Study (PCAPS, Lareau et al. 2013) to examine the passage of a short wave trough during a multiday CAP. This trough-CAP interaction produced a variety of waves, displacement and fronts that disrupted the otherwise quiescent CAP. In the following sections we analyze the observed changes in CAP structure and develop a simple conceptual model for the trough-CAP interaction based on the observations and an idealized numerical simulation using a Large-Eddy Simulation version of the Weather Research and Forecasting (WRF-LES) model (Skamarock et al. 2008).

2.3 The Salt Lake Valley and Meteorological Data

2.3.1 The Salt Lake Valley

The Salt Lake Valley (SLV) is located in northern Utah, USA at the eastern edge of the semi-arid Intermountain West, which is the region between the Sierra Nevada and Rocky Mountains. CAPs are common in the SLV during winter, affecting the nearly 1 million residents. The meridionally oriented valley is confined to the east and west by the Wasatch (2800 m) and Oquirrh (2400 m) Mountains, respectively (Fig. 2.1). To the south, the Traverse Mountains (1800 m), which have 500 m of relief, act as a partial barrier separating the SLV from the neighboring Utah Valley. The SLV opens to the northwest into the Great Salt Lake Basin. The lowest elevations in the SLV are found along the Jordan River, which slopes downward from 1400 m as it enters the SLV through the Jordan Narrows, a gap through the Traverse Mountains, to 1280 m at the shore of the Great Salt Lake. East-west asymmetries in the SLV have large impacts

during CAPs: (1) there is more landmass at a given elevation to the west of the Jordan River, and (2) north-south flow is blocked more to the east of the river than to its west.

2.3.2 Meteorological Data

The meteorological data used in this study were collected during the PCAPS Intensive Observing Period 1 (IOP-1). IOP-1 examined a multiday CAP that formed on 1 December and lasted through late on 6 December 2010. We describe here the key observational resources that are used in this study, the locations of which are shown in Fig. 2.1. An overview of PCAPS and all available data resources are provided by Lareau et al. (2013).

To diagnose the evolution of the IOP-1 CAP, we construct time-height profiles of temperature, potential temperature, relative humidity, and wind intended to be representative of the conditions within the central core of the SLV. For this purpose, we rely most heavily on the data collected at the Integrated Sounding System (ISS) sites labeled by blue dots in Fig. 2.1, which are on bluffs immediately to the west of the Jordan River. A 915 MHz radar wind profiler (RWP) and Radio Acoustic Sounding System (RASS) were operated continuously at ISS-N, while radiosondes were launched at 3-12 h intervals from ISS-S, 1 km to the south, depending on the operational plan for the field program. We constrain these vertical profiles near the surface by automated weather observations at ISS-S and also use radiosonde data from the Salt Lake International Airport (KSLC; black dot in Fig. 2.1) above the boundary layer to improve the temporal coverage for periods when sondes were not launched at ISS-S. Gaps in the remote sensor data due to low signal-to-noise ratios are filled objectively using an "inpainting" analysis

technique (Schönlieb 2012) and bounded by surface and radiosonde data at the gap boundaries. The resulting time-height profiles are quality controlled to remove spurious unphysical values and gradients and then averaged linearly with interpolated time-height profiles from the radiosonde data alone. The final set of time-height profiles reflect an effective blend of the remote sensor and in situ observations at a temporal interval of 30 mins and a vertical resolution of 50 m. These profiles are representative of the conditions throughout most of the SLV during this CAP except during the Disturbance Phase, described later, when these profiles reflect conditions near the ISS sites only.

A laser ceilometer located at ISS-S is used to characterize the mixing depth of aerosol, the presence of hydrometeors, and fine-scale structures within the boundary layer at 16 s temporal resolution (Young 2013). Two pseudo-vertical transects along the confining topography are created based on lines of near-surface sensors running up the sidewalls. The first transect is composed of six automatic weather stations ascending the Traverse Mountains in the southeast corner of the valley with SM6 located on the valley floor at an elevation of 1370 m while SM1 is on the Traverse Mountain ridgeline at an elevation of 1930 m (see Fig. 2.1). These stations were equipped with wind, temperature, humidity and pressure sensors and recorded data every 5 mins. The second transect uses HOBO™ temperature data loggers aligned along Harker's Ridge, which is a subridge along the east slope of the Oquirrh Mountains (northern string of green dots in Fig. 2.1). The HOBOs also report temperature every 5 mins and are spaced vertically at 50 m intervals from 1350 to 2500 m.

Data from over fifty surface weather stations within the SLV with diverse suites of sensors are used from the Mesowest archive (Horel et al. 2002). In addition, seven 10-m

Integrated Surface Flux System (ISFS) stations providing radiation, kinematic flux, and ground probe sensors as well as standard weather variables were deployed around the Salt Lake Valley as part of PCAPS (numbered in purple dots in Fig. 2.1).

2.4 Results

2.4.1 IOP-1 Overview

Wei et al. (2013) describe the conditions from 30 November – to 7 December 2010 that encompass IOP-1 without relying on the PCAPS field campaign data, i.e., they examined KSLC radiosonde and Mesowest surface observations in combination with a WRF model simulation. Based on all the PCAPS data now available, we show that the IOP-1 CAP progressed through 4 stages in its life cycle: formation, disturbance, persistence, and break-up (Fig. 2.2). This paper primarily examines the disturbance phase, but here we briefly summarize the event in its entirety.

2.4.1.1 Formation

The IOP-1 CAP followed the passage of a strong shortwave trough, which brought snow and cold temperatures to the SLV. The CAP was then initiated by mid-tropospheric ridging and warming, which formed a capping layer of strong static stability that decoupled the cold valley atmosphere from the flow above crest level (Wei et al. 2013).

The strength of the nascent CAP was subsequently augmented by a surface based radiation inversion forming during clear skies overnight on 2 December. Averaged over the seven ISFS stations, the net radiative cooling in the valley on that night is the strongest during the CAP episode (not shown). Combined, the warming aloft and cooling

at the surface yielded a 700 m deep CAP with a surface potential temperature deficit (relative to that near the top of the CAP) in excess of 15 K at 1200 UTC 2 December. Weak winter insolation, high albedo due to snow cover, and the strong stability suppressed the growth of the convective boundary layer the following afternoon, which allowed the CAP to persist and for aerosol to accumulate rapidly (Fig. 2.2a). Concentrations of aerosol particulates with diameters less than 2.5 μm ($PM_{2.5}$) surpassed the National Ambient Air Quality Standard (U.S. EPA 2013) of 35 μg m^{-3} after just the second day of the cold pool (not shown).

2.4.1.2 Disturbance

The disturbance phase of IOP-1 occurred on 3 December as the initial ridge broke down and a weak shortwave trough accompanied with midlevel clouds moved across the Intermountain West (not shown). The approaching trough generated a compact regional pressure gradient that accelerated southerly winds above the CAP, reaching a peak meridional speed approaching 15 m s^{-1} during the early morning of 3 December (Fig. 2.2b). Terrain channeling controlled the orientation of the flow in the SLV, leading to ageostrophic south winds blowing along the valley axis and down the regional pressure gradient.

As the winds increased aloft, the CAP thinned from approximately 700 m at 0000 UTC 2 December to 150 m at 0600 UTC 3 December (Fig. 2.2 a, b). The downward slope of the isentropes within the capping layer of strong static stability is partially due to increased warm air advection associated with the strengthening southerly flow and, as we show later, also due to tilting and displacement of the CAP.

Surface conditions at station SM6 on the valley floor at the extreme southern end of the SLV and immediately in the lee of the Traverse Mountains (Fig. 2.2c), remained quiescent (speeds less than 3 m s^{-1}) and were similar to those observed throughout most of the SLV until 0000 UTC 3 December at which time the first burst of warm (>10 $^{\circ}$C) and windy (speeds greater than 7.5 m s^{-1}) conditions penetrated for a brief time to the surface. CAP conditions resumed at this location until 0300 UTC followed by a second intrusion of warm, dry, windy conditions through 0830 UTC (Fig. 2.2c). Another short period of CAP conditions was followed by the third warm, windy burst from 1000-1300 UTC. The causes for these abrupt changes in surface conditions are explored throughout this paper.

The disturbance period in the valley concludes after 1500 UTC 3 December as the trough axis passes over the region bringing a sharp reduction in the winds aloft and surface conditions at the south end of the valley return roughly to those observed the day before. Hence, the disturbance period is more complicated than the hypothesis provided by Wei et al. (2013) that it was due to the passage of a weak cold front.

2.4.1.3 Persistence

Following the trough's departure, the CAP returns to a quiescent state, providing continued cold temperatures and high levels of pollution as ridging builds over the Intermountain West on 4-6 December (Fig. 2.2a). During this phase, the CAP eventually developed a stratocumulus-capped boundary layer and periods of surface fog (red shading Fig. 2.2a) leading to travel delays and, unfortunately, contributing to the crash of a small aircraft to the north of the SLV near Ogden, UT on 6 December.

2.4.1.4 Breakup

The long-lived IOP-1 CAP was finally destroyed late on 6 December by cold-air advection aloft, internal convection, and enhanced winds associated with a much stronger shortwave trough moving into the region (Wei et al. 2013). The breakup of the valley stratification was accompanied by a reduction in the particulate pollution and a return to healthier air quality (not shown).

2.4.1.5 Forecast Uncertainty

During this CAP event, forecasting the extent of the trough-CAP interaction on 3 December was particularly difficult. Operational and research numerical weather prediction guidance did not resolve the details associated with this weak trough passage and the limited impact it had on improving air quality in the valley. For example, while the retrospective research simulations completed by Wei et al. (2013) captured many of the general features associated with IOP-1, their simulation fared poorly during the Disturbance Phase with wind speed and direction errors as large as 10 m s^{-1} and 90°, respectively, and temperature errors greater than 2.5° C below 700 hPa. To better understand the unresolved processes that contributed to the CAP evolution during the Disturbance Phase, we now turn to detailed analyses of PCAPS observations.

2.4.2 Surface Temporal Evolution

The abrupt changes in surface meteorological conditions evident in Fig. 2.2c are caused by a sequence of displacements of the CAP along the valley axis. To better understand these displacements, hourly surface temperature analyses at 100 m horizontal

resolution are created from all available surface temperature observations using a Barnes horizontal and vertical distance weighting (Barnes 1964) of the departures of the observed temperatures from the temperature estimated for that elevation from the hourly profiles of temperature described in Section 2.2 (Figs. 3-6). The horizontal e-folding radius is 20, 10, and 5 km for three successive iterations of the analysis cycle. The vertical radius is held constant at 75 m. Variations in the e-folding radii alter the fine scale structure (e.g., fronts) in the analyses but do not substantively alter the interpretation of the results. The relatively dense network of temperature observations available in the SLV during this IOP reduces the sensitivity of the resulting analyses to the technique, e.g., very similar temperature analyses have been obtained for this period using a two-dimensional variational analysis technique (Tyndall and Horel 2012).

The overall dependence of temperature on elevation is immediately apparent from the surface temperature observations and analyses in Figs. 3-6. For example, the string of HOBO temperature sensors along Harker's Ridge (Fig. 2.1) at 0000 UTC (Fig. 2.3a) transitions from low temperatures (blue shades) in the valley to much higher temperatures on the western slopes of the valley (yellow and orange shades) before again dropping at the upper reaches of the Oquirrh Mountains (blue shades). Prior to 0000 UTC, the temperatures in the lowest elevations of the SLC were nearly uniform (not shown).

The first CAP displacement in the valley is evident at 0000 UTC when the leading edge of the CAP shifts northward, forming a roughly east-west frontal zone (Fig. 2.3a). Warm air (5-10° C) and southerly winds penetrate to the surface to the south of the front, while cold air (0° C) and northerly winds are present to the north. This initial CAP displacement is reversed over the next 2 hs (Fig. 2.3 b, c) as the CAP edge advances

southward at the lowest elevations, eventually abutting the Traverse Mountains to the east of the Jordan Narrows. The southwest corner of the valley remains out of the CAP at that time with southerly flow continuing over the Traverse Mountains in that region.

A second northward CAP displacement is initiated at 0300 UTC as strong winds and warm temperatures again surface along the southeastern portions of the valley (Fig. 2.3d). The southerly flow is particularly strong and warm along the lee slopes of the Traverse Mountains. The edge of the CAP then moves progressively northward through the valley, reaching its northernmost excursion at 0600 UTC (Fig. 2.4 a,b,c). High temperatures (10° C) and strong southerly winds (7-10 m s^{-1}) are reported at that time throughout the southern two-thirds of the valley, while light winds and temperatures around 0° C persist within the displaced CAP. Adjacent temperature observations indicate that the temperature gradient across the leading edge of the CAP is as much as 7-10° C over 2 km in some places. The pronounced tendency for the displacement of the CAP to be enhanced over the western portion of the SLV arises in part from its higher elevation as well as the unimpeded flow towards the Great Salt Lake on that side of the Valley.

Despite continued strong southerly flow aloft, the leading edge of the CAP again reverses course between 0700 and 0800 UTC, returning southward through the valley (Fig. 2.4d, Fig. 2.5a). As the cold air advances, winds to the north of the front become coherent in strength and direction, flowing from the NW to SE then turning south along the valley axis (Fig. 2.5a). Meanwhile, strong south winds continue to the south of the front indicating convergence along the leading edge of the cold air. As the CAP subsumes observing sites throughout the valley, the cold frontal temperature drop is nearly identical in magnitude to the previous warm frontal rise, which produces the step

changes apparent in individual time series (e.g., Fig. 2.2c). By 0900 UTC (Fig. 2.5b), the cold front encroaches on the Traverse Mountains in the southeastern sections of the SLV. As before, high temperatures and strong winds continue along the southwestern portion of the valley and near the crest of the Traverse Mountains.

The third and final CAP displacement commences between 1000 and 1200 UTC as the frontal boundary again moves northward re-establishing a position across the valley center (Fig. 2.5 c,d and Fig. 2.6a). This third displacement is shorter lived, and as the winds aloft diminish after 1200 UTC (Fig. 2.2b), the cold front mobilizes southward for the final time (Fig. 2.6b). By 1500 UTC (Fig. 2.6d), the CAP has returned throughout the valley and penetrates south through the Jordan Narrows into the neighboring Utah Valley. This reversal in the gap flow effectively marks the end of the disturbed CAP conditions and a return to the quiescent and horizontally homogenous CAP ensues.

2.4.3 Mountain Wave

The north-south displacements of the CAP evident in the hourly surface temperature analyses and other earlier figures result in part from the southerly flow crossing over the Traverse Mountains into the SLV. The vertical profiles of potential temperature and wind speed upstream of the Traverse Mountains at Lehi, UT (red triangle in Fig. 2.1) are shown at 0600 UTC 3 December in Fig. 2.7a, which corresponds to the time of the furthest northward displacement of the CAP. The profiles suggest upstream conditions can be characterized at that time as a two-layer stably-stratified fluid: nearly constant wind speed and potential temperature above 1750 m with 6 K lower potential temperature below 1650 m with increasing wind speeds through the lower layer and extending into

the intervening strong stable layer.

Ignoring the 100 m deep surface based inversion, which reflects local conditions at the observation site, it is possible to compute the internal Froude number from this profile as

$$Fr = \frac{\overline{U}}{\sqrt{g'h}} \qquad (2.2)$$

where $\overline{U}$ is the mean wind speed (6 m s^{-1}), h is the height of the interface (#00 m),

$$g' = \frac{\Delta\theta}{\overline{\theta}} g \qquad (2.3)$$

is the reduced gravity where $\Delta\theta$ is the change in temperature across the capping layer (6 K) and θ is the mean profile temperature (297 K). With these approximations $Fr \approx 0.8$, indicating that the upstream mean flow is slightly slower than the fastest linear shallow water gravity waves. It is likely that as the flow passes over the crest of the Traverse Mountains and thins (e.g., h reduced to 100 m) that it transitions to a super-critical state ($Fr > 1$). Following the hydraulic flow analogy, such a flow is expected to produce a mountain wave with strong downslope winds with nonlinear effects including a downstream hydraulic jump (Durran 1986). Similar flows have previously been documented over the Traverse Mountains during diurnal CAPs by Chen et al (2004).

The impact of the mountain wave along the fall line of the Traverse Mountains is shown in Fig. 2.7c. Consider first the conditions at the time of the upstream sounding (0600 UTC). All stations from the ridge crest (SM1) to the valley floor in the lee (SM6) report the same potential temperature, 297 K, which is consistent with air in the upstream stable layer at 1700 m being lifted up and over the ridge. Wind speeds at the crest (SM1- black curve) and near the valley floor (SM5- red; SM6- dark blue, respectively) are

equally strong at this time and occasionally the winds at the base of the slope are stronger, reflecting acceleration of the flow. (Consistently weaker winds at intervening sites, such as SM4, light blue curve, reflect siting more than atmospheric conditions.)

The pulsing of mountain-waves throughout the Disturbance Phase causes the along-slope potential temperature profile to abruptly switch between stratified and adiabatic states (Fig. 2.7c). For example, the ridge-to-valley potential temperature difference is about 12 K at 0250 UTC, whereas just 20 mins later it is nearly zero (the wind and temperature traces at SM6 in Fig. 2.2c are repeated as the blue curves in Fig. 2.7 c, d). Periods of along-slope adiabatic flow are accompanied by the penetration of strong southerly winds to the valley floor, whereas weak northerly flow near the valley floor coincides with stratification. The restratification of the CAP once the southerly flow lessens is clearly evident after 1300 UTC with no change in the conditions at the top (SM1) and progressively lower potential temperatures down the lee slope into the valley.

To visualize in greater detail the impact of the flow across the Traverse Mountains, an idealized Large-Eddy-Simulation is shown in Fig. 2.8. The simulation is initialized from temperature and wind profiles similar to those shown in Fig. 2.7a and uses a 50 km cross section of the SLV beginning south of the Traverse Mountains, extending north across the ISS sites, and terminating at the Salt Lake International Airport (dashed black line, Fig. 2.1). The model domain is 1 km wide to allow three-dimensional turbulence and uses open boundary conditions at the downwind (northern) boundary and a Rayleigh damping layer at the southern boundary that maintains a constant inflow profile. The ridge topography varies slightly in the span wise direction to help generate 3-D flow. The near-surface inversion in the upstream sounding is extrapolated to match the observed

surface temperature at ISS-S within the SLV, which was 285 K. Radiation is neglected, as are sensible heat fluxes at the surface, and friction is parameterized using a Monin-Obukov surface layer scheme. The horizontal grid spacing is 50 m and there are 100 vertical levels stretched over 10 km. The vertical resolution is nominally 30-50 within the valley. The simulation is run for 1-hr to capture the immediate response of the downstream CAP to the upstream-stratified flow over the topography.

After 1 h, a pronounced mountain wave, hydraulic jump, and CAP displacement are apparent (Fig. 2.8b). The low-level upstream flow is partially blocked such that the depth of the cold lower layer increases until it surmounts the ridge and spills down the lee-slopes. As we speculated above, the Froude number at the mountain crest exceeds the critical value within the overtopping flow. The flow aloft behaves similarly, represented by perturbations in the height of the 300 K isentrope. Accompanying the thermal perturbation of the wave is a marked increase in wind speed above the ridge crest and extending down the lee slope. The lee-side along-slope flow is ostensibly adiabatic with constant speed in excess of 10 m s^{-1}, consistent with observations in Fig. 2.7c,d.

The flow separates from the surface near the base of the lee slope in a pronounced hydraulic jump. The presence of the upstream inversion layer is well known to favor such hydraulic jumps, lee waves, and boundary layer separation (Vosper 2004; Jiang et al. 2007). The surface flow within the jump region is reversed and the air becomes turbulently mixed, reducing the stratification and eroding the surface based inversion. Consequently a front forms separating the comparatively quiescent near-surface CAP conditions to the north from the better-mixed and windier conditions to the south.

The front shown in the numerical simulations suggests a link between the strength of

the mountain wave and the timing of the CAP advance and retreat throughout the valley. For example, the northward displacement of the CAP between 0300 and 0600 UTC correspond to a time of increased downslope flow, whereas the frontal reversal is linked with a modest decrease in the strength of the downslope winds. However, since the mountain wave remains fixed to the topography, additional factors must contribute to the larger displacement of the CAP throughout the valley.

2.4.4 Advance and Retreat of the CAP

While the mountain waves caused the CAP to retreat and advance in the extreme southeastern end of the SLV three times on 3 December, a single disruption of the CAP was centered near 0600 UTC 3 December at the ISS sites. Figure 9 shows in more detail this 3 h period when the CAP retreated northward past the ISS sites temporarily providing clean air (low aerosol backscatter). The retreat of the CAP is synonymous with the passage of a warm front, which is marked by a gradual reduction in the height of the aerosol layer followed by rapid reduction in aerosol concentration (Fig. 2.9a), a 7 K temperature rise (Fig. 2.9b), and a burst of strong southerly winds at the surface (Fig. 2.9c). As the front continues northward past ISS-S, there is a 12 min lag before its passage at ISS-N, which is 1 km away, giving a propagation speed in the along valley direction of 1.5 m s^{-1}. Using these values, the width of the frontal zone is about1 km and the front-normal temperature gradient is then 7 K km^{-1}. The winds on the warm side of the front are around 8 m s^{-1} from the south while those within the CAP are nearly zero.

In contrast to the gradual thinning and quiescent prefrontal conditions associated with the warm front, the cold front arrives with strong northerly winds (4-5 m s^{-1}) and an

abrupt 200 m increase in the depth of the aerosol layer (Fig. 2.9a). This frontal "head" is shown in more detail in Fig. 2.10 and moves much more quickly than the warm front, advancing between the ISS sites in just 5 mins, giving a propagation speed of 3.5 m s^{-1}, which is more than twice that of the warm front. The northerly flow within the cold air behind the front combined with the opposing southerly flow of 5-7 m s^{-1} implies strong convergence.

In the wake of the frontal head, the aerosol layer depth decreases and high amplitude waves develop (Fig. 2.10). This morphology is consistent with the characteristics of an advancing gravity current, e.g., an elevated head, convergent opposing flow, and mixing via Kelvin-Helmholtz waves behind the front (Simpson 1997). Moreover, the ceilometer data suggest that the upstream stratified air mass with high aerosol backscatter is lifted over the gravity current head, with evidence of the frontal disturbance reaching as high as 300 m AGL (Fig. 2.10). This evolution closely resembles laboratory and numerical simulations of gravity currents propagating into a two layer stratified environment (Simpson 1997; White and Helfrich 2012). In this case the advance of the gravity current is an important mechanism for restoring the cold-air pool conditions throughout the valley by allowing the cold-air to propagate against the ambient southerly flow aloft.

2.4.5 CAP Tilt

The displacements of the CAP described in the previous sections are accompanied by variations in the along valley slope of the CAP. As the CAP retreats to the north it exhibits a significant northward incline (e.g., deeper cold air to the north), whereas the southward cold frontal advances correspond to a more horizontally homogenous state. An

example of the tilted CAP is provided in Fig. 2.11, which contrasts the vertical profiles of potential temperature and wind over a distance of 19.2 km between ISS-S and KSLC near the end of the Displacement Phase (1115 UTC). The depth of the CAP at KSLC is clearly 200 m deeper than at ISS-S, and thus about 400 m deeper than at the leading edge of the CAP, which is about 3 km south of ISS-S at this time. The CAP top is identified by the transition to an adiabatic profile aloft (Fig. 2.11a) and the height of the jet maximum in the meridional wind (Fig. 2.11b).

The corresponding pressure gradient between the two soundings is shown in Fig. 2.11c. Above the CAP the pressure gradient is oriented from north to south (e.g., low pressure to the north), consistent with the approaching shortwave trough. The magnitude of the pressure gradient aloft (1.25×10^{-3} Pa m^{-1}) matches the value obtained from reanalysis data at 1200 UTC (not shown). The strong southerly flow (15 m s^{-1}) above the CAP is predominately ageostrophic, reflecting pressure channeling within the SLV as low pressure approaches from the northwest. Within the CAP the pressure gradient is reversed with higher pressure over the northern portion of the valley due to the deeper cold air there. Weak northerly flow down the pressure gradient is evident only near the surface while the winds in the upper layers of the CAP remain from the south, blowing against the reversed pressure gradient.

The force balance maintaining the observed CAP tilt is examined by representing the CAP as a two-layered shallow-water system beneath a rigid upper lid. The lower layer, the CAP, has a density (ρ_2) greater than that of the layer aloft (ρ_1) and the lid applies a pressure gradient ($\frac{\partial P}{\partial x}$) to the system as a whole, representative of the synoptic-scale pressure gradient aloft. If we assume the lower layer is at rest while the upper layer

moves downstream at a speed U_1, then the steady-state nonrotating momentum equation for the lower layer can be written as

$$\frac{\partial H}{\partial x} = -\frac{1}{\rho_1 g'}\frac{\partial P}{\partial x} + \frac{C_d U_1^2}{g'\overline{H}} \tag{2.4}$$

where H is the height of the interface (e.g., the CAP top), $g' = \frac{(\rho_2 - \rho_1)}{\rho_1}g$ is the reduced gravity, $C_d U_1^2$ is the parameterized shear stress between layers using a drag coefficient C_d, and $\overline{H}$ is the mean CAP depth. The bottom stress is neglected since we assume the lower layer is at rest in this simplified framework.

The CAP slope, $\frac{\partial H}{\partial x}$, in Eq. 4 is balanced by both the pressure gradient aloft (first term on the Right Hand Side (RHS)) and the shear stress acting on the upper edge of the CAP (second term on RHS). When the balance is dominated by the pressure gradient term it is referred to as the static adjustment, or inverse barometer response, reflecting the change in depth of the cold (dense) air required to exactly offset the pressure gradient aloft (Gill 1982; Petkovšek and Vrhovec 1994; Zängl 2003). Similarly, the balance between the shear stress and the CAP slope is referred to as the dynamic response, physically representing the piling up of cold-air at the downwind end of the basin (Gubser and Richner 2001). For lakes and oceans this effect is known as *storm surge* or *wind setup* (Gill 1982).

Zängl (2003) demonstrates that the static adjustment for a linearly stratified CAP may be approximated using Margule's formula and the hydrostatic equation. The CAP slope required to offset the synoptic-scale pressure gradient is then given by

$$H(x) = \sqrt{\frac{2RT^2}{Pg}} \sqrt{\frac{\frac{dP}{dx}}{(\gamma_1 - \gamma_2)} x} \qquad (2.5)$$

where $H(x)$ is the height of the CAP top that is primarily a function of the pressure gradient $\frac{dP}{dx}$ immediately above the CAP distance, the difference in ambient lapse rates ($\gamma_1 - \gamma_2$, e.g., adiabatic lapse rate aloft and an inverted lapse rate within the CAP), and the distance x from the edge of the cold air as well as the temperature T and pressure P immediately above the CAP. Using Eq. 5 and values from Fig. 2.11 ($\frac{dP}{dx}$=-1.25 x 10^{-3} Pa m^{-1}, T=282.5 K, P=816.5 x 10^2 Pa, γ_1 = -0.0098 K m^{-1}, γ_2=0.022 K m^{-1}) the required change in elevation of the CAP top to balance the synoptic-scale pressure gradient aloft is ~225 m over 22 km, which is roughly half the observed elevation change estimated earlier.

Hence, the dynamic forcing must be roughly the same magnitude as the static forcing in order to maintain the observed steeper slope of the CAP. For such a steady-state situation to exist, the up-pressure gradient winds transporting mass downstream within the CAP have to be balanced antitriptically through downward momentum flux into the CAP from the flow aloft. Similar antitriptic balances are reported in other boundary layer flows (Sun et al. 2013). Zängl (2003) also simulated steeper slopes than expected from static forcing alone as a result of terrain-channeled ageostrophic flow above a CAP during the approach of a short wave trough, a scenario similar to our observed case.

The time variation of the CAP tilt is examined using the elevation corrected time series of surface pressure for ISS-S and ISFS-2 (Fig. 2.11d). ISFS-2 is located near

KSLC and at a comparable elevation (1289 m). When the corrected pressure at ISFS-2 is higher than that at ISS-S the CAP tilt must exceed that required for the static balance. These over tilted periods, centered at 0000, 0300, 0600 and 1100 UTC, correspond to the periods of northward CAP displacement shown in Figs. 3-6. In contrast, when the cold air advances southward (0100, 0400, 0900, 1400 UTC) the pressure gradient along the valley becomes nearly zero, implying a diminished CAP slope just sufficient to offset the pressure gradient aloft. Following the trough passage at 1500 UTC the synoptic-scale pressure gradient weakens and the CAP returns to a horizontally homogenous state.

We conclude, then, that the observed CAP geometry during the Disturbance Phase reflects a three-way balance between the CAP tilt, the pressure gradient aloft, and the wind stress. This balance can, however, be easily disrupted by changes in the wind speed or pressure gradient aloft. For example, a sudden decrease in the wind shear would cause the internal pressure gradient to be out of balance, and prompt a southward rush of cold-air until a new balance is established. This may help explain the advance and retreat of the CAP that was described in the above sections, the gradual thinning of the warm frontal passage, as well as the gravity current characteristics of the advancing cold air as it passed over ISS-S.

2.4.6 Kelvin-Helmholtz Instability

Many high frequency (order mins) waves are observed during IOP-1 (cf. Fig. 2.9). We are particularly interested in those waves resulting from Kelvin-Helmholtz instability, which is a dynamic instability occurring in stratified shear flows when the kinetic energy available from shear exceeds the work required to move a parcel against the stratification,

a condition given by the critical gradient Richardson number

$$Ri_c = \frac{N^2}{\left(\left(\frac{\partial u}{\partial z}\right)^2 + \left(\frac{\partial v}{\partial z}\right)^2\right)} \leq 0.25 \tag{2.6}$$

where N is the Brunt–Väisälä frequency, and the terms in the denominator are the components of the vertical shear. When this condition is met, Kelvin-Helmholtz waves (KHW) develop, evolving from small perturbations into breaking waves that mix properties across the stratification (Nappo 2002). KHW are an important mixing mechanism in stratified geophysical flows (Fernando 1991) and have been regularly documented in the stable boundary layer and CAPs, often associated with low-level jets (Newsom and Banta 2003; Pinto et al. 2006; Flamant et al. 2006).

During IOP-1, KHW are first observed during the onset of the accelerating winds aloft. For example, Fig. 2.12a shows a sequence of high frequency (1 cycle per min) waves that culminate in a pronounced billow that locally inverts the aerosol gradient within the wave crest at 1226 UTC. The folding of low aerosol air beneath high aerosol air suggests that these waves mix pollution from near the surface into the layers aloft, and presumably act similarly on the temperature profile.

A contemporaneous sounding at KSLC shows that the KHW are centered within a weakly stable layer between the surface-based inversion and the capping layer aloft. The wind shear across this layer is modest, but the Richardson number is nonetheless near the critical value for KHI ($Ri < 0.25$) due to the reduced static stability in that layer.

At 0400 UTC 3 December, winds aloft increase to 10 m s^{-1} and high amplitude waves, some resembling KHW, become a dominant feature in the aerosol backscatter profiles at ISS-S. Figure 12b shows a sequence of these waves wherein 100 m amplitude

variations in aerosol depth occur once every 3 mins. The first three waves successively grow in amplitude, and the 4th and 5th waves appear to have broken down into turbulence or smaller scale waves. The Richardson number, here evaluated from our time-height data, is near critical over a deep layer. However, since the time-height temperature and wind data lack the vertical and temporal resolution to resolve fine scale structures in the CAP, it is likely that the minimum values for Ri are lower than those calculated here.

Later, at 1100 UTC 3 December (Fig. 2.12c), the winds aloft reach their peak strength of 15 m s^{-1} and strong shear extends over the depth of the CAP. In fact, the shear is now enhanced by a counter current of northerly flow near the surface associated with the southward motion of the CAP. Correspondingly, Ri is reduced to near its critical value over most of the CAP depth. The waves now have amplitudes upwards of 200 m, and appear to loft aerosols deep into the clear air above. Compared to earlier, the wave structures are more chaotic and less clearly billow shaped. The dominant period of these waves remains 3 mins.

As evident in earlier results as well, it is interesting to note that the CAP is not destroyed despite the strong wind shear, near critical Ri, and active KHW. Competing processes must offset the turbulent heat fluxes arising from the KHW, which would tend to remove the CAP stratification over time. For example, downward turbulent heat fluxes of 120 W m^{-2} during the warm frontal advances were evident with the large jumps in surface temperature (not shown). We suspect that the vertical differential temperature advection across the CAP is responsible for maintaining its strength. For example, the northerly flow at the surface is continually feeding cold-air from deeper portions of the CAP into the region surrounding ISS-S, where these waves are active.

2.4.7 Basin-Scale Internal Waves

A noticeable feature of the Disturbance Phase of IOP-1 is the presence of SLV-scale internal waves within the CAP. Relatively low frequency, long (basin-scale) wavelength phenomena such as baroclinic seiches are known to occur within stratified lakes (Csanady 1972; Monismith 1985), but have not been thoroughly documented in atmospheric CAPs (Largeron et al. 2013).

Such basin-scale internal waves (BSIW) are manifest during IOP-1 as oscillations in the depth of the CAP superimposed upon the broader trends associated with the passage of the short-wave trough (Fig. 2.13a). Visual inspection of the potential temperature and aerosol backscatter profiles suggests that the waves have a period of 3 hrs and arrive with a steep increase in depth but then depart with a more gradual thinning. We attempt to isolate the properties of these BSIW by applying a 1-5 h band-pass filter to independent time series of surface pressure (1-min resolution) and the 1500-1800 m layer-averaged meridional wind and potential temperature at ISS-S (Fig. 2.13b). This filter removes lower frequency variations associated with synoptic-scale and diurnal fluctuations, high frequency variations due to microscale processes (e.g., KHW), and preserves the frequencies associated with the waves of interest.

The filtered data show that increases in the depth of the aerosol layer tend to correspond to increases in the surface pressure and decreases in layer mean temperature (Fig. 2.13b, i.e., a deeper CAP with higher aerosol concentration is accompanied by higher pressure and lower temperature). The meridional component of the wind generally reverses during the wave cycle, oscillating between more northerly and southerly along valley flow. This wind reversal is important in redistributing pollution within the CAP.

These oscillations are coherent over the scale of the SLV, appearing with comparable amplitude (1 hPa) at each of the 7 ISFS sites (Fig. 2.13c). There is an approximate 1 hr time lag between ISFS1 and ISFS7, which are at the north and south ends of the valley, respectively, and separated by about 31.4 km (see Fig. 2.1). Spectral analysis of these time-series confirms that the dominant BSIW period is between 3 and 4 hrs (not shown).

To further demonstrate the link between surface pressure and CAP structure, we examine one of these waves as it passes over the Harker's Ridge transect between 0515 and 0845 UTC 2 December (Fig. 2.14a). From these profiles it is apparent that the oscillation takes the form of rises and falls in the depth of the surface-based layer of cold air relative to a mean state. The maximum amplitude in temperature variations occur within the layer between 1500 and 1800 m, which coincides with the transition layer that separates the surface-based nocturnal inversion from the capping layer aloft. This transition layer is apparent in the individual profiles as a nearly adiabatic lapse rate generally centered at about 1600 m.

Following Li et al. (2009), the pressure perturbation at the surface can be approximated from the temperature anomalies along Harkers Ridge during the CAP oscillations using

$$P'(z = 0) \approx \frac{\bar{\rho}g}{\bar{T}} \int_{z=0}^{z=H} T'(z) \, dz \qquad (2.7)$$

where $\bar{T}$ is the mean temperature, $T'(z)$ is the perturbation temperature at each height, $\bar{\rho}$ is the mean density and H is the depth of the profile. The computed pressure anomalies (Fig. 2.14b) confirm that as the CAP rises (falls) the surface pressure increases (decreases) by about 0.4 hPa, giving a total amplitude of about 0.8 hPa, which is

consistent with the pressure perturbations measured throughout the valley (Fig. 2.13c). The computed perturbations also capture the steep initial rise followed by the more gradual thinning seen in the aerosol backscatter (Fig. 2.13a) as well as the variations in pressure observed at the ISFS sites near 0600 UTC (Fig. 2.13c).

The exact causal mechanism and nature of these BSIW are as of yet unknown. They may arise due to any of a number of forcings acting upon the stably stratified CAP. For example, it is possible that they are a response to an external forcing, such as the increasing winds aloft, or an internal forcing, such as katabatic flows or lake breezes that are known to occur within the SLV during CAPs. Regardless of their source, these BSIW are an important factor in local changes in the CAP. For example it is possible that these waves alter the CAP internal force balance and contribute to the advance and retreat of the cold air. Interestingly such phenomena do not appear to be previously documented in the CAP literature.

2.5 Summary and Conclusions

In this paper we have documented the complex evolution of a CAP that was disturbed by a passing short-wave trough. We show that the initially horizontally homogenous stratified air mass was disrupted by a series of along valley displacements, frontal passages, internal waves, and turbulent mixing. To synthesize these elements of the trough-CAP interaction we present here a schematic of the CAP evolution (Fig. 2.15) using insights from the observational data and the numerical simulation.

The stages of the CAP disruption are as follows:

(a) At the onset, a quiescent and horizontally homogenous two-layered CAP resides

in the valley. Synoptic scale warming aloft modulates the upper stable layer, while the surface based inversion is affected by diurnally varying sensible heat fluxes. The layers are partially separated by a residual layer of weaker stability (Fig. 2.15a).

(b) Winds above the CAP increase as a disturbance approaches. A mountain wave develops in the stratified cross barrier flow over the upstream topography, generating downslope warming and accelerated winds. The plunging flow displaces and erodes the surface inversion, forming a frontal interface. Increased shear leads to KHW, especially at the top of the surface inversion layer (Fig. 2.15b).

(c) The CAP tilts upward in the down wind direction, establishing a force balance between the internal hydrostatic pressure gradient, the external pressure gradient, and the wind stress acting on the CAP. As the CAP tilts, its southern edge advances through the valley as a warm front, providing warmer, windier, and cleaner air to southern locales (Fig. 2.15c).

(d) Some perturbation, such as a temporary reduction in wind stress or a wave modulated change in depth, disrupts the CAP force balance. The CAP tilt partially collapses due to the unbalanced internal pressure gradient, sending a shallow density current propagating upwind through the valley and restoring the surface based inversion. Enhanced KHW mixing occurs in the wake of the density current (Fig. 2.15d).

Stages b-d repeat as the force balance is restored leading to a sequence of frontal advances and retreats over upwind portions of the valley. Meanwhile northern locales remain within the CAP throughout the evolution. Finally, the winds aloft diminish and the CAP tilt collapses for a final time, restoring horizontally homogenous and quiescent

CAP conditions throughout the valley.

While this simple schematic summary relies primarily on data from IOP-1, it nonetheless fits well with observations from many other CAPs, which are common in the SLV. For example, a similar sequence of step-like frontal temperature changes was observed at ISS-S during PCAPS IOP-4 (not shown). Moreover, many of the details of the IOP-1 CAP are similar to the evolution of the CAPs described by Whiteman et al. (2001) and Flamant et al. (2006). Namely, a CAP is displaced in strong prefrontal downslope winds leading to a warm front that provides partial or complete valley ventilation. In the present case, the CAP displacement is reversible, and CAP conditions are restored after winds abate. In other instances, however, a CAP may be completely removed, suggesting that irreversible turbulent mixing and spillover at the downwind end of the basin play an important role in CAP destruction.

We conclude by noting that many of the key features in the trough-CAP interaction are meso- and microscale processes that are typically either poorly resolved or altogether unresolved in numerical forecast guidance. These unresolved processes strongly impact the CAP, and thus the forecasts for air quality. To further address the sensitivity of CAP removal to mountain waves, hydraulic jumps, KHW, and BSIW, a companion study using a larger set of idealized Large-Eddy Simulations than the single simulation used to generate Fig. 2.8 will be forthcoming.

2.6 References

Barnes, S. L., 1964: A technique for maximizing details in numerical weather map analysis. *J. Appl. Meteor.,* **3,** 396–409.

Beard, J. D., C. Beck, R. Graham, S. Packham, M. Traphagan, R. Giles, and J. G. Morgan, 2012: Winter temperature inversions and emergency department visits for

Asthma in Salt Lake County, Utah, 2003-2008. *Env. Health Pers*., **120,** 1385-1390.

Bell, R. C., and R. Thompson, 1980: Valley ventilation by cross winds. *J. Fluid Mech.* **96,** 757-767.

Chen, Y., F. L. Ludwig, and R.L Street, 2004: Stably stratified flows near a notched Transverse Ridge across the Salt Lake Valley. *J. Appl. Meteor.,* **43,** 1308-1328.

Csanady. G. T., 1972: Response of large stratified lakes to wind. *J. Phys. Oceanogr.,* **2,** 3–13.

Durran, D. R., 1986: Another look at downslope windstorms. Part I: The development of analogs to supercritical flow in an infinitely deep, continuously stratified fluid. *J. Atmos. Sci.* **43,** 2527–254.

Flamant, C. , P. Drobinski, N. Furger, B. Chimani, S. Tschannett, R. Steinacker, A. Protat, H. Richner, S. Gubser, and C. Haberli, 2006: Föhn/CAP interactions in the Rhine valley during MAP IOP 15. *Quart. J. Roy. Meteorol. Soc.,* **132**, 3035-3058.

Fernando, H. J. S., 1991: Turbulent mixing in stratified fluids. *Annu. Rev. Fluid Mech.* **23,** 455-493.

Gillies, R. R., Wang, S. Y., Booth M. R., 2010: Atmospheric scale interaction on wintertime Intermountain West low-level inversions. *Wea. Forecasting*, **25,** 1196-1210.

Gubser, S., and H. Richner, 2001: Investigations into mechanisms leading to the removal of the cold-pool in foehn situations. Extended abstract, *MAP Meeting at Schliersee. MAP Newsletter 15*. Available at:http://www.map.meteoswiss.ch/map-doc/NL15/gubser2.pdf

Horel, J., M. Splitt, L. Dunn, J. Pechmann, B. White, C. Ciliberti, S. Lazarus, J. Slemmer, and D. Zaff, 2002: Mesowest: Cooperative mesonets in the Western United States. *Bull. Amer. Meteor. Soc.,* **83,** 211-225

Jiang, Q., J.D. Doyle, S. Wang, R. B. Smith, 2007: On boundary layer separation in the lee of mesoscale topography. *J. Atmos. Sci.*, **64,** 401–420.

Kim, J., and L. Mahrt, 1992: Simple formulation of turbulent mixing in the stable free atmosphere and nocturnal boundary layer. *Tellus,* **44,** 381–394.

Largeron, Y., C. Staquet, and C. Chemel, 2013: Characterization of oscillatory motions in the stable atmosphere of a deep valley. *Bound.-Layer Meteor.,* **148,** 439-454

Lareau, N. P., E. Crosman, C. D. Whiteman, J. D. Horel, S. W. Hoch, W. O. J. Brown, and T. W. Horst, 2013: The persistent cold-air pool study. *Bull. Amer. Meteor. Soc.*, **94,** 51–63.

Lee, T. J., and R. A. Pielke, 1989: Influence of cold pools downstream of mountain barriers on downslope winds and flushing. *Mon. Wea. Rev.*, **117,** 2041-2058.

Lee, J. T., R. E. Lawson Jr., and G. L. Marsh, 1987: Flow visualization experiments on stably stratified flow over ridges and valleys. *Meteor. Atmos. Phys.,* **37,** 183-194.

Li, Y., R. B. Smith, and V. Grubišić, 2009: Using surface pressure variations to categorize diurnal valley circulations: Experiments in Owens Valley. *Mon. Wea. Rev.,* **137,** 1753–1769.

Malek, E., T. Davis, R. S. Martin, and P. J. Silva, 2006: Meteorological and environmental aspects of one of the worst national air pollution episodes in Logan, Cache Valley, Utah, USA. *Atmos. Res.,* **79,** 108-122.

Marht, L., and D. Vickers, 2002: Contrasting vertical structures of nocturnal boundary layers. *Bound.-Layer Meteor.,* **105,**351-363.

Markowski, P., and Y. Richardson, 2010: *Mesoscale Meteorology in Midlatitudes.* John Wiley & Sons, Ltd. 430, pp.

Monismith S. G., 1985: Wind forced motions in stratified lakes and their effects on mixed-layer shear. *Limnol. and Oceanogr.,* **30,** 771-783.

Nappo, C. J., 2002: *An Introduction to Atmospheric Gravity Waves.* Academic Press. 279 pp.

Newsom, R. K., and R. M. Banta, 2003. Shear-flow instability in the stable nocturnal boundary layer as observed by Doppler lidar during CASES-99. *J. Atmos. Sci.* **60,** 16–33.

Pataki, D. E., B. J. Tyler, R. E. Peterson, A. P. Nair, W. J. Steenburgh, and E. R. Pardyjak, 2005: Can carbon dioxide be used as a tracer of urban atmospheric transport? *J. Geophys. Res.,* **110,** D15102.

Pataki, D. E., D. R. Bowling, J. R. Ehleringer, J. M. Zobitz, 2006: High resolution atmospheric monitoring of urban carbon dioxide sources. *Geophys. Res. Let.,* **33,** L03813.

Petkovšek, Z., 1992: Turbulent dissipation of cold air lake in a basin. *Meteor. Atmos. Phys.,* **447,** 237-245.

Petkovšek, Z., and T. Vrhovec (1994): Note on the influences of inclined fog lakes on the air pollution in them and on the irradiance above them. *Meteor. Z.,* **3,** 227-23.

Pinto, J. O., D. B. Parsons, W. O. J. Brown, S. Cohn, N. Chamberlain, and B. Morley, 2006: Coevolution of down-valley flow and the nocturnal boundary layer in complex terrain. *J. Appl. Meteor.,* **45,**1429-1449.

Pope, III C. A., M. Ezzati, and D. W. Dockery, 2009: Fine-particulate air pollution and life expectancy in the United States. *New Engl. J. Med.,* **360,** 376-386.

Rakovec, J., J. Merše, S. Jernej, and B. Paradiž, 2002: Turbulent dissipation of the cold-air pool in a basin: Comparison of observed and simulated development. *Meteor. Atmos. Phys.,* **79,** 195-213.

Reddy, P. J., D. E. Barbarick, and R. D. Osterburg, 1995: Development of a statistical model for forecasting episodes of visibility degradation in the Denver metropolitan area. *J. Appl. Meteor*., **34,** 616-625.

Reeves, H. D., and D. J. Stensrud, 2009: Synoptic-scale flow and valley cold pool evolution in the Western United States. *Wea. Forecasting,* **24,**1625-1643.

Reeves, H. D., K. L. Elmore, G. S. Manikin, and D. J. Stensrud, 2011: Assessment of forecasts during persistent valley cold pools in the Bonneville basin by the North American Mesoscale model. *Wea. Forecasting,* **26,** 447-46.

Schönlieb, C.-B., 2012: Applying modern PDE techniques to digital image restoration. Mathworks Newsletter. Available at: http://www.mathworks.com/company/newsletters/articles/applying-modern-pde-techniques-to-digital-image-restoration.html

Silcox, G. D., K. E. Kelly, E. T. Crosman, C. D. Whiteman, and B. Allen, 2012: Wintertime PM2.5 concentrations in Utah's Salt Lake Valley during persistent, multiday cold-air pools. *Atmos. Environ.,* **46,** 17-24.

Simpson, J. E., 1997: *Gravity Currents in the Environment and the Laboratory*. Cambridge University Press. 244 pp.

Skamarock, W. C., J. B. Klemp, J. Dudhia, D. O. Gill, D. M. Barker, M. G. Duda, X. Huang, W. Want, and J. G. Power, 2008: A description of the advanced research WRF version 3. NCAR Tech. Note, NCAR/TN-475+STR, 113 pp.

Strang, E. J., and H. J. S. Fernando, 2001a) Entrainment and mixing in stratified shear flows. *J. Fluid. Mech.,* **428,** 349-386.

Strang, E. J., and H. J. S. Fernando, 2001b: Vertical mixing and transports through a stratified shear layer. *J. Phys. Oceanogr.,* **31,** 2026-2048.

Sun, J., S. P. Burns, D. H. Lenschow, R. Banta, R. Newsom, R. Coulter, S. Frasier, T. Ince, C. Nappo, J. Cuxart, W. Blumen, X. Lee, and X.-Z. Hu X, 2002: Intermittent

turbulence associated with a density current passage in the stable boundary layer, *Bound.-Layer Meteor.,* **105,** 199–219.

Sun, J., D. H. Lenschow, L. Marht, and C. Nappo, 2013: The relationships among wind, horizontal pressure gradient, and turbulent momentum transport during CASES-99. *J. Atmos. Sci.*, **70,** 3397-3414.

Tampieri, F., and J. C. R. Hunt, 1985: Two-dimensional stratified fluid flow over valleys: Linear theory and laboratory investigation. *Bound.-Layer Meteor.,* **32,** 257-279.

Tyndall, D. P., and J. D. Horel, 2013: Impacts of mesonet observations on meteorological surface analyses. *Wea. Forecasting,* **28,** 254–269.

U.S. EPA, cited 2013: National Ambient Air Quality Standards (NAAQS). [available online at http://www.epa.gov/air/criteria.html.]

Vosper, S. B., 2004: Inversion effects on mountain lee waves. *Quart. J. Roy. Meteor. Soc.,* **130,** 1723–1748.

Vrhovec, T., and A. Hrabar, 1996: Numerical simulations of dissipation of dry temperature inversions in basins. *Geofizika,* **13,** 81-96.

Wei, L., Z. Pu, and S. Wang, 2013: Numerical simulation of the life cycle of a persistent wintertime inversion over Salt Lake City. *Bound.-Layer Meteor.,* **148,** 399-418

White, B. L., and K. R. Helfrich, 2012: A general description of a gravity current front propagating in a two-layer stratified fluid. *J. Fluid. Mech.,* **711,** 545-575.

Whiteman, C. D., X. Bian, and S Zhong, 1999: Wintertime evolution of the temperature inversion in the Colorado Plateau Basin. *J. Appl. Meteor.,* **38,** 1103-1117.

Whiteman, C. D., S. Zhong, W. J. Shaw, J. M. Hubbe, X. Bian, and J. Mittelstadt, 2001: Cold pools in the Columbia basin. *Wea. Forecasting,* **16,** 432-447.

Wolyn, P. G., and T. B. McKee, 1989: Deep stable layers in the intermountain Western United States. *Mon. Wea. Rev.* **117,** 461-472.

Young, J., 2013: Investigation of wintertime cold-air pools and aerosol layers in the Salt Lake Valley using a laser ceilometer. MS Thesis. University of Utah. 118 pp.

Zängl, G., 2003: The impact of upstream blocking, drainage flow and the geostrophic pressure gradient on the persistence of cold-air pools. *Quart. J. Roy. Meteor. Soc.,* **129,** 117–137.

Zängl, G., 2005: Winterime cold-air pools in the Bavarian Danube Valley Basin: Data analysis and idealized numerical simulations. *J. Appl. Meteor.,* **44,** 1950-1971.

Zardi, D. and C. D. Whiteman, 2013: Diurnal Mountain Wind Systems. *Mountain Weather Research and Forecasting: Recent Progress and Current Challenges,* F. K. Chow, S. F. J. De Wekker, and B. Snyder, Ed., Springer, 35-119.

Zhong, S., C. D. Whiteman, X. Bian, W. J. Shaw, and J. M. Hubbe, 2001: Meteorological processes affecting evolution of a wintertime cold air pool in a large basin. *Mon. Wea. Rev.,* **129,** 2600-2613.

Zhong, S., X. Bian, C. D. Whiteman, 2003: Time scale for cold-air pool breakup by turbulent erosion. *Meteor. Z.,* **12,** 229-23.

Fig. 2.1 Topographic map of the Salt Lake Valley, UT showing instrument locations during the Persistent Cold-Air Pool Study. The inset shows the location of the Salt Lake Valley relative to the western United States. Further details are provided in the text.
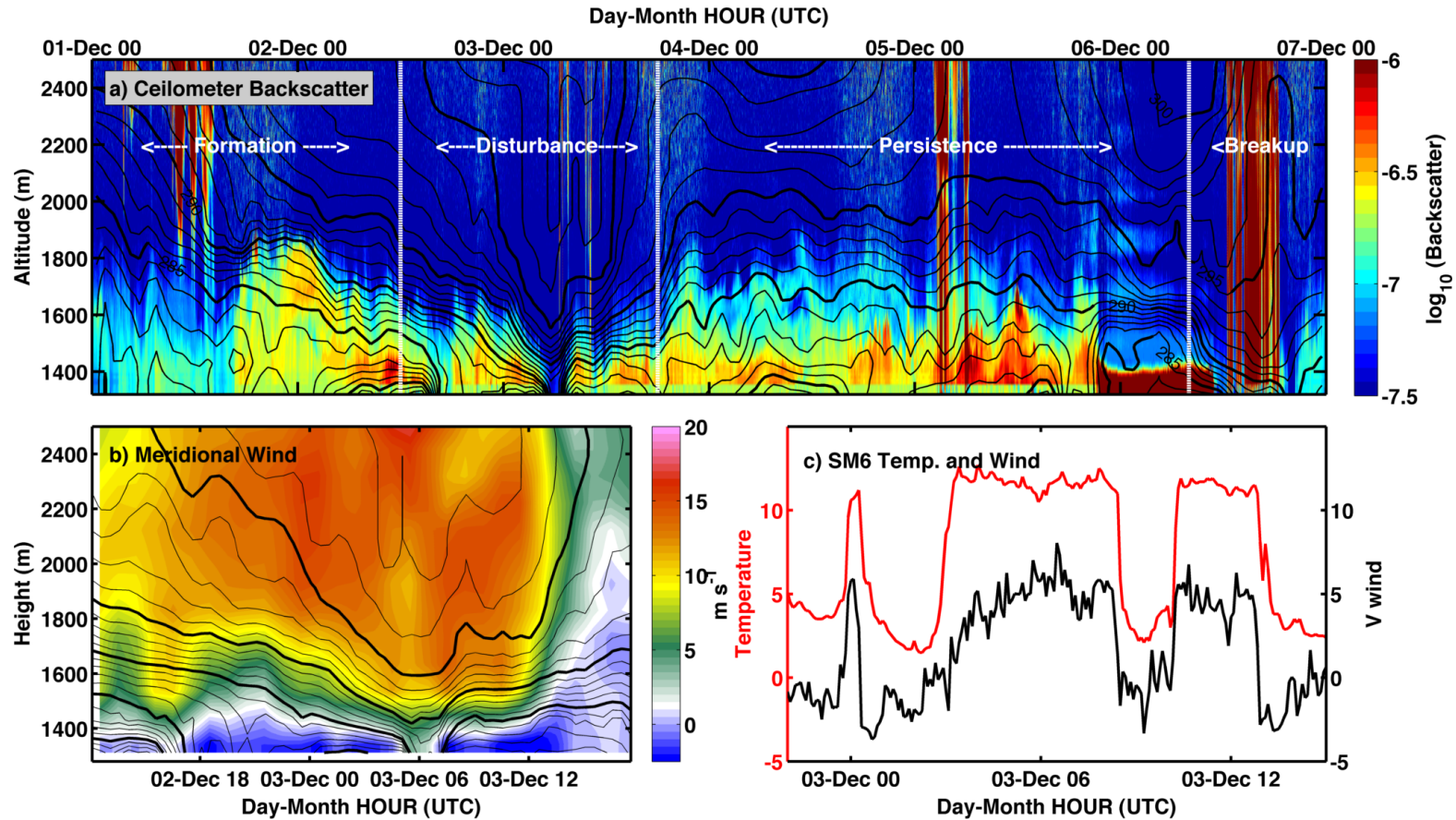
Fig. 2.2 Overview of PCAPS IOP-1. (a) Time-height profile at ISS-S of potential temperature (contours at 1 K interval) and aerosol backscatter (shading) where yellow-orange (blue) shades reflect high (low) aerosol concentrations and dark red shades denote hydrometeors. (b) Time height profile of meridional wind (shading) and potential temperature during the Disturbance Phase. (c) Surface temperature and meridional wind at SM6, which is located at the base of the Traverse Mountains in the southeast corner of the Salt Lake Valley.
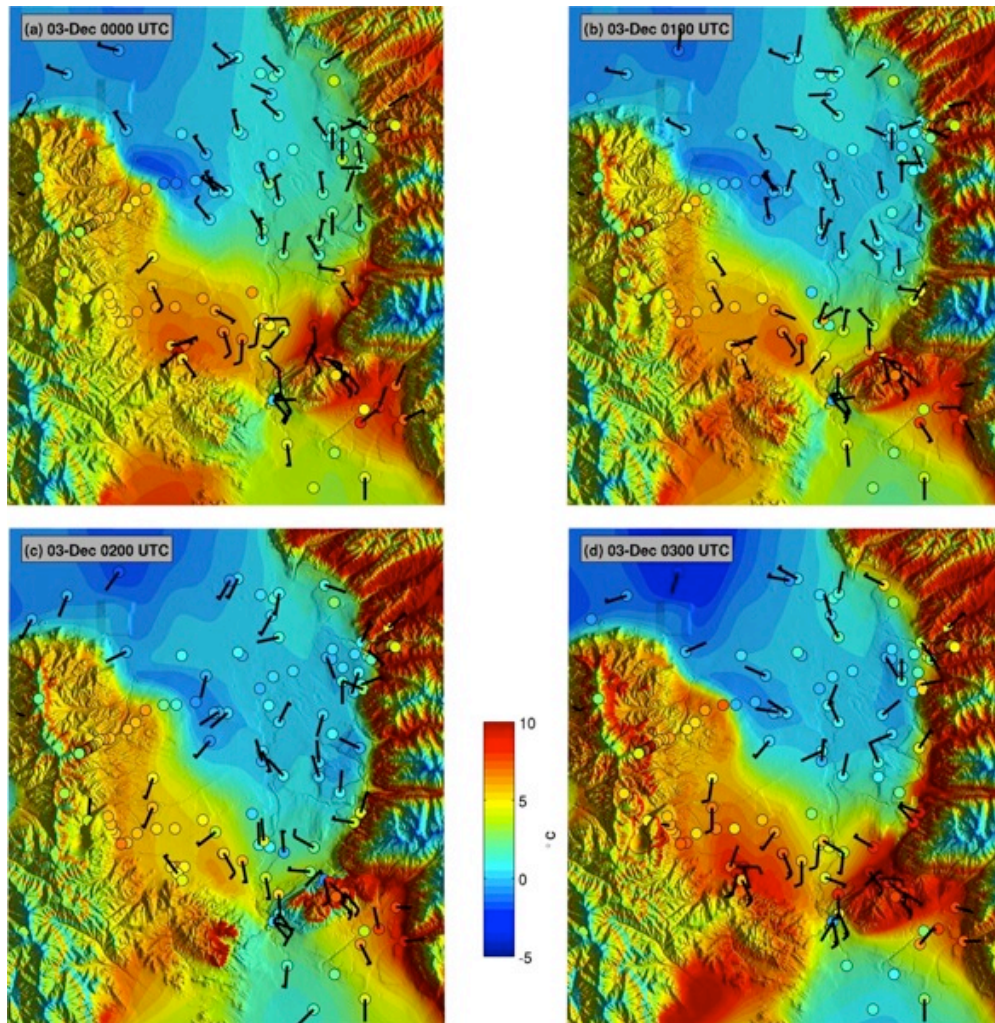
Fig. 2.3 Hourly surface temperature analyses (color shaded) from 0000-0300 UTC 3 December 2010. Surface temperature observations (filled circles shaded according to the scale) and vector wind (wind barbs in m/s where a full barb denotes 5 m/s). a) 0000 UTC. b) 0100 UTC. c) 0200 UTC. d) 0300 UTC.
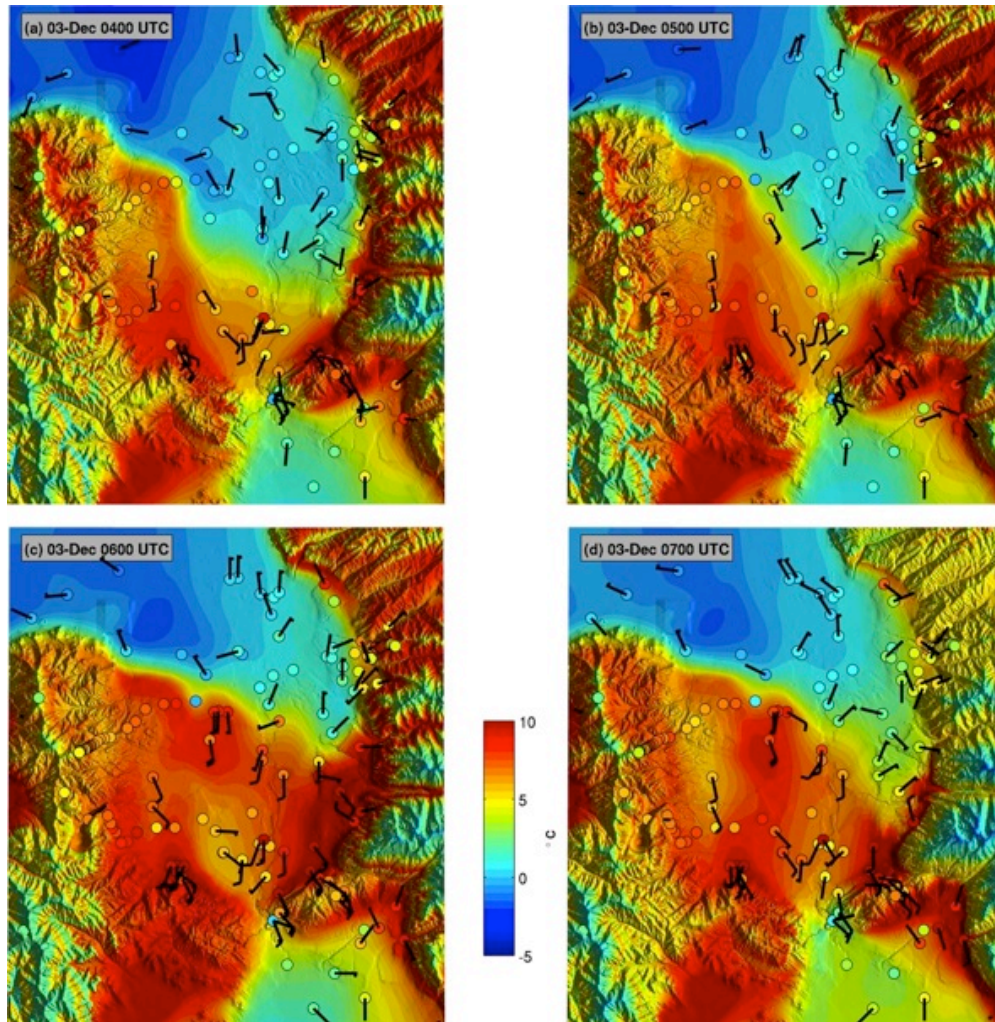
Fig. 2.4 Hourly surface temperature analyses (color shaded) from 0400-0700 UTC 3 December 2010. Surface temperature observations (filled circles shaded according to the scale) and vector wind (wind barbs in m/s where a full barb denotes 5 m/s). a) 0400 UTC. b) 0500 UTC. c) 0600 UTC. d) 0700 UTC.
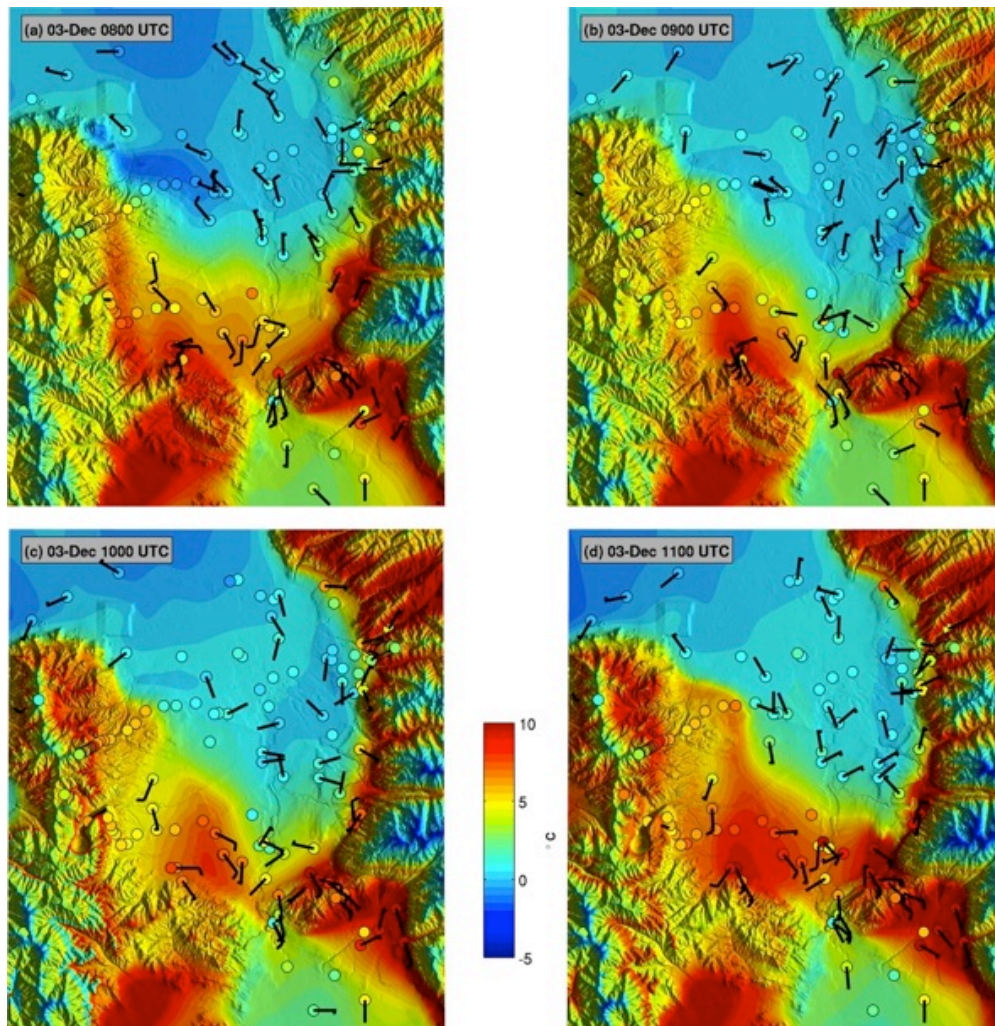
Fig. 2.5 Hourly surface temperature analyses (color shaded) from 0800-1100 UTC 3 December 2010. Surface temperature observations (filled circles shaded according to the scale) and vector wind (wind barbs in m/s where a full barb denotes 5 m/s). a) 0800 UTC. b) 0900 UTC. c) 1000 UTC. d) 1100 UTC.
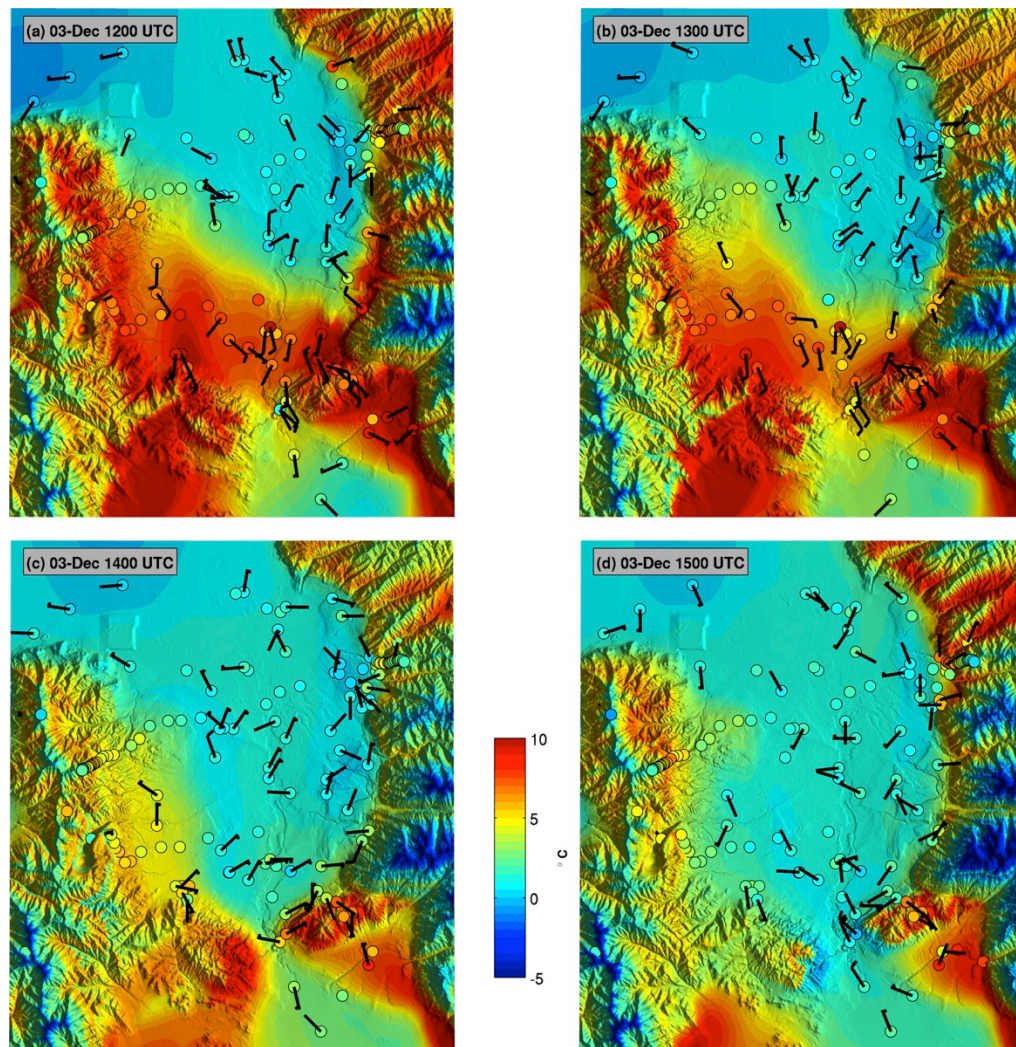
Fig. 2.6 Hourly surface temperature analyses (color shaded) from 1200-1500 UTC 3 December 2010. Surface temperature observations (filled circles shaded according to the scale) and vector wind (wind barbs in m/s where a full barb denotes 5 m/s). a) 1200 UTC. b) 1300 UTC. c) 1400 UTC. d) 1500 UTC.
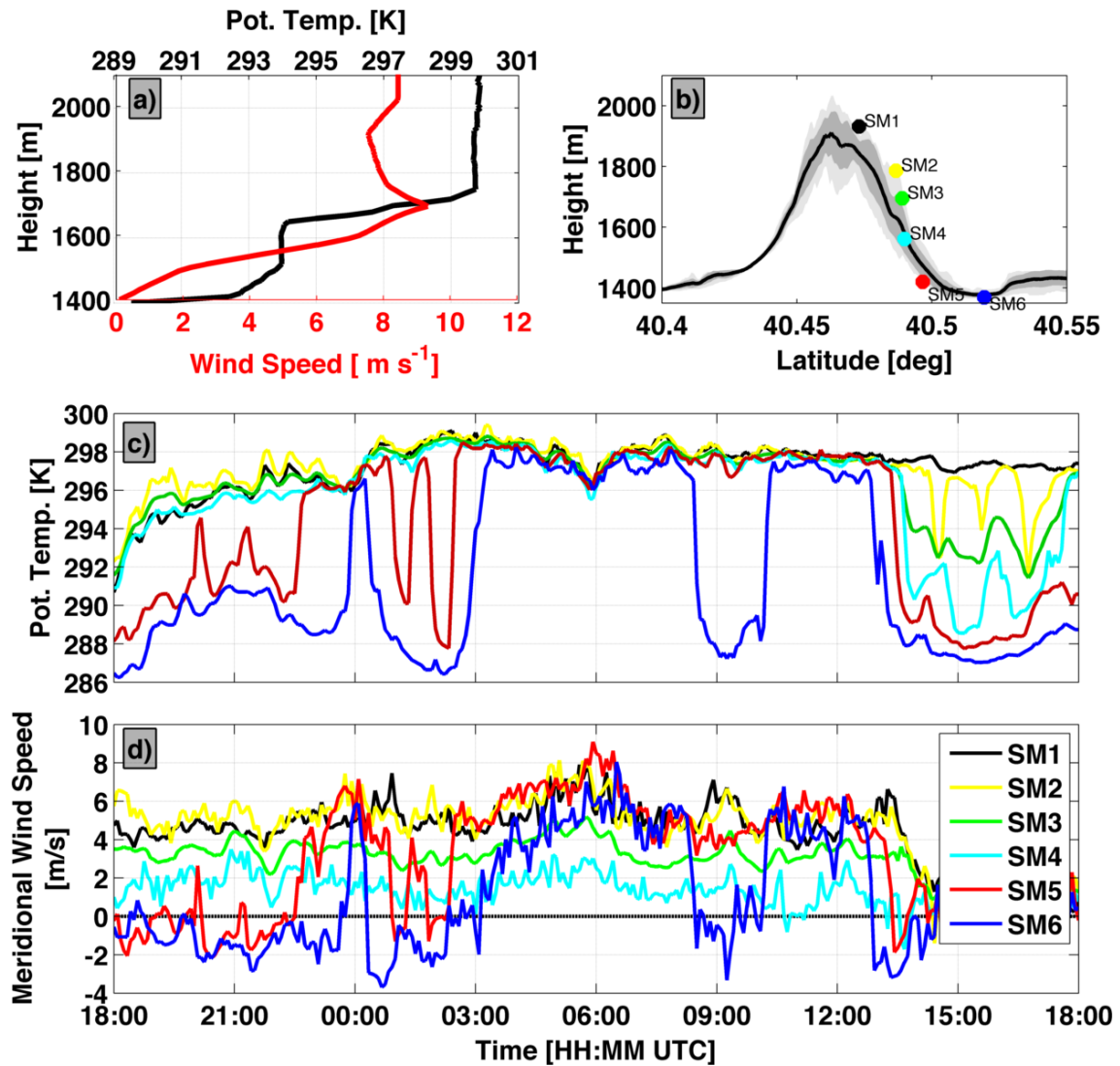
Fig. 2.7 Properties of the mountain wave forming over the Traverse Mountains. (a) Sounding upstream of the SLV at Lehi, UT at 0600 UTC 3 December showing potential temperature (black) and meridional wind (red). (b) Traverse Mountain cross-section showing station locations and the terrain variability (shading). (c) Potential temperature and (d) meridional wind time series for each of the 6 SM stations.
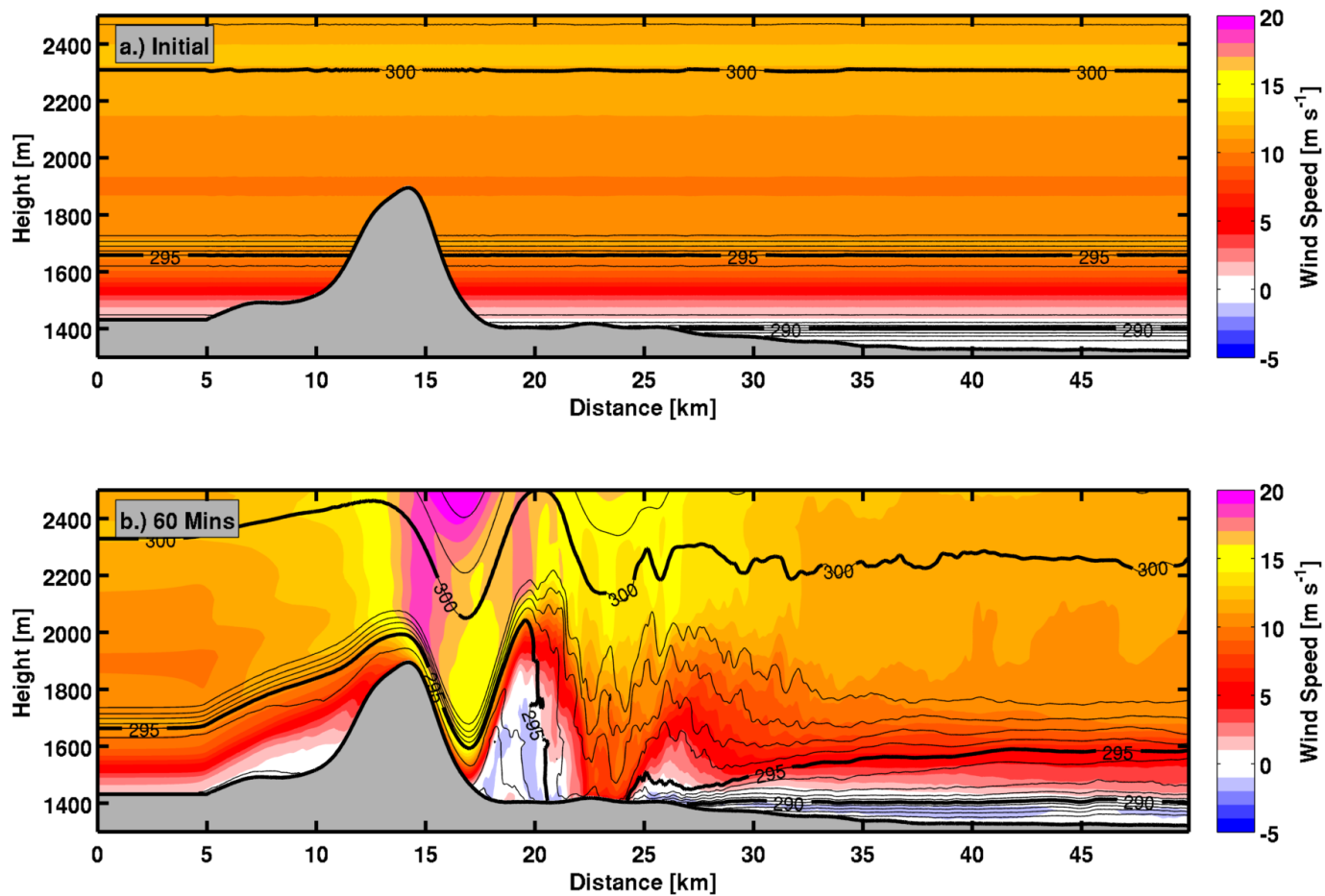
Fig. 2.8 Large-Eddy Simulation of a mountain wave disrupting the two-layered CAP. Panels show wind speed (colors) and potential temperature (contours, bold every 5 K) at (a) the initialization and (b) after 1-h of simulation. The terrain cross section is along the black line if Fig. 2.1, with north to the right.
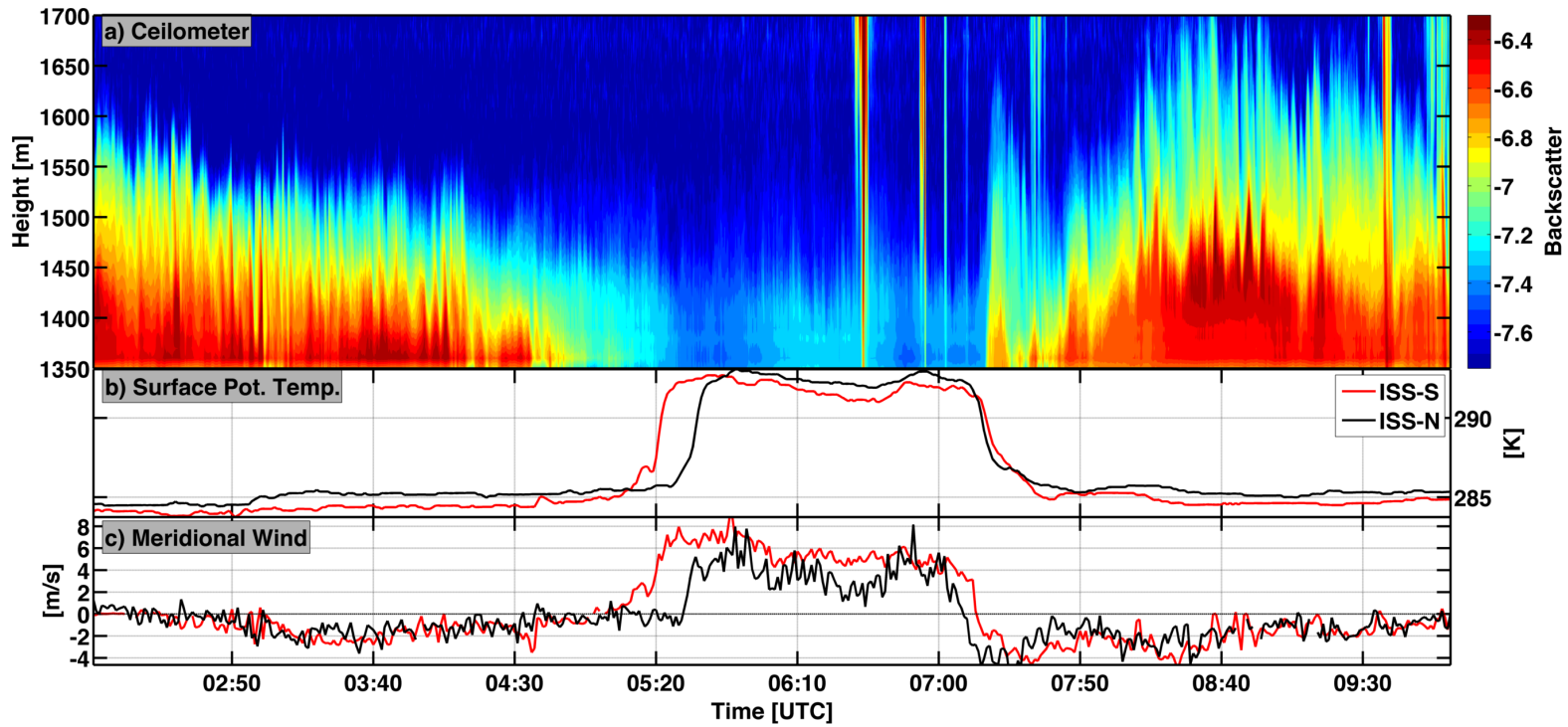
Fig. 2.9 Time series data during the warm and cold frontal passages at ISS-S and ISS-N on 3 December 2010. (a) Laser ceilometer backscatter, (b) potential temperature, and (c) meridional wind.
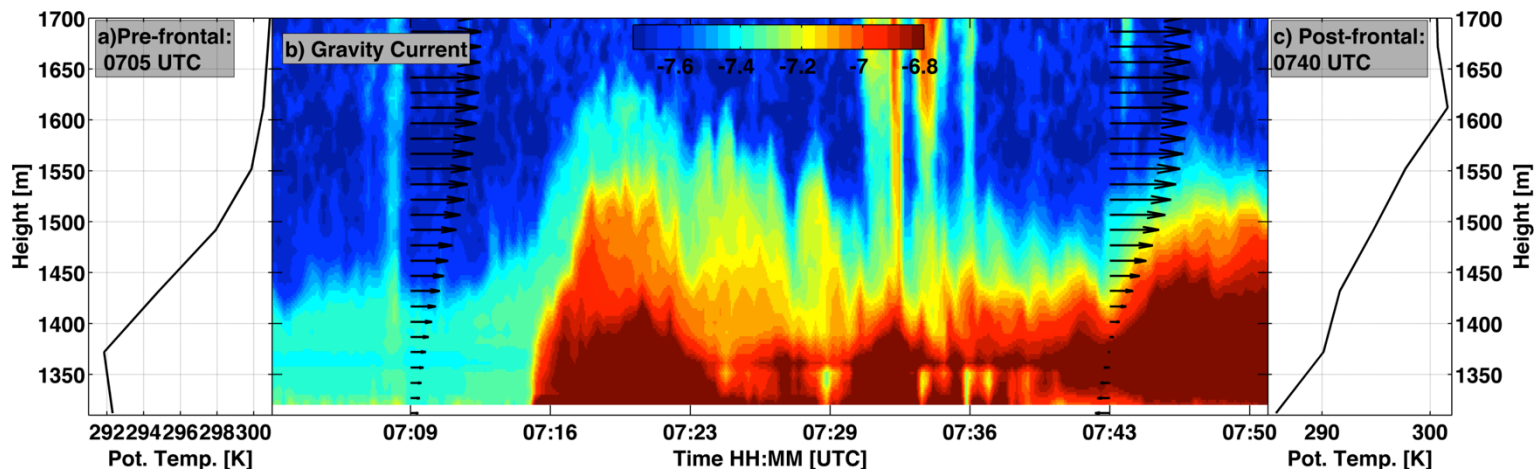
Fig. 2.10 Detail of the gravity current passage at ISS-S. (a) Potential temperature profile at 0705 UTC preceding the cold frontal passage, (b) ceilometer backscatter and meridional wind profiles from the radar wind profiler, and (c) post-cold frontal potential temperature profile at 0740 UTC. Profile data are retrieved from the time-height data set.
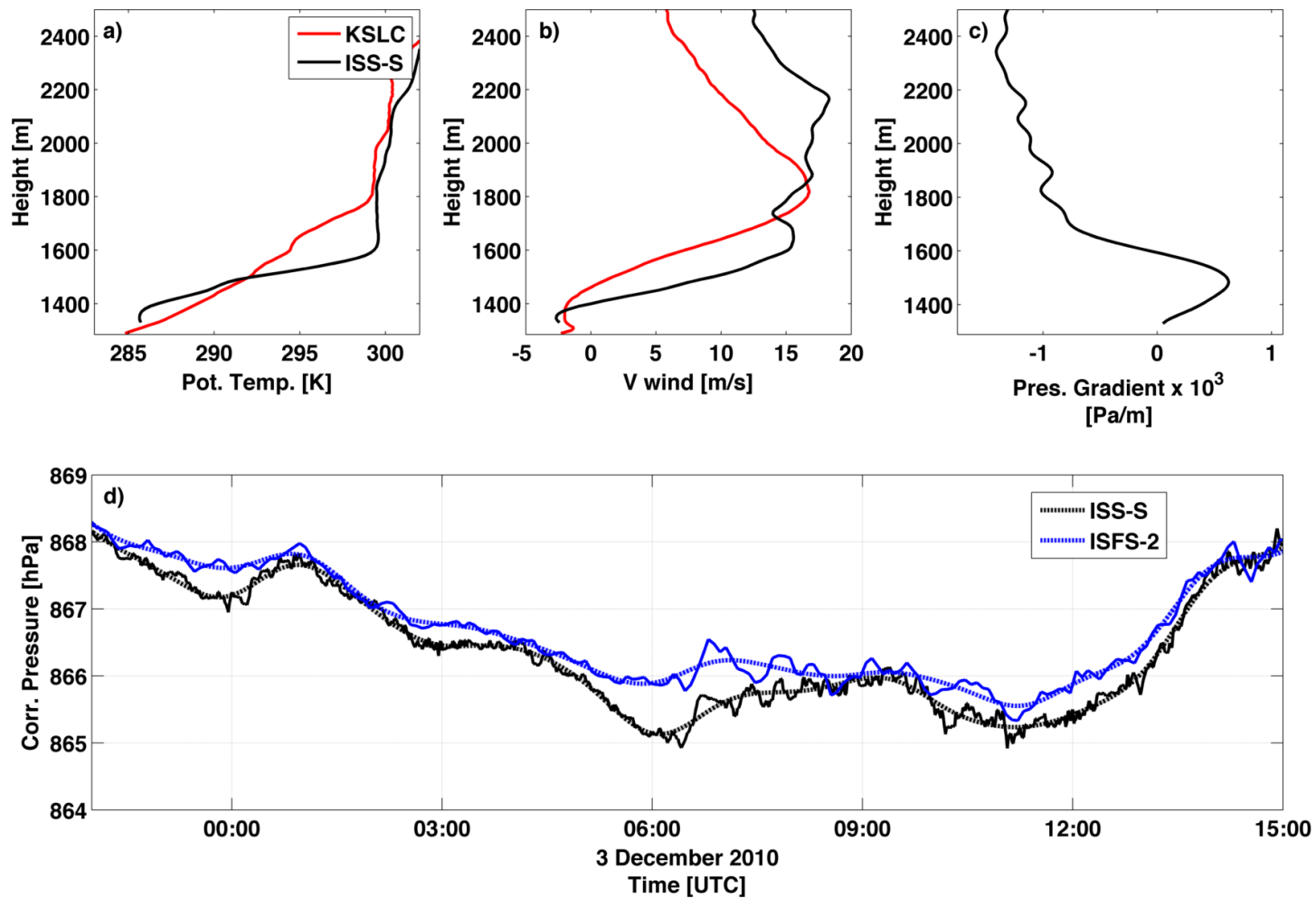
Fig. 2.11 Vertical profiles of (a) potential temperature and (b) meridional wind launched at 1115 UTC at KSLC (red lines) and ISS-S (black lines). (c) The pressure gradient between KSLC and ISS-S. (d) Time series of elevation corrected surface pressure for ISS-S (black) and ISFS-2 (blue). The raw and smoothed data are shown for each site.
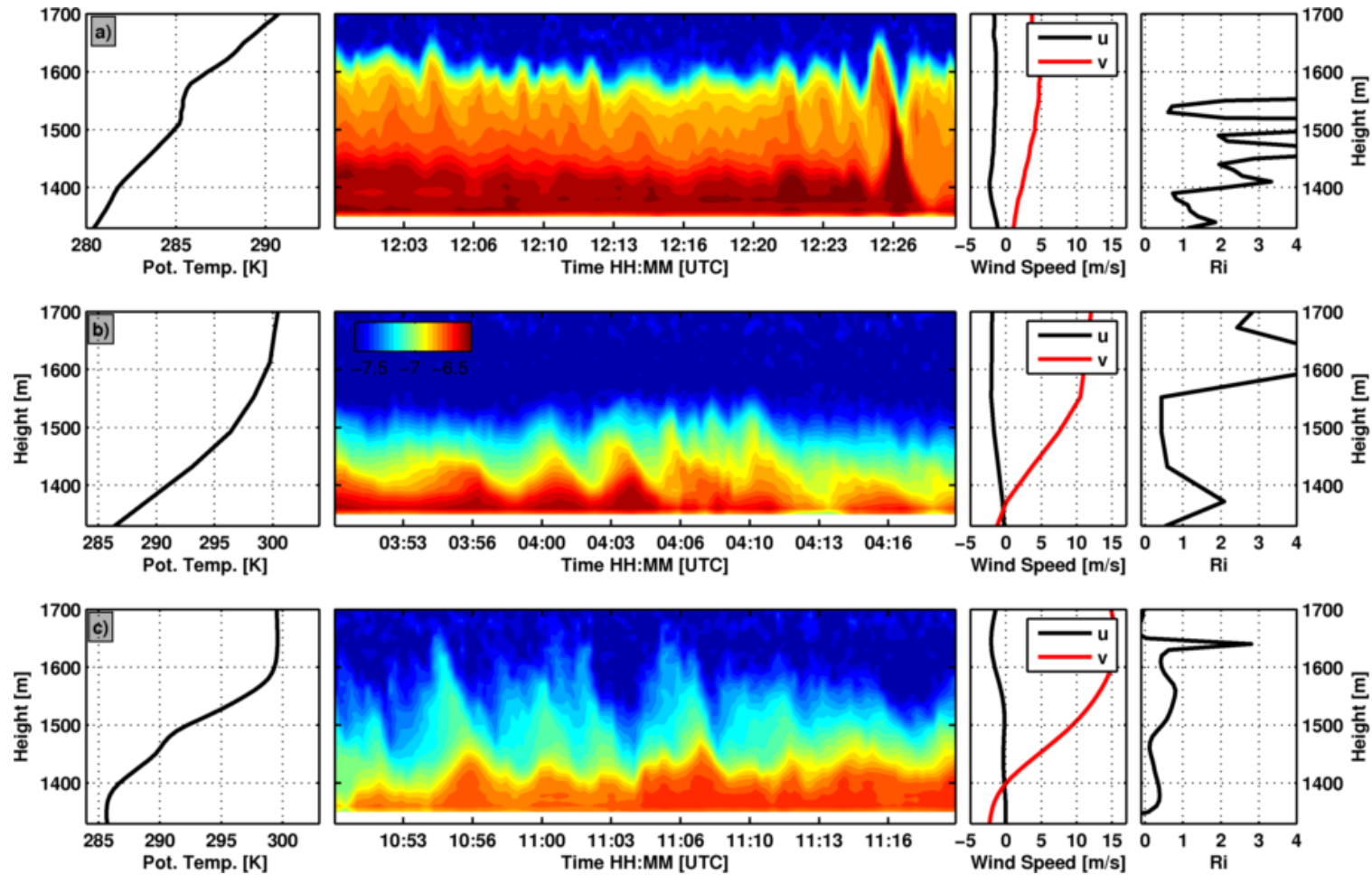
Fig. 2.12 Kelvin Helmholtz waves at: (a) 1200 UTC 2 December, (b) 0400 UTC 3 December, and (c) 1100 UTC 3 December. First column: potential temperature. Second column: aerosol backscatter. Third column: wind speed. Last column: gradient Richardson number. All data are from ISS-S excepting the profile data in the first row, which is from KSLC.
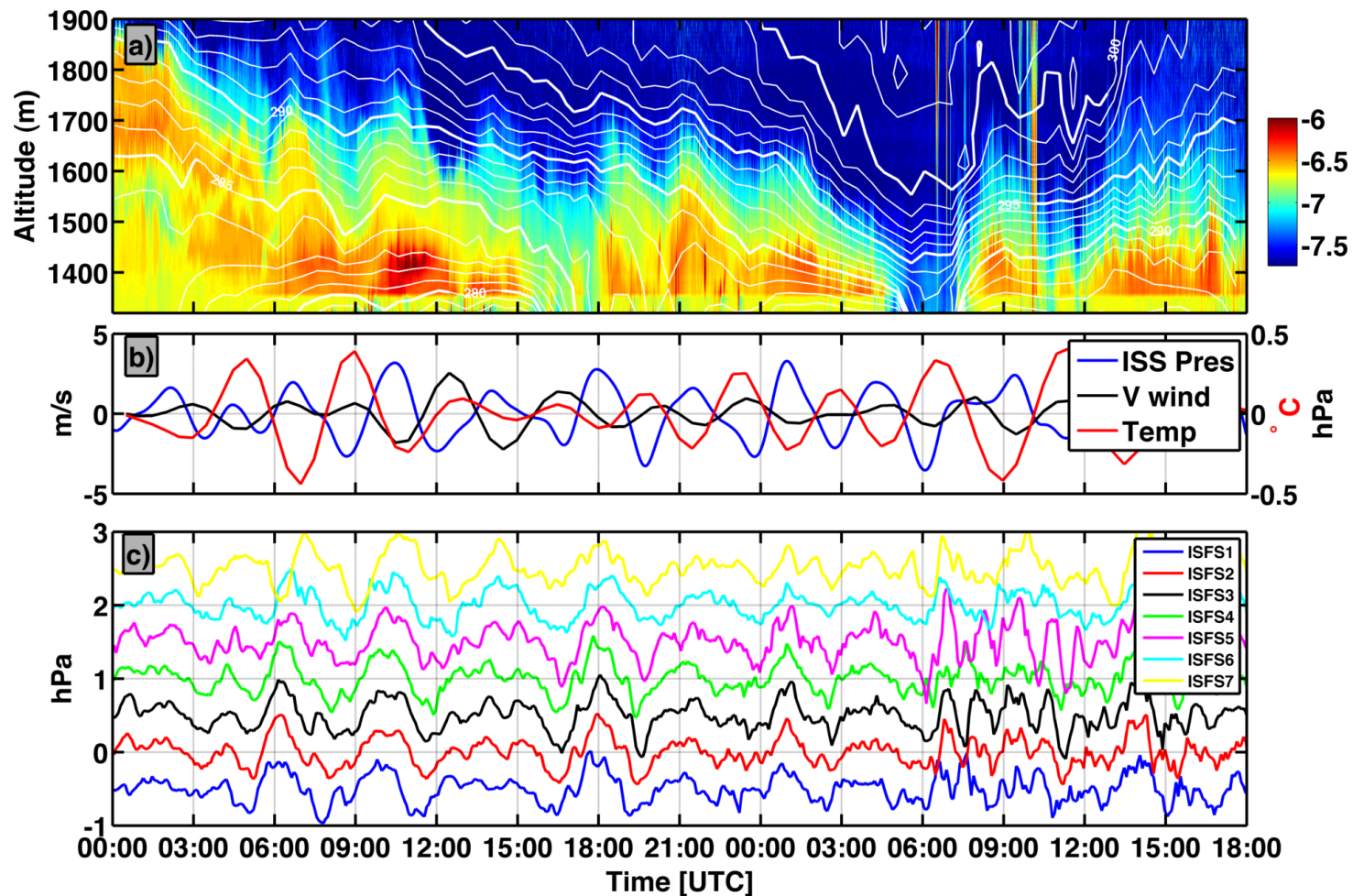
Fig. 2.13 Conditions at ISS-S from 0000 UTC 2 December to 1800 3 December of: (a) aerosol backscatter (shaded) with potential temperature (contours). (b) Band-pass filtered perturbations of ISS-S surface pressure (blue), and 1500-1800 m mean meridional wind (black), and potential temperature (red). (c) High-pass filtered surface pressure perturbations at each ISFS site. Curves are offset by 0.5 hPa.
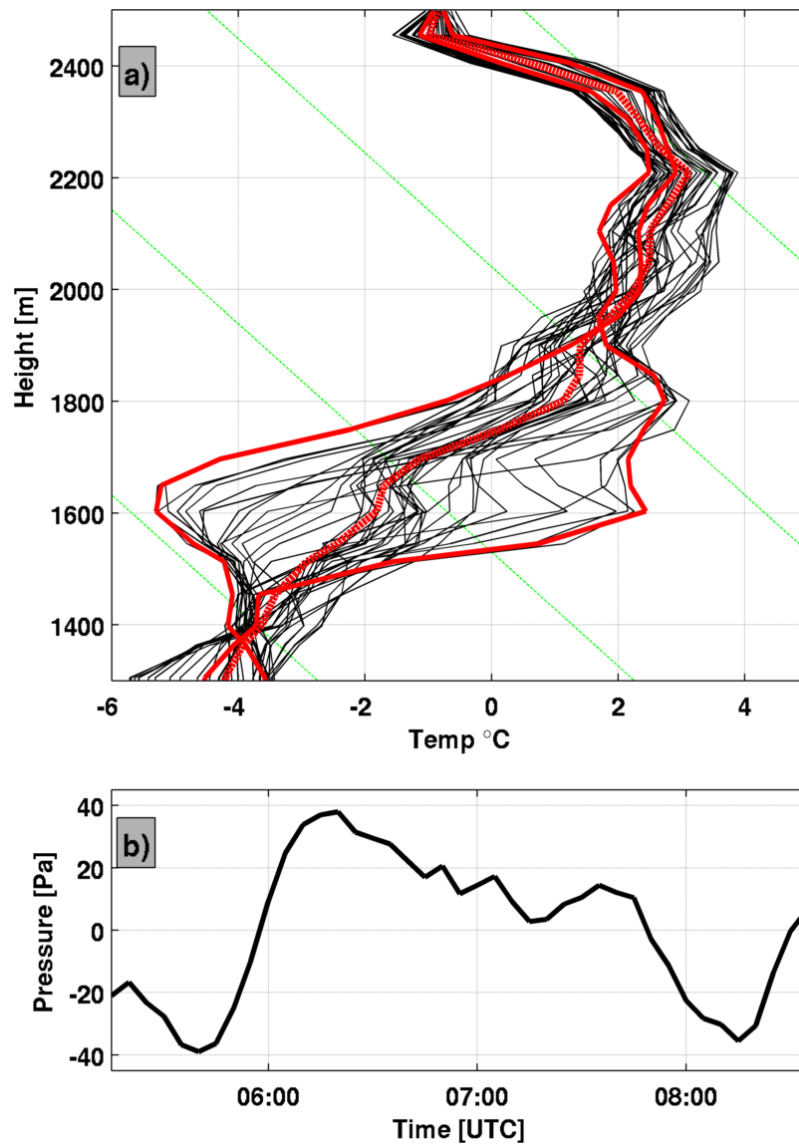
Fig. 2.14 Temperature and pressure variations associated with basin-scale oscillations. (a) Harker's Ridge temperature profiles every 5 mins between 0525 and 0830 UTC during the passage of one BSIW. Red lines indicate the mean and extreme profiles and the dashed green lines are adiabats. (b) The surface pressure perturbation computed from temperature anomalies.
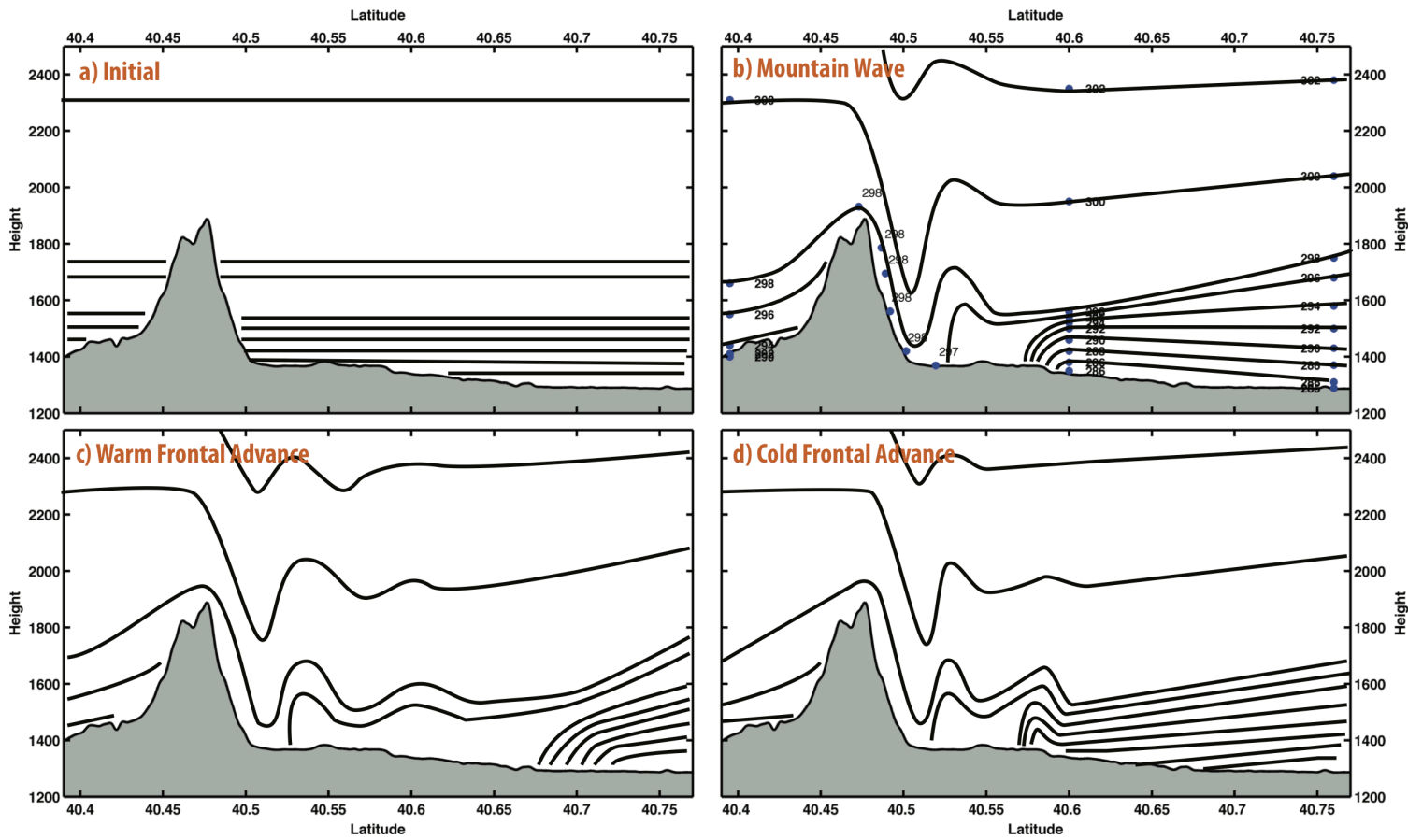
Fig. 2.15 Schematic of cold-air pool displacements. Stages described in the text.

CHAPTER 3

TURBULENT EROSION OF COLD-AIR POOLS:

NUMERICAL SIMULATIONS

3.1 Abstract

High-resolution idealized numerical simulations are used to examine the turbulent removal of cold-air pools commonly observed in mountain valleys and basins. A control simulation with winds aloft increasing from 0.5 to 20 m s^{-1} over 20 h combined with typical cold-air pool stratification illustrates the interplay over time of: lowering of the top of the cold-air pool; spillover downstream of the valley from the upper reaches of the cold-air pool; wave-like undulations affecting the cold-air pool's depth and stratification across the valley; and smaller temporal and spatial scale Kelvin-Helmholtz waves within the uppermost layers of the cold-air pool. The heat budget within the cold-air pool demonstrates the nearly compensating effects of vertical and horizontal advection combined with turbulent heating of the upper portion of the cold-air pool and cooling in the layers immediately above the cold-air pool. Sensitivities of turbulent mixing in cold-air pools to stratification and upstream terrain are examined. Although the characteristics of the turbulent mixing differ as the stratification and topography are modified, a bulk parameter (the cold-air pool Froude number) characterizes the onset and amplification of turbulent mixing as well as when the cold-air pool is removed. When this Froude number

exceeds 1, Kelvin-Helmholtz waves and turbulent heat fluxes commence. Turbulent heat flux and wave activity increase until $Fr = 2$, after which the cold-air pool breaks down and is removed from the valley. The rate of cold-air pool removal is proportional to its strength, i.e., a stronger cold-air pool is removed faster once turbulent erosion is underway.

3.2 Introduction

Multiday cold-air pools (CAPs) are increasingly leading to hazardous levels of air pollution in both urban and rural mountain valleys (Reddy et al. 1995; Pataki et al. 2005; Pataki et al. 2006; Malek et al. 2006; Schnell et al. 2009; Lareau et al 2013). Since CAPs are characterized by stable stratification and limited mixing, greater accumulation of anthropogenic and biogenic emissions result from longer-lived CAPs (Silcox et al. 2012). The resulting high concentrations of fine particulates, $PM_{2.5}$, have been linked to increased risk for cardiovascular diseases, greater numbers of emergency room visits for asthma, and decreased lifespan (Pope et al. 2009; Beard et al. 2012).

CAPs generally form during the onset of high pressure when warming aloft couples with nocturnal radiative cooling to generate a deep stable layer (Wolyn and Mckee 1989). The intensity and longevity of the CAP is modulated by variations in the surface energy budget and subsequent interactions with passing weather systems (Wolyn and Mckee 1989; Whiteman et al. 1999; Whiteman et al. 2001; Zhong et al. 2001; Reeves and Stensrud 2009; Gillies et al. 2010; Zardi and Whiteman 2013). The breakup of CAPs is most often due to vigorous cold-air advection associated with the passage of baroclinic troughs and fronts (Whiteman et al. 1999; Reeves and Stensrud 2009). However, in the

absence of strong cold-air advection, CAP removal depends on the interplay between the CAP's stratification and the strength of winds aloft penetrating into the valley or basin (Lee et al. 1989; Petkovšek 1992; Petkovšek and Vrhovec 1994; Gubser and Richner 2001; Zängl 2003; Zängl 2005; Flamant et al. 2006; Lareau and Horel 2014). The downward penetration of strong winds can lead to *displacement* of the CAP as well as *turbulent erosion* of its stratification.

CAP *displacement* occurs due to regional pressure gradients and strong winds affecting valley stratification. For example, Petkovšek and Vrhovec (1994), and later Zangl (2003), demonstrate that CAPs develop a sloping upper surface wherein the depth of cold-air deepens towards lower pressure. If the resulting CAP slope becomes sufficiently large, cold-air is advected over the confining topography and the volume of air within the CAP is reduced (Zängl 2003, 2005). This tilt may also cause the CAP to contract from one end of the valley or basin, providing localized ventilation. CAP displacement is further influenced by wind stress and ageostrophic advection, both of which may increase the CAP slope and accelerate removal (Petkovšek and Vrhovec 1994; Gubser and Richner 2001; Zängl 2003, 2005; Lareau and Horel 2014).

Terrain flow-interaction may also displace a CAP. For example, Lee et al. (1989) find from numerical simulations that an inversion layer downwind of a mountain can be displaced by a mountain wave forming in cross barrier flow. Observations further support that mountain waves occasionally remove CAPs, sometimes forming a warm front that sweeps through a valley (Whiteman et al. 2001; Flamant et al. 2002; Lareau and Horel 2014). Zangl (2005) demonstrates that such topographic influences on CAPs are sensitive to both wind direction and local topographic details.

The tendency for flow to sweep over the flanking topography and flush stratified air from a valley has been related to critical thresholds of a Froude number defined as:

$$F = \frac{U}{NH} \tag{3.1}$$

where U is the mean wind above the valley, N is the ambient Brunt-Vaisala frequency, and H is the valley depth (Bell and Thompson, 1980; Tampieri and Hunt, 1985; Soontiens et al. 2013). Using idealized tank experiments Bell and Thompson (1980) demonstrate that when $F \geq 1.2$, flow ventilates a valley regardless of the stratification. Grainger and Meroney (1993) find similar Froude number dependence for dispersion from an open-cut coalmine in stratified flow. Terrain geometry also affects the degree of valley ventilation (Tampieri and Hunt, 1985; Lee et al. 1987). However, Reinecke and Durran (2008) highlight how the specification of N in a Froude number can strongly affect the interpretation of terrain-flow interactions.

Strong winds aloft can also cause CAP removal by *turbulent erosion*, which is the downward progression of a less dense layer into a stratified layer by turbulent entrainment across the interface (Kato and Phillips 1969; Pollard et al. 1973; Strang and Fernando 2001 a, b). Laboratory tank experiments show that the entrainment is due to either dynamic instability, such as Kelvin-Helmholtz instability, or ambient turbulence in the layer aloft (Price et al. 1978). The rate of entrainment is governed by the Richardson number, which is the ratio of buoyant consumption to mechanical production of turbulent kinetic energy.

A key aspect of turbulent erosion is the increase in interfacial buoyancy gradient as the mixed layer aloft expands downward into the colder or denser layer (Pollard et al. 1973; Petkovsek 1992). In order for such erosion to continue, the mechanical production

of turbulence must also increase so as to offset the increased buoyant consumption. The semi-analytic model applied by Petkovsek (1992) demonstrates that winds aloft must continually accelerate to produce progressive top-down turbulent erosion of CAPs. Numerical simulations by Vrhovec and Hrabar (1996) and Rakovec et al. (2002) help to confirm the accelerating wind criterion for CAP erosion, although their simulations lack sufficient resolution to explicitly resolve turbulent mixing.

Zhong et al. (2001) also rely on a semi-analytic model to study CAP turbulent erosion due to shear instability across the CAP top. Turbulent erosion commences in their model when the bulk Richardson number for the uppermost layer of the CAP becomes sub-critical, which can be expressed in terms of a threshold wind speed

$$u \geq Nd \tag{3.2}$$

where N and d are representative scales for the static stability and the depth of the capping inversion layer, respectively. Their results indicate that for a given stratification and constant wind, the erosion rate decays with time such that turbulent erosion is unlikely by itself to dissipate a CAP.

The turbulent break down of stratification has also been studied for nocturnal stable boundary layers beneath low-level jets. Banta et al. (2003) formulate a jet bulk Richardson number:

$$Ri_b = \frac{g}{\theta} \frac{\Delta\theta/\Delta z}{(U_x/Z_x)^2} \tag{3.3}$$

where U_x and Z_x are the speed and height of the low-level jet and the numerator represents the temperature deficit over the depth of the stable layer. Their observations indicate that the magnitude of turbulence within the stable layer is controlled by this bulk parameter, rather than local gradients (Banta et al 2003; Banta et al. 2007; Sun et al.

2012). When Ri_b is less than 0.3, turbulent fluxes of heat and momentum are significantly increased. It is worth noting that the bulk Richardson number is closely related to the aforementioned Froude number. Provided that linear profiles of shear and stability are assumed, as by Banta et al. (2003), the two dimensionless numbers are related by:

$$Ri_b = 1/F^2 \tag{3.4}$$

where H and Z_x are assumed to be equivalent. This relationship points to a broader linkage between studies of turbulent mixing and valley flushing.

Despite previous research, aspects of CAP removal by strong winds aloft remain incompletely understood (Zardi and Whiteman 2013). For example, observations of wind-CAP interaction during the Persistent Cold-Air Pool Study in Utah's Salt Lake Valley (PCAPS; Lareau et al. 2013) reveal that CAP removal is sensitive to the strength and structure of stratification. Figure 3.1 demonstrates an aspect of this sensitivity by contrasting conditions during two Intensive Observing Periods (IOPs), each affected by accelerating flow aloft. The IOP-1 CAP (Fig. 3.1a,b) thins substantially from ~700m to ~200m over 18 hs, and is subsequently flushed from portions of the valley a short time later (Lareau and Horel, submitted). The IOP-9 CAP (Fig. 3.1 c,d) also thins from the top down, but the reduction is less that in IOP-1 and surface conditions remain decoupled despite comparable flow aloft. A key difference between the profiles is the *structure* of the CAP: IOP-1 is linearly stratified, whereas IOP-9 exhibits a sharp capping inversion layer above a partially mixed surface-based layer.

While these PCAPS observations highlight the importance of top down removal of CAPs, the experimental design was not directed towards measurements of turbulent heat and momentum fluxes at the CAP top. As such it is difficult to diagnose the underlying

differences in the rate of CAP removal as a function of stratification. Hence, in this study we use idealized high-resolution simulations to examine the turbulent and advective processes contributing to CAP breakup. The extent to which the broad parameter space of wind speeds aloft, stability profiles, and topographic details can be summarized succinctly is explored through a series of sensitivity experiments. The setup and details of these simulations are described in Section 3.2. Results are then presented in Section 3.3, including how a "CAP Froude number" can be used to better understand CAP removal. A quick comparison and discussion of the model simulations relative to conditions during PCAPS IOP-1 follows in Section 3.4. Finally, Section 3.5 summarizes our findings.

3.3 Experimental Setup

3.3.1 Numerical Model

The simulations in this study are executed using version 3.4 of the Weather Research and Forecasting (WRF) model (Skamarock et al. 2008). The model is configured as an idealized Large Eddy Simulation (LES) so as to explicitly resolve the turbulent mixing of heat and momentum between CAPs and their ambient environment. In contrast, most previous numerical investigations of CAP breakup, e.g., Rakovec et al. (2002), rely on parameterization of these turbulent motions. For guidance in selecting sufficient grid spacing, we follow Skamarock (2005), who shows that for WRF to reproduce benchmark simulations of a gravity current (Straka et al.1993) the horizontal grid spacing should be less than or equal to 100 m that high order finite differencing is required. Since the buoyancy and velocity scales of our CAP cases are similar to those of the gravity current, we choose $\Delta x = \Delta y = 50$ m and use 5th order upwind horizontal advection. The vertical

grid is stretched over 100 levels from the surface to 10 km such that the resolution within the first 500 m ranges from 14 m to 30 m. To accommodate the high resolution grid the model time step is 0.5 seconds.

The domain is a rectangular slab that is 102 km long (stream wise) by 1 km wide. The stream wise boundaries use a 5-km lateral Rayleigh damping layer that adjusts the model towards prescribed inflow at each time step. The upper boundary also uses a Rayleigh damping to prevent spurious wave reflection. The span-wise boundaries are periodic.

Since we are interested only in the dynamics of wind-induced CAP removal, we turn off surface heat flux, radiation, and microphysics parameterizations. Surface momentum fluxes are, however, parameterized using a Monin-Obukov surface layer. On the scale of our experiments the Rossby number is sufficiently large so as to neglect rotation.

3.3.2 Control Experiment

The basic dynamics of wind-induced CAP removal are examined using a linearly stratified ($N=0.027$ s^{-1}) CAP confined between two 500-m mountain ridges (Fig. 3.2a, c) while the environment external to the CAP is more weakly stratified ($N=0.01$ s^{-1}). The cold air fills the valley such that the temperature difference across the CAP is 10 K, which is comparable to CAPs observed during PCAPS (see Fig. 3.1). The topography is also loosely based on a south-to-north transect of the Salt Lake Valley: ridge crests are separated by 42-km and the valley floor is ~20 km across. The maximum valley slope angle is ~12 degrees while the outer mountain slopes are more gradual with a maximum of ~5 degrees. Radom noise with a mean of 2.5 m and a maximum of 5 m is added to the topography to help generate 3-D turbulence.

To test CAP response to accelerating wind, the inflow is linearly increased from 0.5 m s^{-1} to 25 m s^{-1} over the 20-h simulation (3.4 x 10^{-4} m s^{-2}). Similar accelerations were documented during PCAPS IOP-1. We impose a 100-m deep logarithmic boundary-layer shear profile at the inflow boundary, but the flow then adjusts to a self-consistent shape and depth before interacting with the CAP.

3.3.3 Sensitivity Experiments

The sensitivity of CAP removal to the strength of stratification and the total amount of cold air that must be scoured from the valley is tested using four initial CAP profiles: Linear (control), Capping Layer, Multilayered, and Shallow Layer (Fig. 3.2c). Each profile is constructed with the same surface temperature deficit (10 K), but varies either in maximum stability or column-integrated negative buoyancy:

$$BH = -g \int_0^H \left(\frac{\theta(z) - \theta(H)}{\theta(H)} \right) dz \qquad (3.5)$$

where $H = 500$ m is the depth of the valley and $\theta(H)$ is the potential temperature at the valley top (initially 274 K), such that the CAP's initial negative buoyancy is relative to a dry adiabatic profile. The negative sign is used for convenience. BH is sensitive to both the depth and the strength of the stratification and is similar to the column heat deficit presented by Whiteman et al. (1999). A summary of the properties for each CAP profile is provided in Table 3.1.

The destruction of each CAP by accelerating wind is subsequently simulated using two different terrain configurations: (1) "mountain" and (2) "plain" (Fig. 3.2a,b). The mountain terrain is the control topography, whereas the plain configuration replaces the outer mountain slopes with constant height surfaces extending to the model boundaries.

The valley shape is unaltered between cases; thereby testing how upstream flow-topography interaction affects the time scale and spatial structure of CAP removal. For example, the two terrains differ in terms of their basic mountain wave response to the linearly stratified inflowing air stream. The mountain cases tend to produce more flow into the valley along the upwind valley slopes, whereas the plain cases exhibit greater flow separation.

3.3.4 CAP Froude number

An advantage of defining the CAP strength in terms of the layer-integrated buoyancy, BH, is that it is possible to reduce a portion of the parameter space of our experiments by defining a CAP Froude number:

$$Fr = \frac{U}{\sqrt{BH}} \tag{3.6}$$

where U is the maximum wind speed above the CAP and the denominator replaces a common approximation for NH (Granger and Meroney 1993; Reinecke and Durran 2008):

$$NH \cong \sqrt{\frac{g}{\bar{\theta}} \frac{\theta_{top} - \theta_{bot}}{H}} * H \tag{3.7}$$

The CAP Froude number better differentiates between cases with variations in stratification within CAPs as examined in this study, i.e., there are no differences in NH using the conventional approximation between any of the four CAP profiles shown in Fig. 3.2. Moreover, as the CAP profile approaches that of a two-layer stratified system (e.g., knife-edge capping inversion), $\sqrt{BH}$ approaches the conventional shallow water gravity speed, $\sqrt{g'h}$. Rather than the common, and difficult, requirement for other

terrain-flow interactions to specify the upstream wind speed impinging on the upstream terrain, *Fr* is defined here in terms of the maximum wind *above* the CAP. Hence, it is possible from a profile within the valley to define *Fr* relevant for CAP removal.

3.4 Results

3.4.1 Control Case: Linear CAP, Mountain Topography

This section highlights the key dynamics of wind-induced CAP breakup by examining the control simulation. Figure 3.3 shows 20-min mean cross sections of the CAP at successive inflow wind speeds of 5, 10, and 15 m s^{-1} corresponding to 221, 466, and 711 mins into the simulation, respectively.

Figure 3.3a shows that the initial horizontally homogenous CAP responds to the acceleration of the inflow to 5 m s^{-1} by tilting in the downwind direction such that the CAP depth is decreased (increased) at the windward (downwind) end of the valley. The difference in CAP depth across the valley is ~200 m. At the downwind edge of the valley, blocked flow below is separated from a thin slice of the upper layer of the CAP (e.g., the top three isentropes) that possesses sufficient momentum to surmount the downstream ridge, thus removing cold-air from the valley via "spill over" (Zangl 2003). Vertical wind shear is concentrated in a shallow layer near the CAP top, since the upper layer of the CAP is flowing downstream while the remainder of the CAP is nearly stagnant. At the windward end of the basin, two low amplitude lee waves generated by the upstream mountain ridge locally affect the stability the top of the CAP.

As the flow continues to accelerate to a speed of 10 m s^{-1} over the next several hs (Fig. 3.3b), the CAP has thinned to a mean depth of ~300 m and continues to exhibit a

downstream incline and spillover. Compared to its initial state, the stability at the CAP top has increased (e.g., tighter vertical gradient in potential temperature). The CAP also exhibits a series of wave-like undulations wherein the local CAP depth and stratification vary along the valley. The first two undulations are associated with lee waves from the upstream mountain, while the remaining wave-like variations are less clearly linked with the upstream terrain. The flow within the CAP remains weak with some regions of reversed flow (blue shading), implying a dynamical response arising from the blocked flow further downstream.

After 12 h and acceleration of the inflow to 15 m s^{-1} (Fig. 3.3c), the CAP is removed from the windward third of the valley and thinned to a mean depth of ~150 m along the remaining downwind fetch. The downwind incline persists, though spillover is less due to the increased separation between the CAP top and the ridge crest. A front separates the stagnant cold air from the warmer, windier air sweeping into the basin. This front advances through the valley leading to a step-like jump in surface temperature of ~10 K as it passes (not shown). The previously identified undulations in the CAP depth persist with the windward side of each undulation exhibiting both stronger stratification and stronger shear as compared to its downwind side.

To further summarize the CAP removal, the column-integrated buoyancy, BH, is shown in Fig. 3.3d as a function of time and along valley distance. Commensurate with the CAP thinning throughout the simulation, BH progressively diminishes with time and increasing wind speed. The CAP tilting is apparent as greater BH for the downwind portion of the basin at a given time and subsequently reflected in the pattern of CAP removal (e.g., BH approaches zero), which occurs first at the upwind end of the valley at

around 12 h, then progresses downwind before final CAP eradication at ~15 h when the inflow is ~19 m s^{-1}. The front separating CAP air from warmer flow propagates at a rate of ~2.8 m s^{-1}, though its motion is somewhat discontinuous due to meso-γ variations in the CAP depth.

In addition to the CAP thinning and tilting, waves at multiple scales and phase speeds are affecting the CAP (Fig. 3.3d). For example the lee-waves apparent in Fig 3.3a-c have a pronounced signature that slowly moves downstream due to the increasing inflow velocity. Many smaller scale waves are also apparent as striations tending to originate proximal to the lee-wave and progressing downstream at a rate roughly that of the ambient flow. The meso-γ CAP undulations are also evident as variations in BH that propagate downstream at a rate greater than that of the lee wave but much slower than the smaller scale waves.

A snapshot of these smaller scale waves and their contribution to CAP destruction is presented in Fig 3.4. At 500 mins, the top of the CAP is populated with numerous perturbations, many exhibiting the characteristic billow of Kelvin-Helmholtz waves (KHW). These KHW have amplitudes of 100-200 m and wavelengths of 0.5 to 1 km (inset, Fig. 3.4). KHW form in stratified shear flow when the magnitude of the shear exceeds the damping effects of the stratification (Nappo 2002), a condition given by the critical gradient Richardson number

$$Ri_g = \frac{N^2}{\left(\left(\frac{\partial u}{\partial z}\right)^2 + \left(\frac{\partial v}{\partial z}\right)^2\right)} \leq 0.25 \tag{3.8}$$

where the terms in the denominator are the components of the vertical shear. It is apparent from Fig. 3.4b, that the simulated KHW form in regions of subcritical Ri_g (blue

shading) *within* the uppermost layers of the CAP. For example, small wavelike perturbations first appear starting at ~37 km in a narrow filament at the CAP top where subcritical Ri_g coincides with strong static stability, reflecting dynamically unstable stratified shear flow. This dynamically unstable layer is distinct from the more extensive layer of subcritical Ri_g associated with the turbulent boundary layer that is advected into the basin. These nascent KHW subsequently grow downstream, becoming breaking waves before diminishing into a region of reduced stratification and shear at ~47 km. The meso-γ undulations previously described in the 20 min averages (Fig. 3.3b,c) simply reflect the impact of averaging the shear and stratification associated with the KHW.

The kinematic turbulent heat flux due to these KHW is assessed using 15-min Reynolds averages (Fig. 3.4c). Since the KHW transport cold air upwards and warm air downwards, localized regions of strong negative heat flux (-100-150 W m^2) are evident in Fig. 3.4c. The resulting turbulent heating *rate* (i.e., the flux divergence) manifests as a vertical couplet of cooling above and warming within the CAP (Fig. 3.4d). This process contributes to the generation of an intermediary layer of air above the primary CAP that is cooler than the air aloft and warmer than the air inside the CAP.

The relationships between shear, stratification, and KHW are illustrated in Fig. 3.5 by examining the valley mean atmospheric column as a function of time and height. The top of the CAP progressively lowers and also becomes increasingly stable. The peak stability just before the CAP is destroyed is N~0.055 s^{-1}, more than twice that at the initial time. The strong winds extending downward into the basin maintain strong shear at the CAP top (Fig. 3.5a). The strength of the shear and that of the stratification vary roughly in concert thereby maintaining a region of near critical gradient Richardson

number along the CAP top that continually supports KHW (Fig. 3.5b). The KHW accomplish this mutual adjustment by redistributing heat and momentum.

The KHW, however, cannot alone remove the CAP. Advection also contributes to the transport of cold air out of the valley. This interplay between advection and KHW is examined in terms of the heat budget computed locally at every location and then averaged to obtain a valley-mean column:

$$\underbrace{\frac{d\bar{\theta}}{dt}}_{1} = \underbrace{-(u \cdot \nabla\bar{\theta} + w \cdot \nabla\bar{\theta})}_{2} - \underbrace{\left(\frac{\partial \overline{w'\theta'}}{\partial z} + \frac{\partial \overline{u'\theta'}}{\partial x}\right)}_{3} \tag{3.9}$$

where term 1 is the local time rate of change of the 15 min Reynold's mean potential temperature that is forced by the terms on the right-hand-side: the heating or cooling due to mean advection (term 2) and turbulent heat flux divergence (term 3). There is no radiative heating term since radiation is ignored. Each term of the heat budget is shown in Fig. 3.6 along with the contours of mean potential temperature.

Averaged over the entire valley, substantive turbulent heating commences after ~5 hs (Fig. 3.6a), corresponding to the onset of KHW during the transition to subcritical gradient Richardson number at the top edge of the CAP (Fig. 3.5b). The heating rate is then, in general, positive within the top edge of the CAP and negative above, as previously shown in the snapshot in Fig. 3.4. The regions of positive heating closely align with the increased static stability in the capping layer. This pattern is consistent with theories for top down turbulent erosion, which predict that the lowering of the mixed layer generates a localized increase in the buoyancy contrast between layers (Pollard et al. 1973; Price et al. 1978; Petkovsek 1992). The turbulent heating rate is predominately negative above the CAP, indicating that the breaking waves redistribute the colder,

denser air into the mixed layer aloft, which tends to raise the potential energy of the system.

In contrast to the vertical dipole in the turbulent heating rate, the net advective heating rate (term 2) is generally positive at and above the CAP top, with only ephemeral periods of cooling (Fig. 3.6b). Importantly, advection warms the mixed layer aloft, the same region that KHW continuously cool with an almost one-to-one relationship between periods of advective warming and turbulent cooling. Hence, the mixed layer temperature remains roughly constant throughout the simulation.

Advective heating of the valley atmosphere is also important prior to the onset of KHW since the only way to lower the CAP during the first 5 hs of the simulation is the laminar spillover of the cold-air out of the valley. Thus, there appear to be two regimes in the CAP removal: the first is dominated by spillover while the second corresponds to a combination of KHW and advection. In the net, the two processes act together to destroy the CAP from the top down, which is shown in Fig. 3.6c in terms of the mean potential temperature tendency (term 1).

The top down destruction of the CAP for the control case can be summarized as follows:

- Winds increase aloft transferring momentum into the upper layers of the stratified air mass. The upper most layers of the CAP are then advected downstream and over the topography, reducing the CAP by spillover.

- As the winds aloft continue to increase, a critical threshold is reached within the sheared upper layers of the CAP that leads to the breakdown of stratification into KHW. These KHW mix cold-air upwards and warm air downward, resulting in an

"intermediary layer" of air that is potentially warmer than the CAP, but cooler than the flow aloft.

- The "intermediary layer" is subsequently scoured from the CAP top, advected downwind and eventually out of the basin. The warmer inflowing air replaces the intermediary layer, thus progressively lowering and sharpening the CAP.

3.4.2 Sensitivity Results

3.4.2.1 Overview

In this section we investigate how the timescale and structure of CAP removal varies with stratification and terrain. Many of the basic features of these sensitivities are revealed in 20-min mean cross sections of each simulation when the inflow speed reaches 15 m s^{-1} (after ~12 h, Fig. 3.7). It is immediately apparent that the CAPs in mountain cases are removed more effectively than those in the plain cases. Each mountain CAP is inclined in the downstream direction and displaced (or eradicated entirely) by the warmer inflowing air at the windward end of the valley. For the plain cases, the valley atmosphere remains largely decoupled from the flow aloft with only minor reductions in CAP strength. The plain cases also exhibit organized reversed flow and a modest upstream incline such that the greatest CAP depth is found near the windward end of the valley. As a result the spillover in the plain cases is comparatively less than in the mountain runs.

Comparing the simulations with differing stability profiles, the shallow CAPs are most affected by the accelerating flow, and in the case of the mountain terrain, completely removed. The capping layer cases are least affected, with, for example, the

plain case nearly unaltered after 12 h. In that case, the CAP serves as an impermeable barrier and the flow aloft proceeds across the valley as if the valley were not present. The multilayered and linear CAPs, which start from the same value of BH, are more similarly eroded.

These basic inferences regarding the sensitivity of CAP removal to the terrain and stability profiles are confirmed by examining the time-distance evolution of BH for each case (Fig. 3.8). As expected, the terrain sensitivity is large: the mountain CAPs are removed after 11-15 hrs compared to 14 to more than 20 hrs for the plain cases. In addition, whereas the plain cases maintain a steady state CAP until much later into those simulations, the reduction of BH in the mountain cases commences shortly after initialization. The terrain also affects the spatial pattern of CAP removal. As seen in Fig. 3.7, the mountain cases experience a pronounced downwind incline, which leads to the CAP removal advancing downwind through the valley (Figs. 3.8a-d). In contrast, the plain cases maintain a vestigial pocket of cold-air near the windward end of the valley and do not exhibit a clear downwind frontal propagation during removal (Figs. 3.8e-h). This key morphologic difference is associated with separation eddies that form in the plain cases as the flow detaches from the inflow plain at the valley crest, thus sheltering the windward end of the valley. The mountain simulations, on the other hand, experience plunging flow in the same region due to higher amplitude mountain waves, which help to displace the CAP.

Terrain-flow interactions are also a key component of the difference in CAP removal timescale (Fig. 3.9). For the mountain cases, the flow above the CAP tracks closely with the prescribed inflow velocity, whereas for the plain cases it is systematically reduced.

This difference is related to the conservation of mass through the model domain. For the plain cases, the total depth of the flow increases to fill the valley as the CAP is removed, requiring the column mean velocity to diminish. Thus, the differences between the valley and plain cases arise not simply due to terrain geometry but to the impact of the terrain on the strength of the flow aloft impinging on the CAP.

As shown in Fig. 3.10, the sensitivity to initial stratification is also pronounced, accounting for multihour differences in the timing of CAP removal. First, the greater the initial value of BH, the longer it takes to remove the CAP. For example, the shallow cases are removed much sooner than the capping layer cases regardless of the terrain. Moreover, the multilayer and linear CAP profiles, which have the same initial value of BH but differ in their peak stability within the CAP, are removed in comparable times. This result suggests that the total amount of cold air in the basin is more important than the maximum stability within the CAP. In addition, Fig. 3.10 clearly shows that the greater the initial value of BH, the greater the eventual *rate* of cold-air removal from the basin. For example, the capping, linear, multilayer, and shallow stability profiles lead to successively slower rates of cold-air removal. This effect tends to converge the times required to remove weaker and stronger CAPs.

As in the control simulation, the CAP reduction in all cases proceeds as a continual top down turbulent erosion, wherein the lowering of the CAP top produces a very sharp, shallow layer of cold air just before removal (not shown). There are, however, distinct differences in the time evolution of the maximum stability among the stability profiles (Fig. 3.11). Compared to the initial stratification, the maximum stratification in the linear profiles continuously increases, approaching a value nearly twice that at initialization (red

markers, Fig. 3.11). In contrast, the multilayer CAPs experience a gradual decrease in stratification as the upper inversion layer is removed and the internal adiabatic layer is mixed into the flow aloft (blue markers, Fig. 3.11). The stratification then increases as the CAP top reaches the lower inversion layer. The capping and shallow profiles, which both start with comparable layers of strong stability, experience little change in strength for most of the run then spike to higher values as the CAP top approaches the ground. In terms of the actual values of peak stability, each case approaches a value of N~0.055 s^{-1} just prior to removal (not shown). This is roughly equivalent to a 10 K inversion over 100 m, which is consistent with the tendency for the surface condition to remain unchanged until the final destruction of the CAP.

3.4.2.2 CAP Froude Number, *Fr*

In light of the pronounced wind speed and buoyancy differences between simulations, it is useful to recast the basic sensitivity results in terms of *Fr*, in order to succinctly delineate many of the key aspects of CAP break-up. Figure 3.12 shows the time-distance evolution of each CAP in terms of *Fr*. Compared to Fig. 3.8, it is now clear that each case progresses through the same parameter space en route to breakup. Irrespective of initial stratification or terrain, *Fr* first smoothly increases from 0 to 1 as the wind aloft accelerates. Then, at *Fr*~1, the CAPs develop small waves, apparent as fine scale variations in Fig. 3.12. Wave activity then amplifies with increasing Froude number. After *Fr*~2 the CAP is rapidly eroded, with complete removal corresponding to *Fr*~3. Beyond this point the Froude number quickly becomes large as the buoyancy deficit (denominator) trends toward zero.

The dynamical significance of these Froude number transitions is highlighted by examination of the linear–plain CAP (Fig. 3.13). The changes to the valley mean potential temperature profile proceed similarly to the control case (Figs. 3.5, 3.6), but can now be interpreted using Fr. The CAP top gradually lowers for the first 8 hs of the simulation, corresponding to Fr increasing from 0 to 1 due to the increased flow aloft. The gradual thinning of the CAP during that time is entirely due to spillover and no KHW are present. Then, at $Fr\sim1$ the lowering rate increases and negative interfacial heat fluxes associated with KHW begin. The onset of the waves reduces the CAP more rapidly than the spillover alone, reflected as an accelerating increase in Fr. At $Fr\sim2$ the column heat fluxes reach their maximum amplitude (Fig. 3.13c) and the CAP top lowers even more sharply (Fig. 3.13a). By $Fr=3$ the CAP is reduced to just a few 10s of meters, and it is completely eradicated by $Fr=4$. Fig. 3.13 suggests that Fr not only reduces the parameter space by combining the effects of changes in wind shear and stability over time, but also is closely related to the onset and amplification of turbulent mixing.

The relationship between turbulent heat flux and the Froude number is borne out across the remaining sensitivity cases (Fig. 3.14a). The wave induced interfacial fluxes generally start at $Fr\sim1$, excepting the shallow-plain simulation (green squares), which we discuss later. The flux amplitude continuously increases to a maximum proximal to $Fr=2$, remains high for Fr between 2 and 3, then reduces toward zero for $Fr>3$, corresponding to the complete removal of the stratification.

Not surprisingly, Fr is also related to the gradient Richardson number evaluated at the CAP top (Fig. 3.14b). The $Fr=1$ transition corresponds to Ri_g approaching its critical value; consistent with the onset of KHW and turbulent heat flux. What is more surprising

is that Ri_g is then roughly constant with increasing Fr despite a concurrent increase in magnitude of the heat fluxes, reflective of the mutual adjustment between shear and stratification demonstrated for the control case (Fig. 3.5). The value of Ri_g finally diminishes once the CAP is removed ($Fr>3$) and trends towards the critical Richardson number ($\log10[Ri_c] = -0.6$).

Despite nearly constant values of Ri_g over the span of $Fr=1$-3, the vertical scales of the KHW vary, which is shown for each of three cases in Fig. 3.15. At $Fr=1.2$, the waves are diminutive and confined to the top edge of the CAP, whereas at $Fr=2.2$ pronounced billows pervade the greater CAP depth. Thus, the minimum in heat flux at $Fr\sim2$ is associated with the transition to layer-deep KHW. It is worth reemphasizing that $Fr=2$ closely corresponds with $Ri_b=0.25$ for the CAP layer, indicative of a bulk breakdown of the stratification and a transition to a more turbulent regime irrespective of *locally* evaluated gradients (Banta el al. 2003; Banta et al. 2007). That the CAP is not immediately destroyed at this threshold reflects the horizontal inhomogeneity within the valley. Internal circulations redistribute the cold-air and offset the locally vigorous mixing. Thus, fluxes remain large beyond $Fr=2$ until the source of cold-air is entirely exhausted.

A related aspect of these results is that the magnitudes of the turbulent heat fluxes are also proportional to the strength of the underlying CAP (not shown). The capping layer cases experience the strongest heat fluxes, whereas the shallow cases are more subdued in their turbulent mixing. This result helps to explain the results presented in Figs. 3.9 and 3.10, which show that the strong CAPs were destroyed more rapidly than weaker CAPs. In total, this effect tends to converge the timescales for CAP removal across the range of

stability profiles and makes the time to "mix-out" more similar than might otherwise be expected.

Finally, we note that the shallow CAP cases have one distinct difference from deeper ones, particularly evident in the shallow-plain case early in its simulation when the relationship between Fr and the onset of turbulent fluxes does not hold (green squares, Fig. 3.14a). Turbulent heating in that case begins at much smaller values of Fr due to strong eddies forming as the inflowing air stream separates from the leading edge of the valley (not shown). The resulting turbulence impinges on the CAP top, thereby inducing turbulent heat fluxes long before the mean flow above the CAP reaches a threshold to induce dynamic instability. Later, when KHW begin to form, the erosion progresses more similarly to the other cases. Hence, nonlocal turbulence also plays a role in the breakup of the shallow cases.

3.5 Comparison with Observations

The results of our control simulation compare favorably with observations of wind-induced CAP removal during PCAPS IOP-1 (Fig. 3.16). The potential temperature and wind data for IOP-1 are derived from numerous balloon soundings collocated with a Radio Acoustic Sounding System and Radar Wind Profiler in the center of the Salt Lake Valley. Further details are available in Lareau et al. (2013) and Lareau and Horel (2014). Despite the differences between our idealized simulations and PCAPS observations, both reveal CAPs thinning from initial depths of ~500-m down to the surface in ~15 hs due to interaction with accelerating wind aloft. Also, as the IOP-1 CAP thins from the top down, the static stability is increased, which is a key aspect of the control simulation. Even more

striking is the similarity at the surface, where both observation and simulation show step-like jumps in temperature as the CAP is eroded to the ground. This signature is characteristic of mechanically removed CAPs, and similar temperature traces were recorded throughout the valley during IOP-1.

It is also encouraging that *Fr* represents the observed CAP evolution. For both the observations during IOP-1 and the control simulation, *Fr* varies slowly up until *Fr*=2, and more rapidly as the stratification is reduced and warm air is mixed to the surface. There is a distinct increase in the reduction of the CAP during IOP-1 coincident with the *Fr*=2 transition as seen earlier in Fig. 3.13.

The relationship between *Fr* and wave dynamics as determined from our simulations is also consistent with the observations. For example, aerosol backscatter from a vertically pointing laser ceilometer (Fig. 3.17) reveals that small waves propagate along the upper edge of the CAP at *Fr~1*, whereas those waves grow, becoming overturning billows that impact the depth of the aerosol layer by *Fr=2*. The observed KHW when *Fr=2*, have a period of ~3 mins, amplitude of 100-200 m and estimated wavelengths of ~1 km, similar to the simulated KHW (see Fig. 3.4). Moreover, the turbulent heat flux magnitudes during IOP-1 were recorded as the edge of the CAP passed over a 50-m tower equipped with a sonic anemometer. The maximum flux magnitudes were ~100-150 W m^{-2}, closely matching the simulated values (not shown).

Beyond IOP-1, the Froude number also shows some promise for distinguishing between steady-state CAPs and those that experience appreciable or rapid erosion. For example, the CAP during IOP-9 (see a representative sounding for it in Fig. 3.1) was not eroded to the surface despite strong wind aloft. The Froude number for that sounding is

~1, and never exceeded that value despite a number of hs with strong winds. Only minor wave-induced perturbations and temporary thinning was observed. Had the winds aloft increased further, it is likely that the CAP would have been more substantively affected.

3.6 Summary and Conclusions

In this study we have presented results using idealized numerical simulations to examine wind-induced CAP breakup. Two regimes for CAP removal are identified: (1) laminar spillover and (2) the interplay of turbulent mixing and warm air advection. The spillover regime affects the CAP prior to the onset of dynamic instabilities and is due to the downward flux of momentum into the CAP. Provided sufficient momentum, the upper layers of the CAP are advected over the confining topography and out of the valley, thus reducing the CAP over time. The degree of spillover is sensitive to the specific terrain configuration and can be expected to vary greatly depending on local terrain features.

The second removal regime arises from turbulent entrainment of cold-air into the flow aloft. As the flow continues to accelerate aloft, the vertical shear and stability mutually adjust along the top of the CAP to maintain a region of dynamic instability that leads to breaking KHW. The turbulent mixing within the waves proceeds as a two-step process: first, the KHW mix cold-air vertically, then warmer inflow air replaces the partially mixed air above the CAP, which results in continual lowering of the CAP top over time. The removal of the cold-air at the surface tends to occur as a sudden burst of warm air.

The onset and amplification of KHW and their attendant fluxes is controlled by the

CAP Froude number, *Fr*, which is a bulk measure of the CAP strength relative to the flow aloft. When *Fr* exceeds unity, KHW begin. KHW subsequently increase in scale up to *Fr~2*, at which point breaking waves pervade the entire CAP depth leading to stronger heat flux and more rapid CAP breakdown. That *Fr* distinguishes between erosive and steady state conditions is potentially useful. For a given CAP profile, forecasters can estimate the wind speed required for *Fr* to exceed 1, and thus for turbulent erosion to commence. If the winds are expected to reach strengths that would lead to *Fr=2*, mix-out should be expected to follow. However, more work is required to better understand the interplay of spillover and turbulence. Thus, some caution is necessitated in the application of our results without a robust understanding of local and regional climatological CAP response to wind. Forecasters must also consider other competing processes, such as radiative cooling or strong warm air advection, which might act to maintain stratification despite turbulence.

Our model results suggest that mechanical removal of CAPs by wind is a viable mechanism to ventilate a valley on timescales of less than a day, in some instances less than 12 hs This contrasts with the previous results of Zhong et al. (2001), who indicate that CAP removal by turbulent erosion is too slow to alone remove a stratified air mass from a basin. One key difference in our findings is the link between CAP strength and the rate of removal, which converges the time scale for ventilation across a range of CAP strengths. Also, the bulk break down of the stratified layer was not considered in previous semi-analytic models. While our results are broadly consistent with observed CAP removal in limited cases, in order to more thoroughly test our findings additional observational studies are required. Such studies would need to more fully resolve

turbulent fluxes of heat and momentum due to shear instability at the top of the CAP as

well as quantify the degree of spillover from a basin.

3.7 References

Banta, R. M., Y. L. Pichugina, R. K. Newsom, 2003: Relationship between low-level jet properties and turbulence kinetic energy in the nocturnal stable boundary layer. *J. Atmos. Sci.*, **60**, 2549–2555.

Banta, R. M., Y. L. Pichugina, W. A. Brewer, 2006: turbulent velocity-variance profiles in the stable boundary layer generated by a nocturnal low-level jet. *J. Atmos. Sci.*, **63**, 2700–2719.

Beard, J. D., C. Beck, R. Graham, S. Packham, M. Traphagan, R. Giles, and J. G. Morgan, 2012: Winter temperature inversions and emergency department visits for Asthma in Salt Lake County, Utah, 2003-2008. *Env. Health Pers*., **120,** 1385-1390.

Bell, R. C., and R. Thompson, 1980: Valley ventilation by cross winds. *J. Fluid Mech.* **96,** 757-767.

Flamant, C. , P. Drobinski, N. Furger, B. Chimani, S. Tschannett, R. Steinacker, A. Protat, H. Richner, S. Gubser, and C. Haberli, 2006: Föhn/CAP interactions in the Rhine valley during MAP IOP 15. *Quart. J. Roy. Meteorol. Soc.,* **132**, 3035-3058.

Grainger, C., and R. N. Maroney (1993): Dispersion in an open-cut coal mine in stably stratified flow. *Bound. Layer. Meteorol.* **63**, 117-140.

Gubser, S., and H. Richner, 2001: Investigations into mechanisms leading to the removal of the cold-pool in foehn situations. Extended abstract, *MAP meeting at Schliersee. MAP Newsletter 15*. Available at: http://www.map.meteoswiss.ch/map–doc/NL15/gubser2.pdf

Lareau, N. P., E. Crosman, C. D. Whiteman, J. D. Horel, S. W. Hoch, W. O. J. Brown, and T. W. Horst, 2013: The persistent cold-air pool study. *Bull. Amer. Meteor. Soc.*, **94,** 51–63.

Lee, T. J., and R. A. Pielke, 1989: Influence of cold pools downstream of mountain barriers on downslope winds and flushing. *Mon. Wea. Rev.*, **117,** 2041-2058.

Lee, J. T., R. E. Lawson Jr., and G. L. Marsh, 1987: Flow visualization experiments on stably stratified flow over ridges and valleys. *Meteor. Atmos. Phys.,* **37,** 183-194.

Malek, E., T. Davis, R. S. Martin, and P. J. Silva, 2006: Meteorological and environmental aspects of one of the worst national air pollution episodes in Logan,

Cache Valley, Utah, USA. *Atmos. Res.,* **79,** 108-122.

Nappo, C. J., 2002: *An Introduction to Atmospheric Gravity Waves.* Academic Press. 279 pp.

Pataki, D. E., B. J. Tyler, R. E. Peterson, A. P. Nair, W. J. Steenburgh, and E. R. Pardyjak, 2005: Can carbon dioxide be used as a tracer of urban atmospheric transport? *J. Geophys. Res.,* **110,** D15102.

Pataki, D. E., D. R. Bowling, J. R. Ehleringer, J. M. Zobitz, 2006: High resolution atmospheric monitoring of urban carbon dioxide sources. *Geophys. Res. Let.,* **33,** L03813.

Petkovšek, Z., 1992: Turbulent dissipation of cold air lake in a basin. *Meteor. Atmos. Phys.,* **447,** 237-245.

Petkovšek, Z., and T. Vrhovec (1994): Note on the influences of inclined fog lakes on the air pollution in them and on the irradiance above them. *Meteor. Z.,* **3,** 227-23.

Pollard, R. T., P. B. Rhines, R. O. R. Y. Thompson 1973: The Deepening of the Wind-Mixed Layer. *Geophys. Fluid Dyn.,* **3**, 381-404.

Pope, III C. A., and coauthors, 2006: Ischemic heart disease events triggered by short-term exposure to fine particulate air pollution. *Circulations,* **112,** 2443-2448.

Pope, III C. A., M. Ezzati, and D. W. Dockery, 2009: Fine-particulate air pollution and life expectancy in the United States. *New Engl. J. Med.,* **360,** 376-386.

Price, James F., C. N. K. Mooers, and J. C. Van Leer, 1978: Observation and simulation of storm-induced mixed-layer deepening. *J. Phys. Oceanogr.,* **8**, 582–599.

Rakovec, J., J. Merše, S. Jernej, and B. Paradiž, 2002: Turbulent dissipation of the cold-air pool in a basin: Comparison of observed and simulated development. *Meteor. Atmos. Phys.,* **79,** 195-213.

Reddy, P. J., D. E. Barbarick, and R. D. Osterburg, 1995: Development of a statistical model for forecasting episodes of visibility degradation in the Denver metropolitan area. *J. Appl. Meteor.,* **34,** 616-625.

Reeves, H. D., and D. J. Stensrud, 2009: Synoptic-scale flow and valley cold pool evolution in the western United States. *Wea. Forecasting,* **24,**1625-1643.

Silcox, G. D., K. E. Kelly, E. T. Crosman, C. D. Whiteman, and B. Allen, 2012: Wintertime PM2.5 concentrations in Utah's Salt Lake Valley during persistent, multiday cold-air pools. *Atmos. Environ.,* **46,** 17-24.

Skamarock, W. C., J. B. Klemp, J. Dudhia, D. O. Gill, D. M. Barker, M. G. Duda, X. Huang, W. Want, and J. G. Power, 2008: A description of the advanced research WRF version 3. NCAR Tech. Note, NCAR/TN-475+STR, 113 pp.

Skamarock, W. C., cited 2014: Density current test case. *A Standard Test Set for Nonhydrostatic Dynamical Cores of NWP Models.* Available at: http://www.mmm.ucar.edu/projects/srnwp_tests/density/density.html

Straka, J. M., R. B. Whilhelmson, L. J. Wicker, J. R. Andernson, and K.K. Droegemeier, 1993: Numerical solutions of a nonlinear density-current - A benchmark solution and comparisons. *Int. J. for Numerical Methods in Fluids*, 1-22.

Strang, E. J., and H. J. S. Fernando, 2001a) Entrainment and mixing in stratified shear flows. *J. Fluid. Mech.,* **428,** 349-386.

Strang, E. J., and H. J. S. Fernando, 2001b: Vertical mixing and transports through a stratified shear layer. *J. Phys. Oceanogr.,* **31,** 2026-2048.

Tampieri, F., and J. C. R. Hunt, 1985: Two-dimensional stratified fluid flow over valleys: Linear theory and laboratory investigation. *Bound.-Layer Meteor.,* **32,** 257-279.

Vrhovec, T., and A. Hrabar, 1996: Numerical simulations of dissipation of dry temperature inversions in basins. *Geofiz.,* **13,** 81-96.

Wei, L., Z. Pu, and S. Wang, 2013: Numerical simulation of the life cycle of a persistent wintertime inversion over Salt Lake City. *Bound.-Layer Meteor.,* **148,** 399-418.

Whiteman, C. D., X. Bian, and S Zhong, 1999: Wintertime evolution of the temperature inversion in the Colorado Plateau Basin. *J. Appl. Meteor.,* **38,** 1103-1117.

Whiteman, C. D., S. Zhong, W. J. Shaw, J. M. Hubbe, X. Bian, and J. Mittelstadt, 2001: Cold pools in the Columbia basin. *Wea. Forecasting,* **16,** 432-447.

Wolyn, P. G., and T. B. McKee, 1989: Deep stable layers in the intermountain Western United States. *Mon. Wea. Rev.* **117,** 461-472.

Zängl, G., 2003: The impact of upstream blocking, drainage flow and the geostrophic pressure gradient on the persistence of cold-air pools. *Quart. J. Roy. Meteor. Soc.,* **129,** 117–137.

Zängl, G., 2005: Winterime cold-air pools in the Bavarian Danube Valley Basin: Data analysis and idealized numerical simulations. *J. Appl. Meteor.,* **44,** 1950-1971.

Zardi, D. and C. D. Whiteman, 2013: Diurnal Mountain Wind Systems. *Mountain Weather Research and Forecasting: Recent Progress and Current Challenges,* F. K. Chow, S. F. J. De Wekker, and B. Snyder, Ed., Springer, 35-119.

Zhong, S., C. D. Whiteman, X. Bian, W. J. Shaw, and J. M. Hubbe, 2001: Meteorological processes affecting evolution of a wintertime cold air pool in a large basin. *Mon. Wea. Rev.,* **129,** 2600-2613.

Zhong, S., X. Bian, C. D. Whiteman, 2003: Time scale for cold-air pool breakup by turbulent erosion. *Meteor. Z.,* **12,** 229-23.

Table 3.1: Properties of each CAP profile used in this study. BH is the column-integrated buoyancy, defined in the text, and N max is the maximum Brunt-Vaisala Frequency.

CAP Profile	Surface Temperature Deficit (K)	BH $(m^2\ s^{-2})$	N Max (s^{-1})
Linear	10	82.8	0.027
Multi-Layer	10	82.8	0.043
Capping Layer	10	138.4	0.043
Shallow Layer	10	36.7	0.043
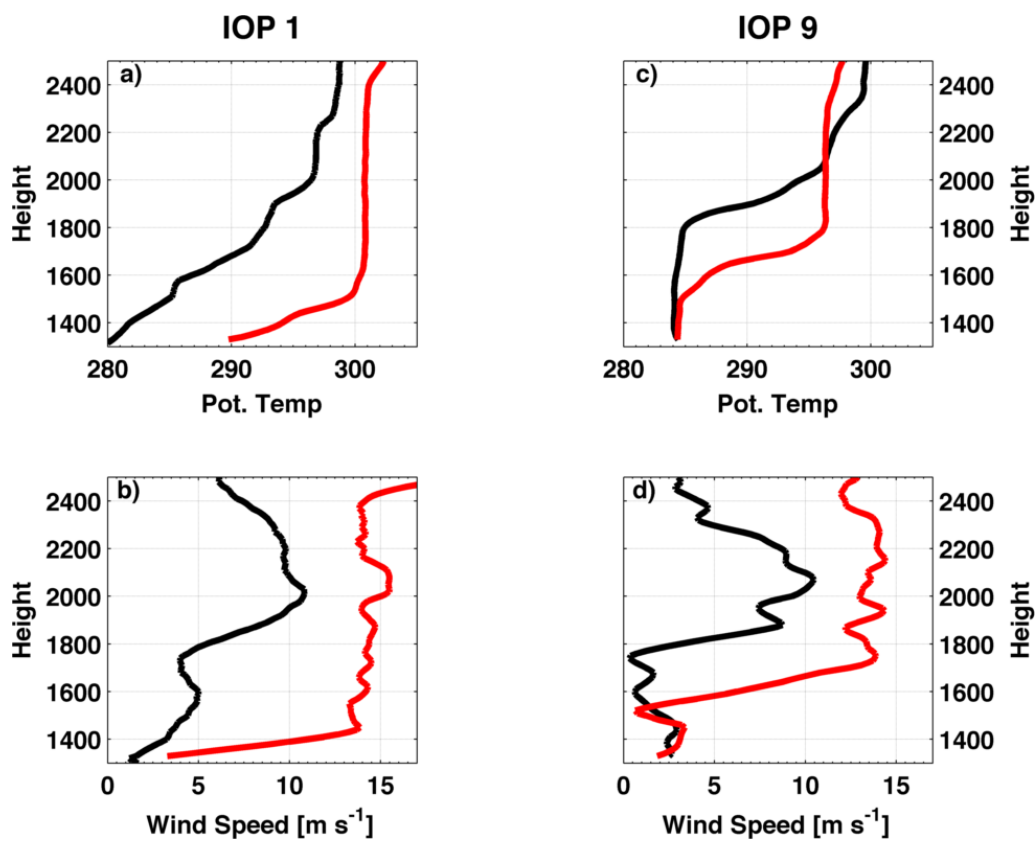
Fig. 3.1 Profiles of potential temperature (a,c) and wind speed (b,d) from PCAPS IOP-1 (left column, a,b) and IOP-9 (right column, c,d). For each case the black line is ~18 hs prior to the red line.
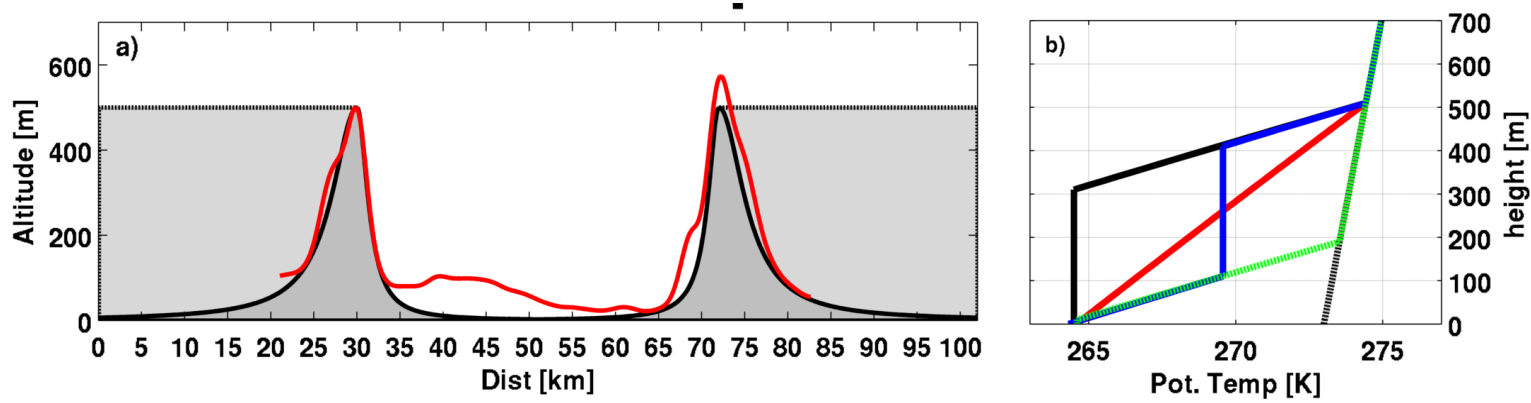
Fig. 3.2. Summary of numerical experiment design. (a) Model topography: mountain (e.g., control) topography (solid black line, dark gray shading) and plain topography (black line and light gray shading). The red line is a smoothed south-to-north transect of the Salt Lake Valley, UT. (b) CAP Potential temperature profiles: Linear (e.g. control, red), multilayer (blue), capping layer (black), shallow (dashed green), and inflow profile (gray).
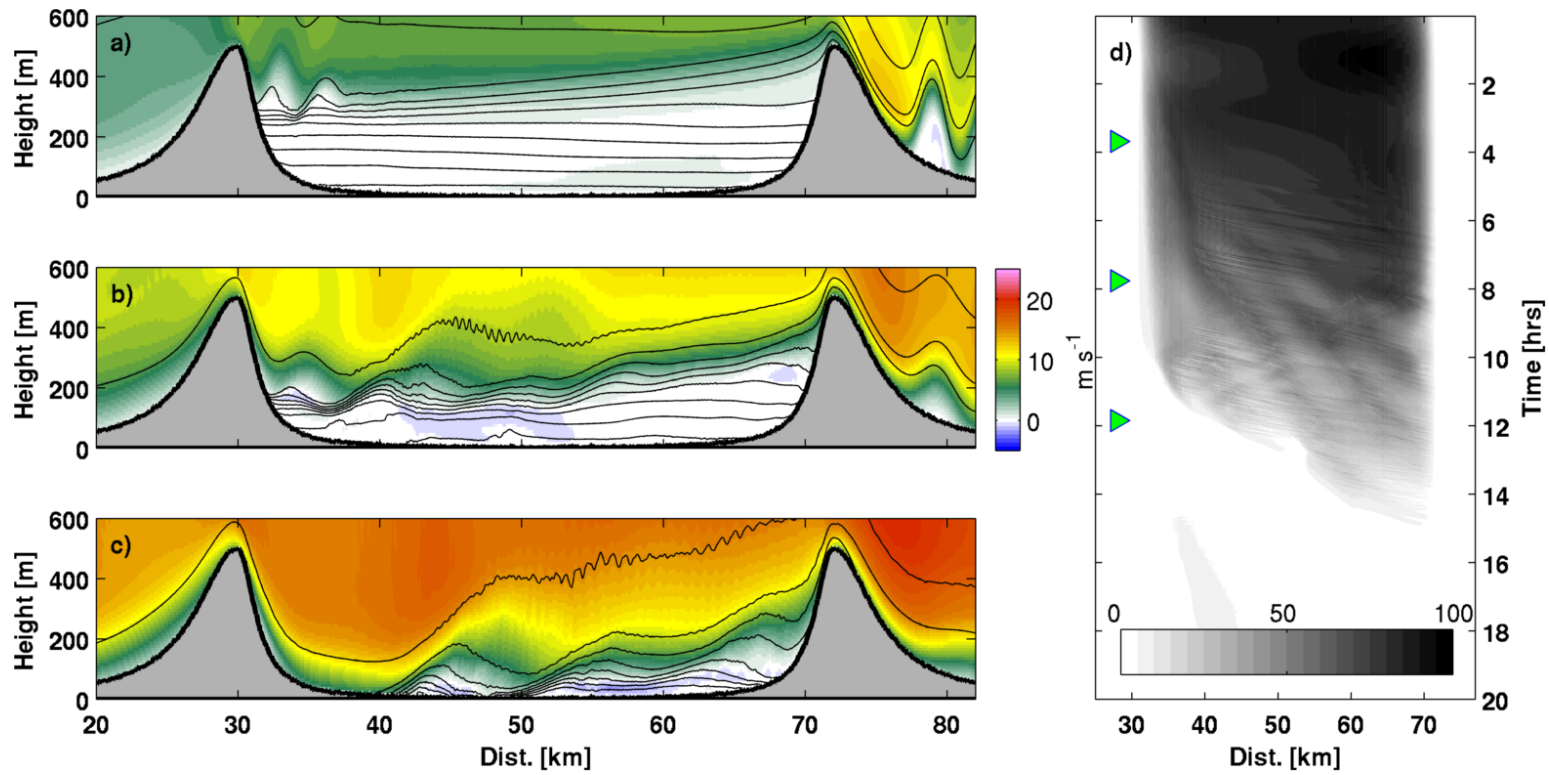
Fig. 3.3. Twenty min time-mean cross sections of potential temperature (contours, c.i. 1 K) and wind speed (shading) for the linear CAP mountain case at (a) 5, (b) 10, and (c) 15 m s^{-1} inflow. (d) Time-distance distribution of column integrated buoyancy (BH).
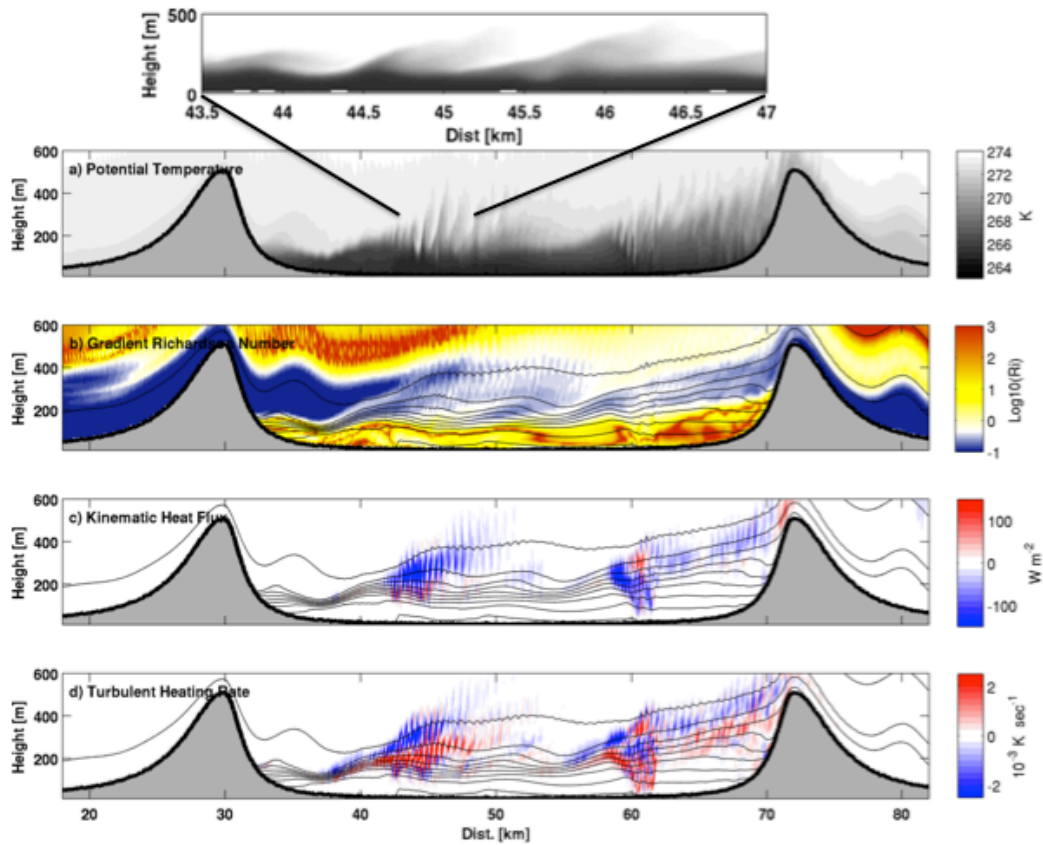
Fig. 3.4. Snapshot of waves impacting the CAP at 500 mins (11 m s^{-1}) (a) potential temperature, (b) log base 10 of the gradient Richardson number (blue shading for subcritical values), (c) kinematic heat flux, and (d) turbulent heating rate. Contours in b-d are potential temperature every 1 K. The upper most panel is a detail of the Kelvin-Helmholtz waves in equal aspect ratio.
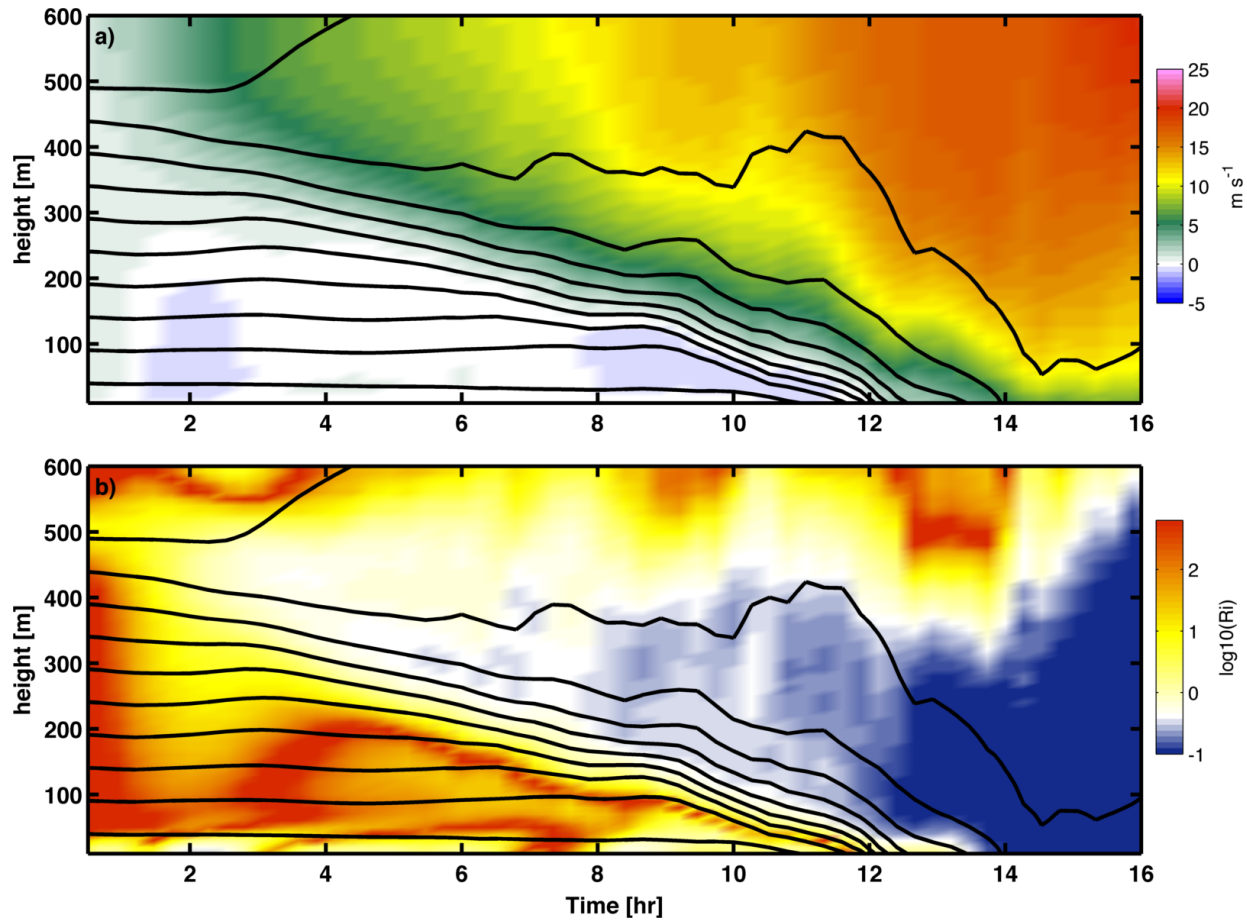
Fig. 3.5. Time-height evolution of (a) wind speed and (b) log base 10 of the gradient Richardson number for the valley mean column. Contours in both panels are potential temperature at 1 K intervals.
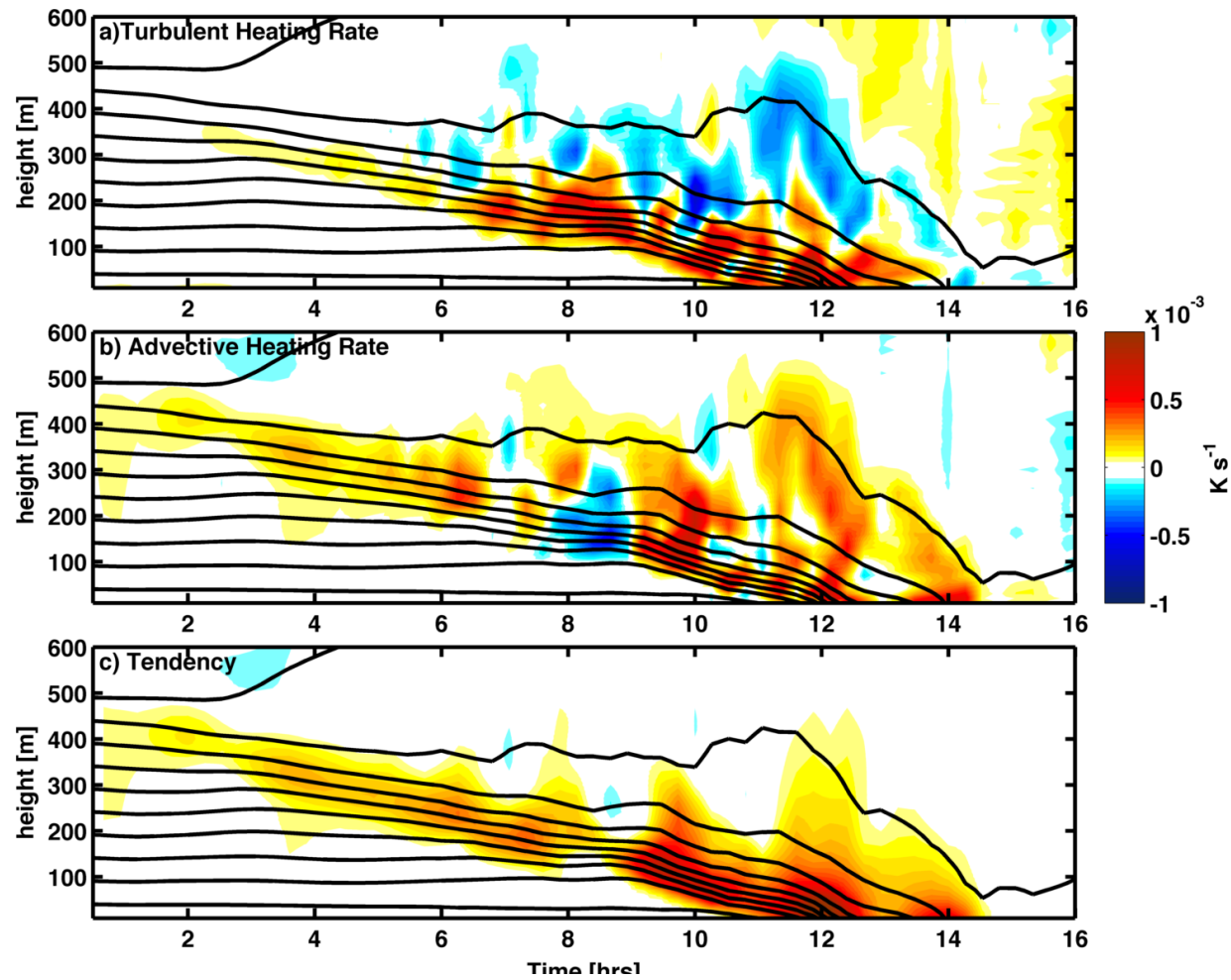
Fig. 3.6. Time height evolution of the heat budget for the valley mean column. (a) Turbulent heating rate, (b) advective heating rate, and (c) net heating tendency. Contours in all panels are potential temperature every 1K.
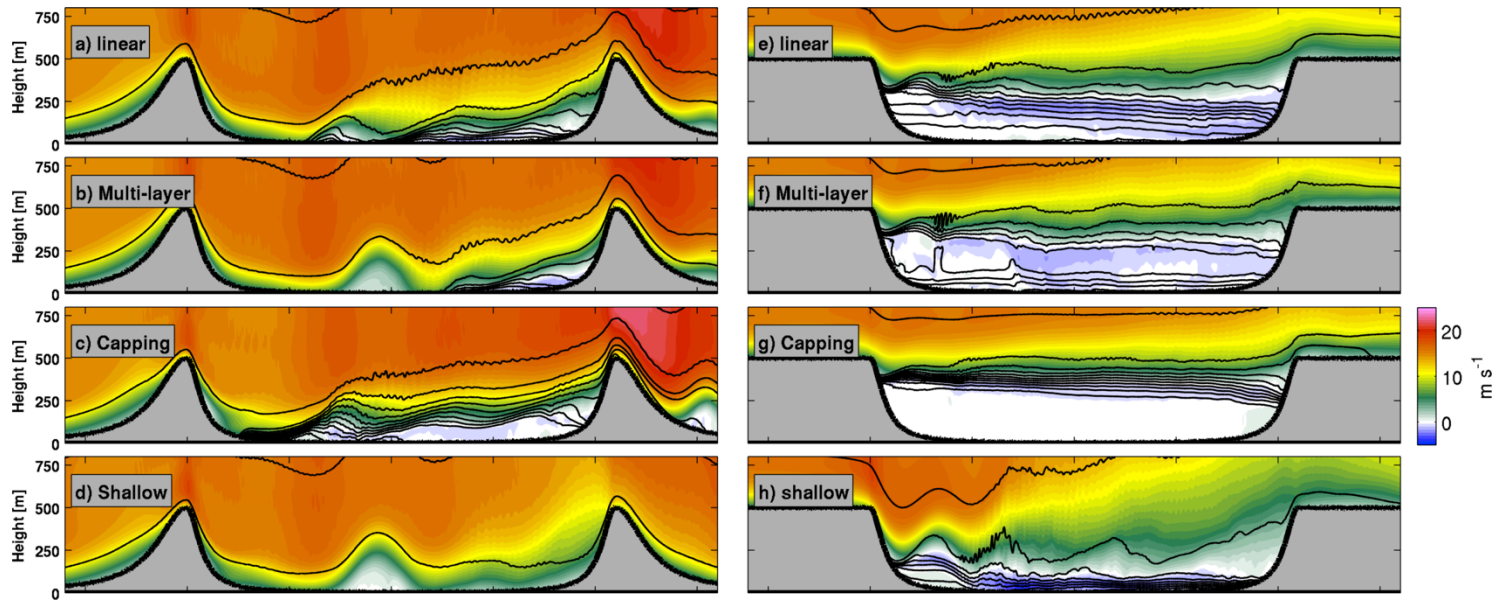
Fig. 3.7 Snap shots of each experimental run at 15 m s^{-1} inflow. The left column is the mountain simulations (a-d) and the right column is the plain simulations (e-h). The profiles are labeled in the figure.
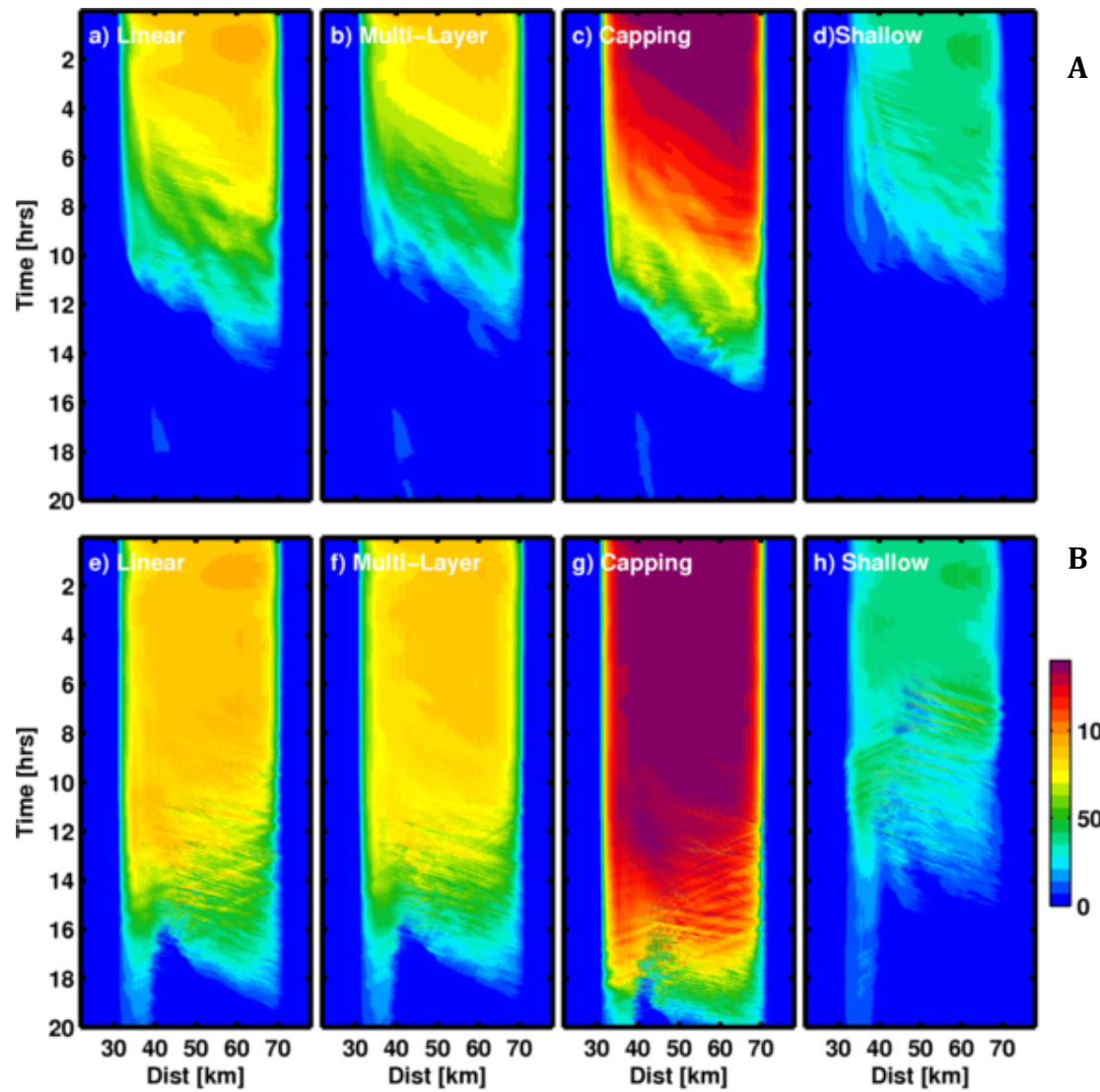
Fig. 3.8. Time-distance evolution of the column integrated buoyancy for each case. Top (A) and bottom (B) rows are the mountain and simulations, respectively. Profiles are labeled in the figure.
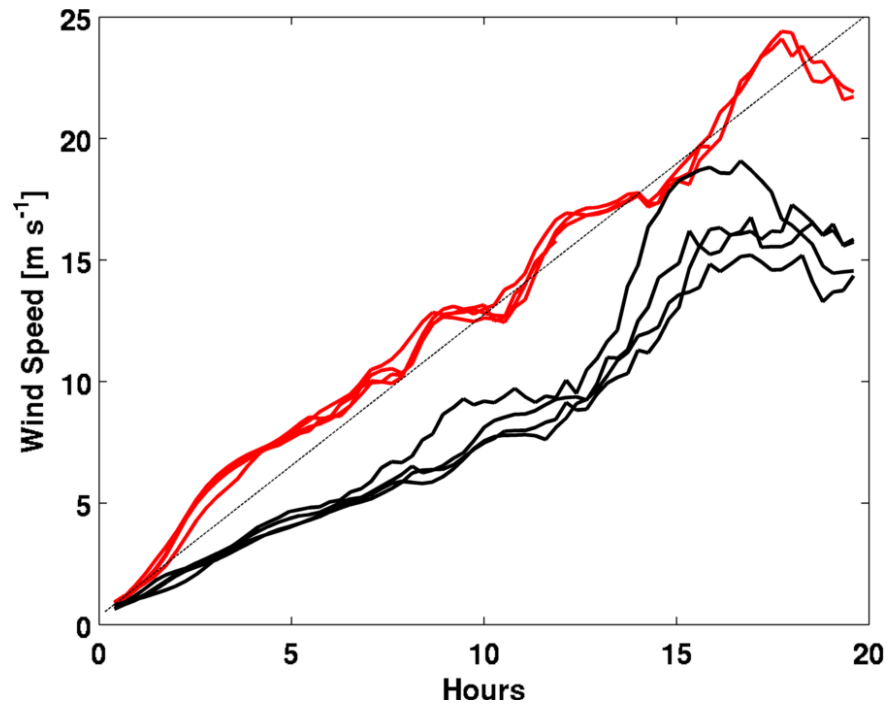
Fig. 3.9. Mean wind at 500-m above the valley floor for the mountain cases (red) and plain cases (black). The dashed line is prescribed inflow velocity.
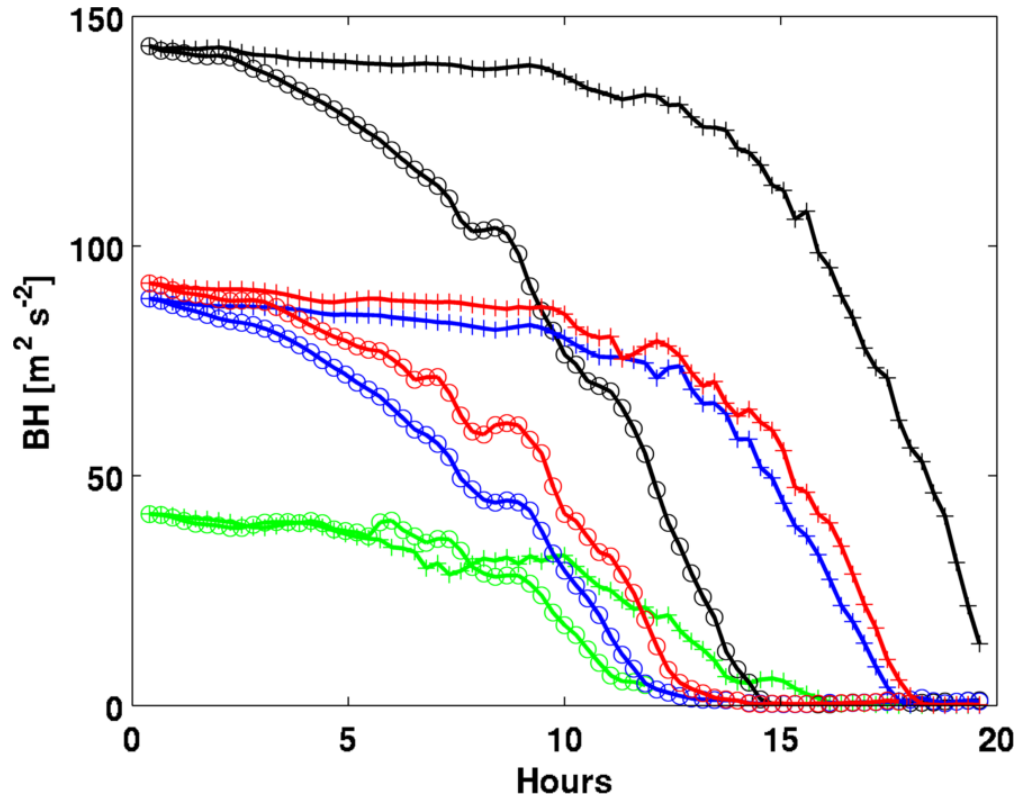
Fig. 3.10. Column integrated buoyancy, BH, as a function of time for each case. Circles represent the mountain cases and plus symbols represent the plain cases. Colors correspond to the different profiles: linear (red), multi-layer (blue), capping layer (black), and shallow layer (green).
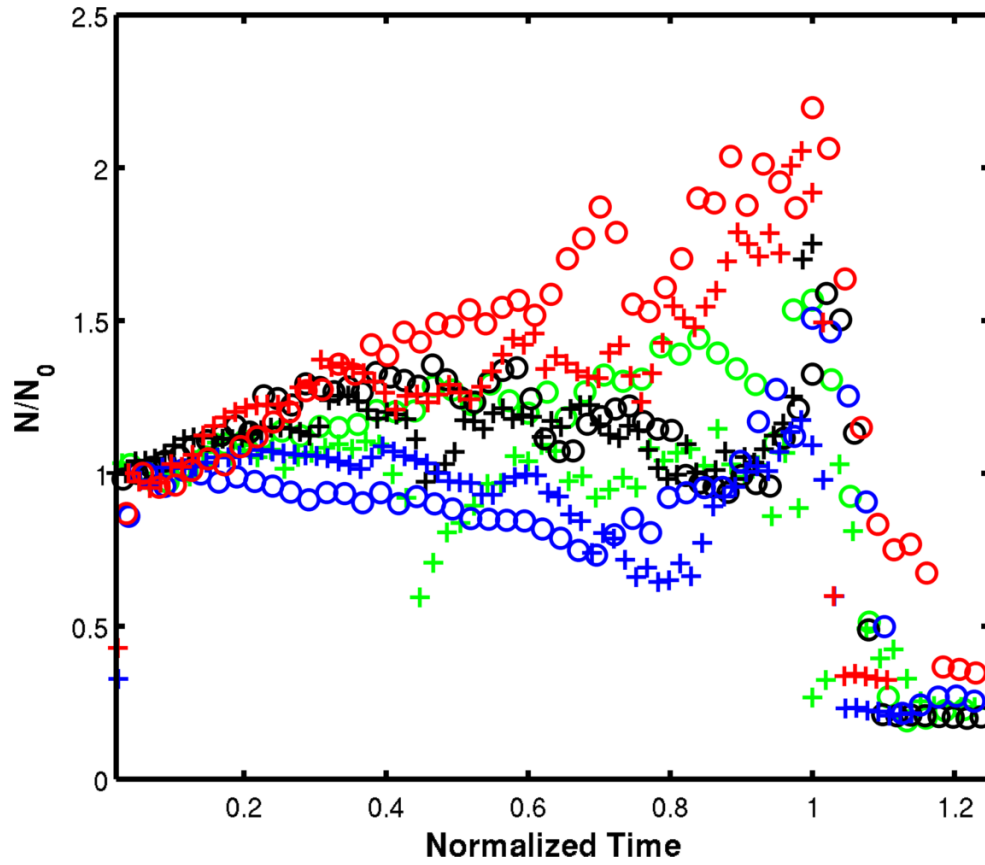
Fig. 3.11. Time evolution of the capping layer Brunt-Vaisala frequency normalized by its initial value. Time has also been normalized such that the time of CAP removal corresponds to 1. The circles correspond with the plain cases, and the pluses the mountain cases. Profiles are indicated by color: linear (red), multilayer (blue), capping layer (black), and shallow layer (yellow).
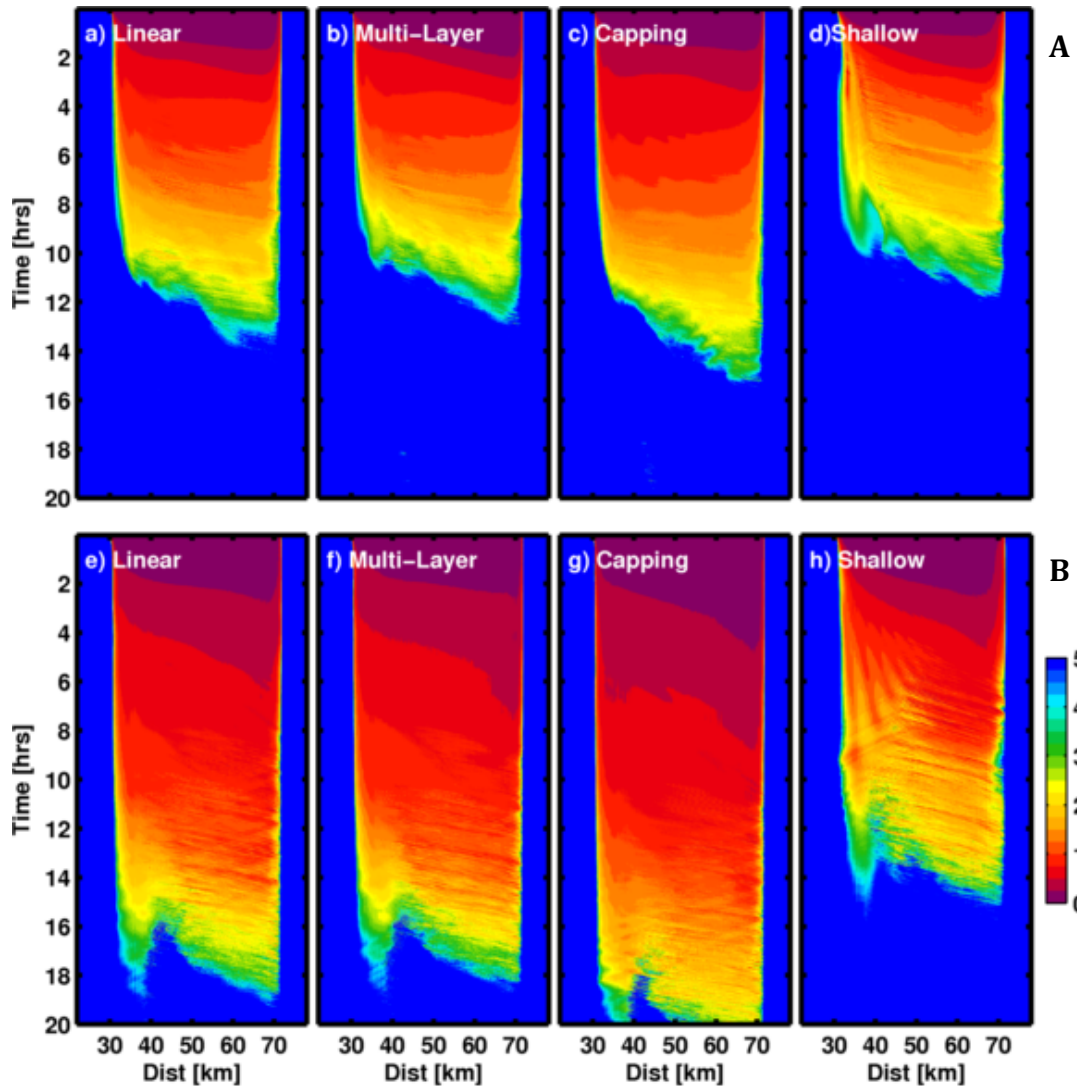
Fig. 3.12.Time-distance evolution of the column Froude number. Top (A) and bottom (B) rows are the mountain and simulations, respectively. Profiles are labeled in the figure.
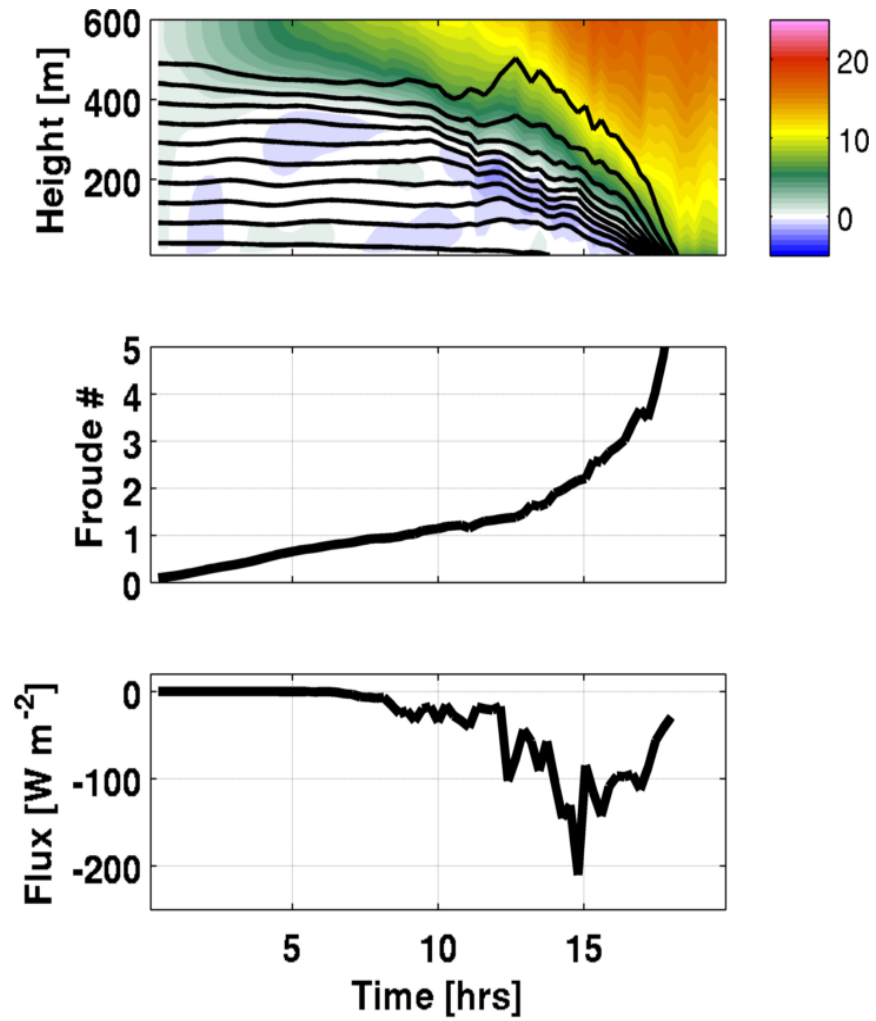
Fig. 3.13. Summary of the linear-plane case: (a) Wind (shaded) and potential temperature (contoured), (b) Froude number time series, (c) column minimum heat flux (negative downwards).
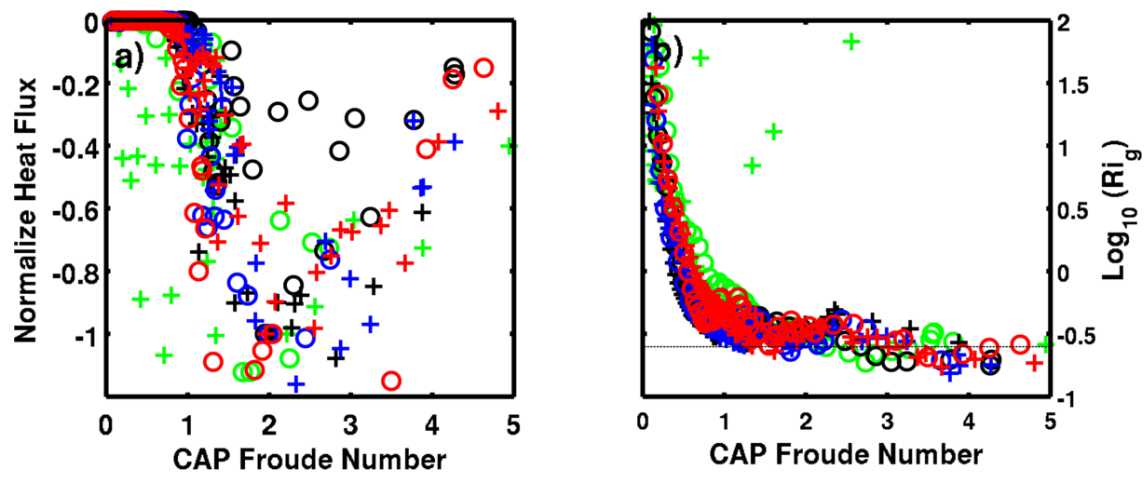
Fig. 3.14. Summary of the CAP parameter space: (a) Column minimum heat flux versus Froude number for each case. (b) Log base 10 of the gradient Richardson number at the CAP top versus Froude number (log10(Ri$_c$) =-.6).
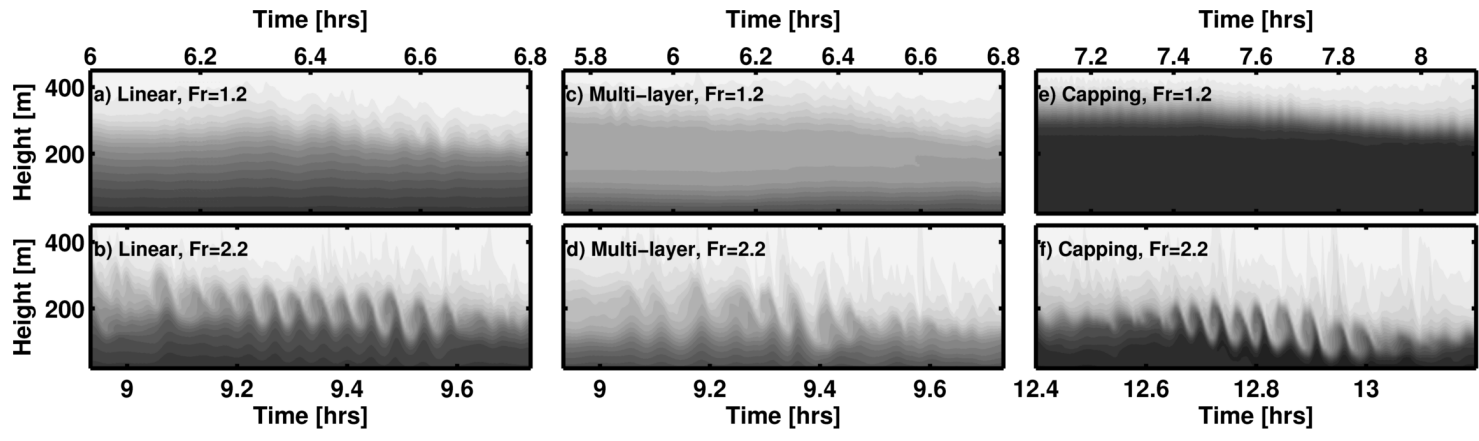
Fig. 3.15. Kelvin-Helmholtz waves at Fr~=1.2 (top row) and Fr~=2.2 (bottom row) for (a,b) mountain-linear, (c,d) mountain multilayer, and (e,f) mountain capping layer.
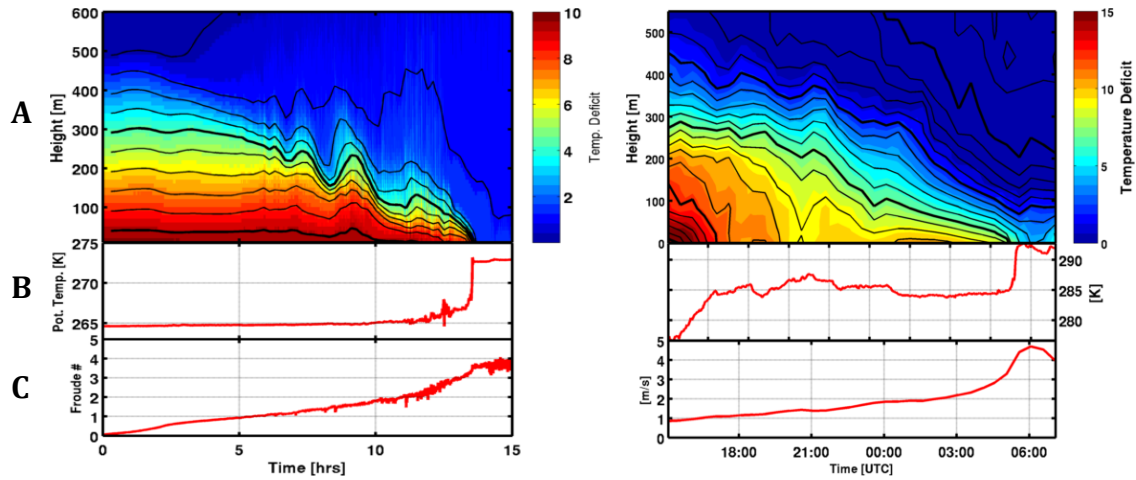
Fig. 3.16. Comparison between the linear-mountain simulation (left column) and PCAPS IOP-1 on 2-3 December 2010 (right column). Top row (A) shows the potential temperature time-height and temperature deficit (shading). The middle row (B) is the surface temperature in Kelvin. The bottom row (C) is the CAP Froude number.
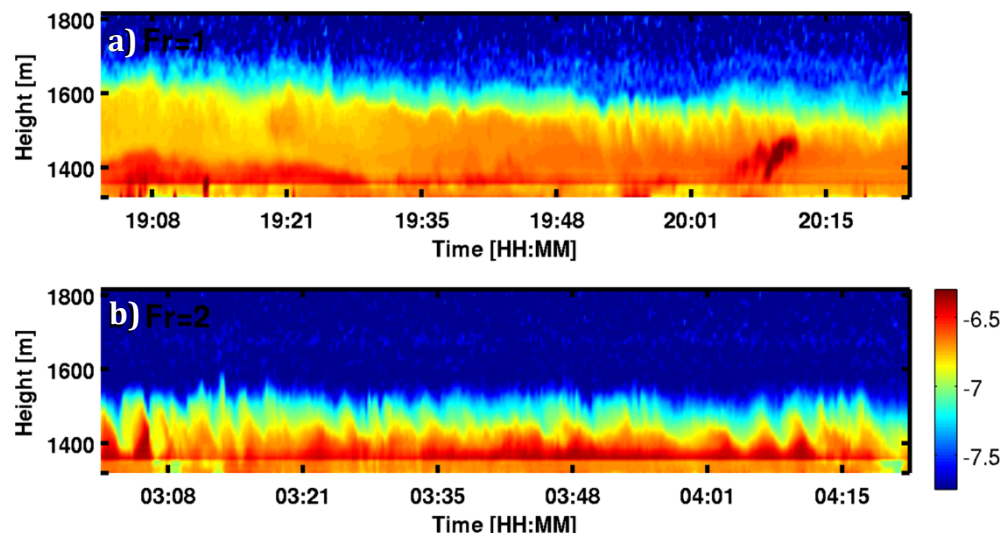
Fig. 3.17. Example of waves on 3 December during PCAPS IOP-1 for Fr=1 (a) and Fr=2 (b). Data are aerosol backscatter from a laser ceilometer.

CHAPTER 4

CONCLUSIONS

The research trajectory encompassing the work presented by Lareau et al. (2013) and that was presented in the previous chapters is summarized here. This research effort spans the initial formulation of a research problem, namely CAP breakup by wind, through iterative steps including the design of a field program, data analysis, and numerical modeling. The lessons learned and how the elements of the research are interconnected is reflected upon. The discussion is concluded in terms of future investigations that would complement the contributions to wind-induced CAP breakup presented throughout this work.

An investigation of wind-induced CAP destruction was first proposed as a sub-experiment of the Persistent Cold-Air Pool Study (PCAPS), which was a broader investigation of the lifecycle of multiday CAPs in Utah's Salt Lake Valley (Lareau et al. 2013). Prior to PCAPS, cold-air pool breakup by wind was addressed in only a handful of observational studies (Whiteman et al. 2001, Flamant et al. 2002, Rakovec et al. 2002), yet represented a major rationale for CAP removal within the SLV. Subjective evaluation of prior events indicated that strong south winds preceding shortwave troughs often produced either partial or complete removal of CAPs, but the mechanisms for the removal were incompletely understood and difficult to forecast.

To address this problem, a targeted observation plan was developed wherein coordinated radiosondes were to be launched along a south-to-north transect of the SLV when strong winds were forecast during major CAPs events. The goal was to observe the spatial variations in the CAP depth and structure (e.g., tilting), and if possible, the complete eradication of the stratification by wind. These upper air data were to be complemented with a distributed network of surface observations and continuously monitoring remote sensing instruments that formed the core of the PCAPS project. This targeted operation plan was implemented during three CAPs during PCAPS (See Fig. 1.3), each time capturing a portion of the spatial and temporal variations induced within CAPs by the strong winds aloft. Amongst these CAPs, the IOP-1 data set provided the richest and most complete set of observations, becoming the foundation for the observational component of this dissertation.

The PCAPS operations also presented a platform for individual growth in terms of scientific leadership and decision-making. For example, it was the author's responsibility to lead daily forecast and operations meetings and to help organize resource deployments to accomplish the scientific goals of the field campaign. Thus, the project itself spanned scientific problem formulation, experiment design, and logistical implementation. These elements and the preliminary findings of field program were collaboratively summarized in an overview publication (Lareau et al. 2013).

Following completion of the field phase of PCAPS, attention turned to post-processing observations across a range of meteorological platforms. Portions of these data were subsequently combined to produce a time-height representation of the valley atmosphere throughout the PCAPS project. Specifically, the data set is comprised of a

linear averaging of radiosonde data (spaced from 3-12 hs apart) with continuously recording remote sensor measurements (filling gaps using novel procedures) and constrained by surface observations. The resulting profiles prove useful across a range of PCAPS investigations, including analyses of mixing depth within CAPs, linking pollution and CAP strength, model verification, and not least, the analyses presented in this dissertation.

One of the key "lessons learned" from both the field program and the subsequent data processing is the utility of collocated instrumentation for boundary layer meteorology. For example, the combination of proximally located radiosondes, wind profilers, and acoustic soundings provides a more nuanced view of CAP evolution than is possible from discrete radiosondes alone. Even more so, the presence of a laser ceilometer was remarkably, and unexpectedly, useful for determining aerosol depth and structure within CAPs, as highlighted by Young (2013). These ceilometer data corroborate interesting features within the thermodynamic profile. For example, the sharp variations in potential temperature during IOP-5 (Fig. 1.2) might be dismissed as erroneous noise were it not for the corresponding aerosol convective plumes.

The PCAPS data resources, including the ceilometer, form the backbone for the analyses presented in Chapter 2, which are a scientific dissection of the physical processes arising due to wind-CAP interaction. These elements of the CAP evolution include: mountain-wave CAP interaction, CAP tilt, surface fronts, dynamic instability, turbulent mixing, gravity currents, and basin-scale oscillations. Identification of these processes addressed a fundamental goal of PCAPS, which was to document the multi-scale meteorological processes affecting CAP evolution.

Many of the meteorological aspects of the CAP disruption during IOP-1 would be unknown without the PCAPS observations. For example, the modeling investigation by Wei et al. (2013) fails to identify most of these significant features, thereby posing an overly simple perspective of the evolution of the IOP-1 CAP. That study does not incorporate PCAPS data beyond operational radiosondes at 12-h intervals. Future studies might take fuller advantage of data assimilation of the PCAPS observations to better resolve complex aspects of CAP dynamics.

While the PCAPS observations were fundamental to develop a nuanced conceptual model for IOP-1 CAP displacement, they also have limitations. For example, the laser ceilometer revealed the presence of Kelvin-Helmholtz waves within the CAP, but there were no systematic observations of the turbulent fluxes or kinematic structure within these breaking waves. Surface flux towers were in use, but at 10-m were not sufficiently tall to capture these wave-generated turbulent processes affecting the CAP at elevations greater than 100 m above the surface. As such, a complete picture of the top-down removal of the CAP was not possible from observations alone.

To address this shortcoming in our analyses, a modeling study was conducted to provide a detailed perspective on the role of turbulent CAP erosion. Idealized Large-Eddy Simulations (LES) were chosen as an appropriate research tool capable of resolving this component of CAP removal. The model was configured to examine the interaction of accelerating flow aloft with idealized CAPs comparable to those during PCAPS. The model resolution permitted explicit simulation of dynamic instability in stratified shear flow that was not possible in previous modeling studies investigating this subject. The model results revealed that the wind-induced CAP destruction occurs via the interplay of

Kelvin-Helmholtz waves and warm air advection and that the complete CAP removal can be accomplished on diurnal time scales. A range of sensitivity studies further indicated that a simple dimensionless number, the CAP Froude number, could be used to diagnose the onset and amplification of turbulent CAP erosion.

These model-based conclusions were subsequently used to reexamine a portion of the results from PCAPS IOP-1, finding a compelling similarity between model and observations both in terms of the details of turbulent mixing and the applicability of the CAP Froude number. This interchange of findings between observations and simulations reflects a key aspect of modern meteorological research, namely that observations sometimes reveal the need for numerical investigation, and sometimes vice versa.

To that end, further field investigations of CAP turbulent erosion are required to verify the broader applicability of the modeling results obtained from this study for CAPs and other stably stratified air masses. To accomplish this goal, instrumentation beyond those available in PCAPS are required. Specifically, there is a need to resolve the CAP dynamics on scales comparable to that of the LES, e.g., 50-100 m. This requirement is not solely to validate the model but is more fundamentally tied to the scale of the turbulence that acts to destroy CAPs. Both the observations and simulations indicate KHW with scales of 100-200 m vertically and ~ 1 km horizontally.

Scanning Doppler lidar is one promising tool for this task, providing high spatial (~20 m) and temporal (~1 sec) resolution aerosol backscatter intensity and radial velocity over a range of a few km. For example, vertically pointed lidar during a CAP "mix-out" could potentially quantify the turbulent entrainment velocity at the interface between stratified air and warm air aloft. Previous investigators use lidar in a similar approach to

obtain entrainment rates for the convective boundary layer (Boers et al. 1983). Range-height scans might also more fully resolve the kinematic structures of KHW, as shown by Newsom and Banta (2003), as compared with qualitative assessments provided by the laser ceilometer. It is also possible to use multiple Doppler lidars to construct "virtual tall towers," as recently shown by Wang et al. (2013) during the MATTERHORN field experiment, which investigated thermally driven flows in complex topography (Fernando et al. 2013). Doing so would allow quantification of the turbulent three-dimensional flow over the full depth of a CAP, providing data that would be more directly comparable with laboratory tank experiments (e.g., Strang and Fernando 2001 a,b) and the numerical simulations in Chapter 3.

Even with Doppler lidar, a remaining challenge is the need for high temporal and spatial resolution measurements of temperature with height during turbulent erosion events. These data are necessary to quantify the "interfacial buoyancy flux" representing the removal of cold air from within the CAP and might be obtained from tethered sondes, frequent radiosondes, or, ideally, a tall tower (e.g., CASES-99, Poulos et al. 2002).

One final consideration is the need for a large sample of events to formulate robust statistics regarding erosion rates during strong winds. Since "mix outs" are relatively infrequent in the SLV, e.g., a few per winter, additional settings for the interaction of strong flow and semipermanent stable boundary layers are sought. One possible natural laboratory is the interaction of the marine layer, which tends to be capped with strong static stability, with offshore flows along the California coast. For example, Santa Anna winds are known to displace and erode the marine layer from the region surrounding Los Angles, CA, an example of which is shown in Fig 4.1. That data, obtained using a mobile

Doppler lidar situated near Oxnard, CA on 3 October 2013 (courtesy of Dr. C. Clements), shows the continual top-down removal of the marine layer by strong easterly flow aloft. The warmer turbulent layer eventually erodes to the surface, producing sudden warming analogous to the results found in Chapters 2 and 3.

The Santa Anna wind event emphasizes that the mechanical removal of stratified and topographically confined air masses is relevant beyond the basins of the Intermountain West. For example, the mechanical removal of the marine layer and the onset of warm dry winds at the surface are critically important for fire weather forecasts. Turbulent erosion of this sort may also be an important factor in the removal of cold-air dams along the Appalachian and Rocky Mountains, and thus affect forecasts for high impact freezing rain events (Lackman 2011). Less directly, the surfacing of strong winds has also gained attention within the wind-energy community in terms of sudden "ramp" events that affect power generation and put strain on wind turbines.

Ultimately this dissertation is a short compendium of the author's original contributions to our understanding of the breakup and disruption of CAPs by wind. The research addresses a local and regional problem for the Salt Lake Valley and Intermountain West, but is of broader scope and applicability. The results provide a clearer understanding of the myriad and complex processes contributing to the break-up of CAPs by strong winds and establish groundwork for future investigations.

4.1 References

Boers, R., E. W. Eloranta, and R. L. Coulter, 1984: Lidar observations of mixed layer dynamics: Tests of parameterized entrainment models of mixed layer growth rates. *J. Appl. Meteor.,* **23,** 247-266.

Flamant, C. , P. Drobinski, N. Furger, B. Chimani, S. Tschannett, R. Steinacker, A. Protat, H. Richner, S. Gubser, C. Haberli, 2006: Föhn/CAP interactions in the Rhine Valley during MAP IOP 15. *Quart. J. Roy. Meteor. Soc.,* **132**, 3035-3058.

Fernando, H. J., E. Pardyjak, J. Hacker, S. De Wekker, F. K. Chow, and Y. Wang, 2013: A14D-02. The Mountain Terrain Atmospheric Modeling and Observations (MATERHORN) Program: An Overview. Proceedings, *2012 Fall Meeting, San Francisco,* CA, Amer. Geophys. Union, A14D-02.

Lackmann, G. M., 2011: *Midlatitude Synoptic Meteorology: Dynamics, Analysis, and Forecasting*. Amer. Met. Soc., 345 pp.

Lareau, N. P., E. Crosman, C.D. Whiteman, J.D. Horel, S.W. Hoch, W.O.J. Brown, T.W. Horst, 2013: The persistent cold-air pool study. *Bull. Amer. Meteor. Soc.*, **94**, 51–63

Newsom, R. K., and R. M. Banta, 2003. Shear-flow instability in the stable nocturnal boundary layer as observed by Doppler Lidar during CASES-99. *J. Atmos. Sci.* **60,** 16–33.

Poulos, Gregory S., and Coauthors, 2002: CASES-99: A Comprehensive investigation of the stable nocturnal boundary layer. *Bull. Amer. Meteor. Soc.*, **83**, 555–581.

Rakovec, J., J. Merše, S. Jernej, and B. Paradiž, 2002: Turbulent dissipation of the cold-air pool in a basin: Comparison of observed and simulated development. *Meteorol. Atmos. Phys.,* **79,** 195-213.

Strang, E. J., and H. J. S. Fernando, 2001a: Entrainment and mixing in stratified shear flows. *J. Fluid Mech.,* **428,** 349-386.

Strang, E. J., and H. J. S. Fernando, 2001b: Vertical mixing and transports through a stratified shear layer. *J. Phys. Oceanogr.,* **31,** 2026-2048.

Wang, Y., E. Creegan, M. Felton, G. Huynh, C. Hocut, H. J. Fernando, S. Hoch, and C. D. Whiteman, 2013: Application of triple Doppler wind lidars for the study of an atmospheric boundary layer over a mountainous area. Proceedings, *2012 Fall Meeting, San Francisco,* CA, Amer. Geophys. Union, A14D-08

Whiteman, C. D, S. Zhong, W. J. Shaw, J. M. Hubbe, X. Bian, and J. Mittelstadt, 2001: Cold pools in the Columbia basin. *Wea. Forecasting,* **16,** 432-447.

Young, J., 2013: Investigation of wintertime cold-air pools and aerosol layers in the Salt Lake Valley using a laser ceilometer. MS Thesis. University of Utah. 118 pp.
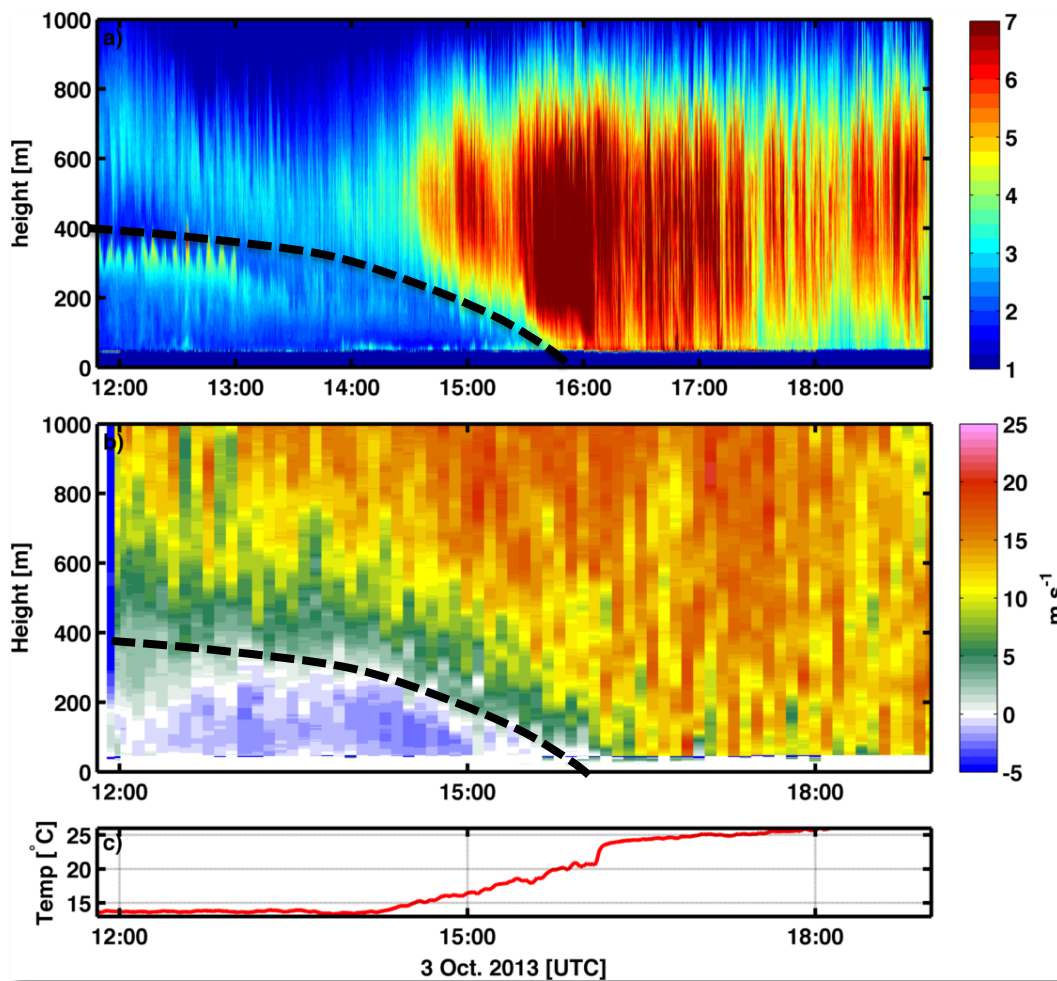
Fig. 4.1. Top-down removal of the marine layer near Oxnard, CA during Santa Anna winds on 3 October 2013. (a) Logarithmic aerosol backscatter, (b) stream wise wind along the ~50 degree azimuth, and (c) surface temperature. The black dashed line subjectively identifies the top of the marine layer.